MAX-PLANCK-GESELLSCHAFT

Electronic and Magnetic Properties of Graphene-Based Systems

Dissertation

zur Erlangung des Akademischen Grades
Doctor rerum naturalium
(Dr. rer. nat.)

vorgelegt von

Dipl.-Phys. Martin Weser
Fritz-Haber-Institut der Max-Planck Gesellschaft

eingereicht am 21.02.2013
im Fachbereich Physik der Freien Universität Berlin
Disputation am 22.04.2013

Gutachter: Prof. Dr. K. Horn
Prof. Dr. U. Bovensiepen

Contents

Chapter 1

Introduction

Graphene is one of the best examples for the stepwise or cyclic renaissance and disappearance of general scientific topics. Every time when a topic comes back into the main focus of researchers further knowledge is generated and after a plurality of such cycles this progress ends in the understanding of the research field or even in applications. In the case of carbon allotrope research the last cycle has demonstrated a new quantity of research leading to the more than 15 000 publications within seven years.

One of the earliest steps in this field was performed by Wallace in 1947 [1]. Under the intention to estimate the band structure of graphite, he reduced the graphite crystal to a single layer of hexagonally arranged C atoms and thus to a free-standing graphene layer. Furthermore, to reduce the complexity he separated the graphene lattice into two nearly independent sublattices.

In the 70 s and 80 s, scientists studied intensively intercalation compounds of graphite [2]. After the investigation of many intercalation systems including the insertion of atoms and molecules into the graphite lattice the interest was reduced. The intercalation of molecules separates the graphite layers such that it becomes similar to a graphene layer on a substrate with the same adsorbate on top. From the 80 s until 2000, graphene-like systems were studied only by a small number of scientists.

In 2004 the rush of excitement over graphene started to get momentum, in a similar vein as the ones on fullerenes in the late 80's and carbon nanotubes in the 90's. In a few groundbreaking papers, Geim and Novoselov demonstrated how one can isolate a one atomic thick C layer, named graphene. The preparation of graphene broke a thermodynamical law which was thought to prevail ever since Landau and Peierls concluded from a theoretical work that a purely two-dimensional material cannot exist [3, 4]. Strictly speaking, this prediction does not apply to the graphene flakes prepared by Geim and coworkers because these are either prepared on a substrate, or in the case of so-called "free-standing graphene" are suspended on all sides. At any rate, graphene exhibited a number of unexpected quantum phenomena such as the anomalous integer quantum Hall effect [5, 6], the isospin [1, 7] and a property which immediately attracted the interest of applications-oriented scientists, an extremely high electron mobility of about $10^7\,\mathrm{cm}/(\mathrm{V}\cdot\mathrm{s})$ [8], a consequence of the linear dispersion at the Fermi level. Moreover, the very large spin relaxation times [9] suggest possible spintronics applications of graphene.

At present, a large body of knowledge has been assembled concerning the properties of graphene, based on transport measurements, but also on the results of many surface-related experimental techniques such as photoemission, scanning tunneling microscopy/spectroscopy, and others. Graphene is a blessing for surface-related research since here we have a 2 D material at the atomic limit-graphene is "all surface and no bulk" [10]. Beyond an investigation of the properties of graphene itself, other important tasks are the investigation of the bonding mechanisms between graphene and substrates, in particular metallic ones on which high quality graphene films can be prepared.

This thesis deals with the interaction of graphene with transition metal surfaces and intercalated metals. It was motivated by early discoveries of large spin relaxation times in graphene [11] and predictions of spin filtering in the nickel/graphene/nickel system [12]. The first section of the thesis thus deals with electronic and magnetic coupling between graphene and ferromagnetic substrate; it is followed by the investigation of tuning possibilities for the electronic and magnetic interaction, by intercalating Fe and Al in between graphene and a Ni(111) substrate. The intercalation of Al underneath graphene on Ni(111) is shown to decouple graphene almost completely from the Ni surface. In contrast, intercalation of Fe shows almost no changes from graphene/Ni(111) host valence band structure, but it increases the magnetic moment induced into the graphene carbon atoms by a factor three. The thesis ends with an experiment to characterize two systems which could be important in future spintronic applications, i.e. graphene isolated on top of a ferromagnetic substrate, and to the growth of ordered graphene multilayers on top of Ni.

Chapter 2

Graphene

The goal of this chapter is to give a short introduction to carbon allotropes, their physical properties, electronic structure, and possible future applications. In recent years, several reviews have been published which summarize many aspects of current knowledge about graphene; for a more extensive survey, the interested reader is referred to these [13–17].

2.0.1 Allotropic Occurrence of Carbon

Carbon is probably the most important element for life on Earth due to the role which it plays in organic chemistry. This role arises from the flexibility of its bonding. Carbon-based systems show an unlimited number of different structures with an equally large variety of physical properties [13]. In nature atomic carbon is a very short-lived species and, thus carbon is stabilized in a pure carbon environment in various multi-atomic structures (carbon allotropic forms) depending on the hybridization of carbon atoms. sp^3 hybridized carbon atoms form diamond, sp^2 hybridization of carbon atoms leads to the formation of two-dimensional flat sheets consisting of hexagonal rings and loosely bonded to neighboring layers through weak van-der-Waals forces forming bulk graphite, and mixed sp^2/sp^3 hybridization leads to the arrangements of carbon atoms in fullerenes or carbon nanotubes (see also *Figure* 2.1) [18, 19]. These different types of hybridization lead to different geometrical structures, some examples of which are shown in Figure 1.1, and these result in very different physical and chemical properties. The group of these materials is summarized under the name "allotropes of carbon". Diamond is transparent, electrically insulating and very hard. Graphite, in contrast has a black color and is electrically conductive and a soft material. The change from sp^3 to sp^2 affects a change of the crystallographic structure from cubic to hexagonal. A single plane of graphite has nearly the same stiffness as diamond because of the in-plane sp^2 hybridized σ bonds. Graphite is highly electrically conductive, resulting from an overlap of the out-of-plane p orbital. In the direction normal to the planes graphite has a very low electrical conductance because of weak van-der-Waals interaction between the hexagonal planes. These two examples demonstrate the large differences in the structure and physical properties of carbon allotropes.

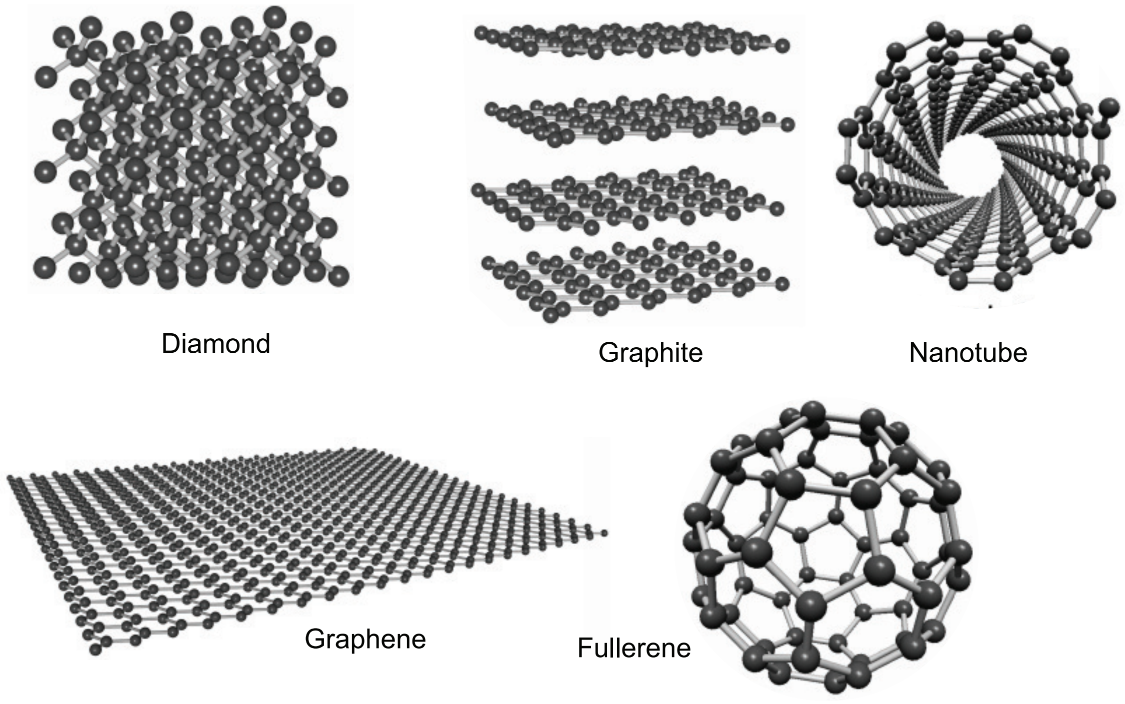

Figure 2.1: Carbon allotropes with a differing valence electron configuration and hence crystallographic structure. The models in this picture were made with VESTA^{TM} softwear.

Graphene, the central material of this thesis, has a structure identical to a single carbon layer of graphite, i.e. a hexagonal structure with sp^2 hybridized in plane σ bonds and p orbitals out-of-plane; these p orbitals are hybridized to form a π electron system. Therefore, graphene shows almost the same properties of a single layer graphite, except for weak van-der-Waals interaction between the graphite layers.

2.1 Free-Standing Graphene

A single graphene sheet is a planar layer of sp^2 hybridized C atoms arranged in a two-dimensional hexagonal or so-called honeycomb lattice with a lattice constant $c = |a| = |b| = 2.46\,\text{Å}$ [14, 15, 20, 21] as shown in *Figure* 2.2. The real space lattice vectors are marked as **a** and **b**

$$\mathbf{a} = \left(\frac{a}{2}, \frac{\sqrt{3}c}{2}\right), \qquad \mathbf{b} = \left(\frac{a}{2}, -\frac{\sqrt{3}c}{2}\right). \tag{2.1}$$

Each graphene unit cell contains two C atoms with an interatomic distance of 1.42 Å. The hexagonal C atom lattice is not a Bravais lattice because it is not possible to connect atom position A and B by a translation of an integer number of lattice vectors. However, it is possible to assign the two C atoms to two different sublattice

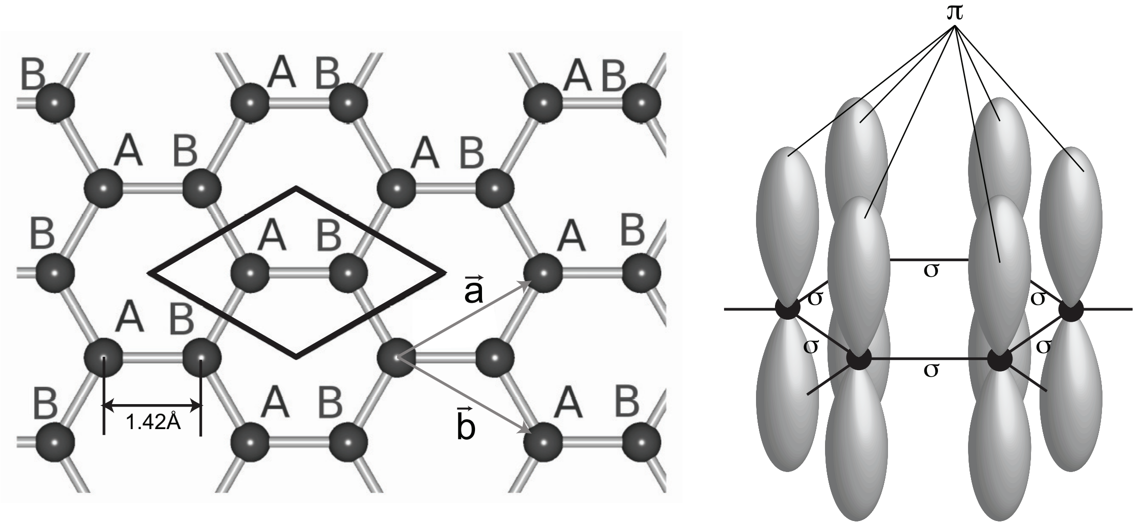

Figure 2.2: Crystallographic and molecular orbital structure of graphene: Two atomic sublattices, labeled A and B on the left-hand side of the figure are used to build the graphene sheet. The rhombus marks the Wigner-Seitz cell of the graphene lattice. The right-hand side of the figure shows the molecular orbital orientation of the sp^2 *hybridized C atoms.*

(labeled as A and B in the figure); this has important implications for the electronic band structure around the K point as discussed below.

The electronic band structure of the graphene π states can be described, in good agreement to experimental results, in a tight-binding model [1, 17, 19, 21]. This model is a good approximation for systems which have strongly localized electrons. Using Bloch's theorem [22] a basic wave function set $\Phi_j(\mathbf{k}, \mathbf{r})$ for the j th valence band can be created by Bloch functions summing over wave functions $\phi_j(\mathbf{r} - \mathbf{R}_{j,i})$ of the atomic orbitals in the i th unit cell modeled by a phase factor $e^{i\mathbf{k},\mathbf{R}_{j,i}}$, where $\mathbf{k}$ is the wave vector

$$\Phi_j(\mathbf{k}, \mathbf{r}) = \frac{1}{\sqrt{N}} \sum_{i=1}^{N} e^{i\mathbf{k}\mathbf{R}_{j,i}} \phi_j(\mathbf{r} - \mathbf{R}_{j,i}). \tag{2.2}$$

Here N is the number of unit cells. An electronic wave function can be created by the linear combination of n different Bloch functions using the coefficients of expansion $c_{j,l}$

$$\Psi_j(\mathbf{k}, \mathbf{r}) = \sum_{i=1}^{N} c_{j,l} \Phi_l(\mathbf{k}, \mathbf{r}). \tag{2.3}$$

Then the energy of the j th band is given by

$$E_j(\mathbf{k}) = \frac{\langle \Phi_j | H | \Phi_j \rangle}{\langle \Phi_j | \Phi_j \rangle}. \tag{2.4}$$

In the numerator H represents the Hamiltonian. By inserting *Function* 2.3 into *Equation* 2.4 we obtain

$$E_j(\mathbf{k}) = \frac{\sum_{i,l}^{n} c_{j,i}^{*} c_{j,l} \langle \Phi_i | H | \Phi_l \rangle}{\sum_{i,l}^{n} c_{j,i}^{*} c_{j,l} \langle \Phi_i | \Phi_l \rangle} = \frac{\sum_{i,l}^{n} H_{i,l} c_{j,i}^{*} c_{j,l}}{\sum_{i,l}^{n} S_{i,l} c_{j,i}^{*} c_{j,l}}. \tag{2.5}$$

The introduced matrix element $H_{i,l} = \langle \Phi_i | H | \Phi_l \rangle$ is often called the integral transfer matrix element and is divided by the overlap integral $S_{i,l} = \langle \Phi_i | \Phi_l \rangle$ in the energy relation. Minimization of the energy with respect to the coefficient $c_{j,m}^{*}$ by setting $\partial E_j / \partial c_{j,m}^{*} = 0$ and neglecting the factor $\sum_{i,l}^{n} S_{i,l} c_{j,i}^{*} c_{j,l}$, which is approximately one, leads to

$$\sum\nolimits_{i,l}^{n} H_{i,l} c_{j,l} = E_j \sum\nolimits_{i,l}^{n} S_{m,l} c_{j,l}. \tag{2.6}$$

Considering that the graphene unit cell contains two orbitals ($n = 2$) *Equation* 2.6 can be written as

$$\begin{pmatrix} H_{AA} & H_{BA} \\ H_{AB} & H_{BB} \end{pmatrix} \begin{pmatrix} c_A \\ c_B \end{pmatrix} = E \begin{pmatrix} S_{AA} & S_{BA} \\ S_{AB} & S_{BB} \end{pmatrix} \begin{pmatrix} c_A \\ c_B \end{pmatrix}. \tag{2.7}$$

Here the nearest neighbor approximation and the fact that the bonding to all three neighbors is equivalent are used. By comparison of coefficients and creating a secular equation, the derivation proceeds to

$$\det(H - E_j S) = 0. \tag{2.8}$$

The diagonal matrix elements of the Hamiltonian are given by

$$H_{AA} = H_{BB} \approx \frac{1}{N} \sum_{i=1}^{N} \langle \Phi_A(\mathbf{r} - \mathbf{R}_{A,i}) | H | \Phi_A(\mathbf{r} - \mathbf{R}_{A,i}) \rangle. \tag{2.9}$$

Within the sum, the integral is independent of the index i, because it is equal for every A and B site. This value is approximately equivalent to the energy of an electron in an atomic orbital ϵ_{2p}

$$H_{AA} = H_{BB} \approx \frac{1}{N} \sum_{i=1}^{N} \epsilon_{2p} = \epsilon_{2p}. \tag{2.10}$$

The calculation of the overlap diagonal elements proceeds in a similar way

$$S_{AA} = S_{BB} \approx \frac{1}{N} \sum_{i=1}^{N} \langle \Phi_A(\mathbf{r} - \mathbf{R}_{A,i}) | \Phi_A(\mathbf{r} - \mathbf{R}_{A,i}) \rangle = 1. \tag{2.11}$$

The off-diagonal matrix elements describe the process of hopping of the electrons between the A and B sublattices

$$H_{AB} = \frac{1}{N} \sum_{i=1}^{N} \sum_{l=1}^{N} e^{i\mathbf{k}(\mathbf{R}_{B,i} - \mathbf{R}_{A,l})} \langle \Phi_A(\mathbf{r} - \mathbf{R}_{A,i}) | H | \Phi_A(\mathbf{r} - \mathbf{R}_{A,l}) \rangle. \tag{2.12}$$

The nearest-neighbor approximation reduces the second sum to only three terms. Considering the translation symmetry the first sum and the normalization factor $1/N$ yield

$$H_{AB} = \sum_{j=1}^{3} e^{i\mathbf{k}(\mathbf{R}_{B,i}-\mathbf{R}_{A,j})} \langle \Phi_A(\mathbf{r}-\mathbf{R}_{A,i})|H|\Phi_A(\mathbf{r}-\mathbf{R}_{A,j})\rangle. \tag{2.13}$$

Moreover the equivalence of the three bondings allows to set

$$-\langle \Phi_A(\mathbf{r}-\mathbf{R}_{A,i})|H|\Phi_A(\mathbf{r}-\mathbf{R}_{A,j})\rangle \tag{2.14}$$

to a l independent value γ_0. It is common to summarize the remaining e function and sum to a $\mathbf{k}$ function $f(k)$ yielding

$$H_{AB} = -\gamma_0 f(k). \tag{2.15}$$

Inserting the coordinates of an A atom and the three neighboring B atoms into $f(k)$ leads to

$$f(k) = e^{ik_y a/\sqrt{3}} + 2e^{-ik_y a/\sqrt{3}} \cos(k_x a/2). \tag{2.16}$$

The other off-diagonal element is the complex conjugate $H_{BA} = H_{AB}^*$.The calculation of the overlap integral runs similar yielding

$$S_{AB} = s_0 f(k), \qquad S_{BA} = s_0 f^*(k). \tag{2.17}$$

Summarizing these results the secular equation (*Equation* 2.8) can be solved.

$$\det\left(\begin{pmatrix} \epsilon_{2p} & -\gamma_0 f^*(k) \\ -\gamma_0 f(k) & \epsilon_{2p} \end{pmatrix} - \begin{pmatrix} E & s_0 f^*(k) \\ s_0 f(k) & E \end{pmatrix}\right) = 0 \tag{2.18}$$

$$(E-\epsilon_{2p})^2 - ([E-\epsilon_{2p}]s_0 + \epsilon_{2p}s_0 + \gamma)^2 |f(k)|^2 = 0 \tag{2.19}$$

$$E_\pm = \frac{\epsilon_{2p} \pm \gamma_0 |f(k)|}{1 \mp s_0 |f(k)|} \tag{2.20}$$

The resulting band structure is shown in *Figure* 2.3. For more details of this derivation see E. McCann [21]. Parameters ϵ and γ_0 have to be calculated from other theories such as density-functional theory. It is common to set the parameter ϵ_{2p} to 0 meaning the zero energy is set to the energy of an electron in a p_z orbital. *Equation* 2.20 clarifies an asymmetry between the E_+ and the E_- bands which arises from the overlap parameter s_0. At the corners of the Brillouin zone, six Dirac cones occur distinguished in two types labeled as K_+ and K_- in *Figure* 2.3. Dirac cones of the same type are connected by reciprocal lattice vectors. Further important facts are the position of the Fermi energy and the dispersion in the vicinity of it. In pristine graphene, the Fermi level appears exactly at the touching point of the E_+ and the E_- solutions where density of states vanishes. Therefore pristine graphene is a gapless semiconductor or a so-called half metal. The good agreement of the tight-binding model results with experimental data indicates that in graphene the structure of the p orbitals are mainly preserved and these orbitals have a small overlap with each other. Otherwise the use of the p_z orbital functions as the basis wave function in the Bloch functions and the approximation $\langle S_{AA}\rangle = 1$ would lead to large differences between the theoretical and the experimental results. The approximately linear dispersion around the K points allows to describe the electronic states by a Dirac-like Hamiltonian for massless particles. In the following an index $\kappa = \pm 1$ is used to distinguish both types of K points. The positions of two different K points in k space are

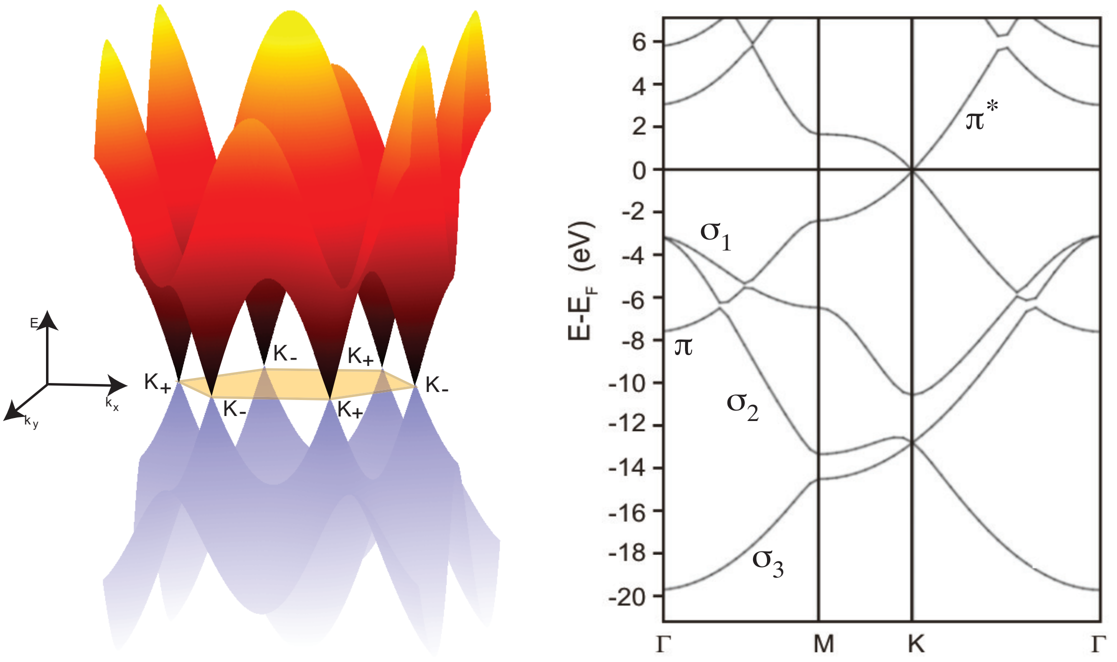

Figure 2.3: Electronic band structure of free-standing graphene in a tight-binding approach: The yellow hexagon marks the Brillouin zone and the position of the Fermi level. Based on the separation into two distinct sublattices two different types of K points are labeled as K_+ and K_-.

$$\mathbf{K}_\kappa = \kappa\left(\frac{4\pi}{3a}, 0\right) \tag{2.21}$$

with respect to the reciprocal lattice vectors. In the tight-binding model the off-diagonal matrix elements describe the coupling between both sublattices A and B. These matrix elements are proportional to γ_0 and the function $f(\mathbf{k})$. Exactly at the K points the function $f(k)$ is

$$f(\mathbf{K}_\kappa) = e^0 + e^{i\kappa 2\pi/3} + e^{-i\kappa 2\pi/3} = 0. \tag{2.22}$$

Therefore the coupling of the sublattices is zero for electron states exactly at the K points. Electrons of these states belongs to the A or to the B sublattice. Since both sublattices are hexagonal Bravais lattices, they support the same quantum state leading to a degeneracy at this point.Introducing an new momentum $\mathbf{p}$ centered at K_κ changes $f(k)$ to

$$\mathbf{p} = \hbar\mathbf{k} - \hbar\mathbf{K}_\kappa \tag{2.23}$$

$$f(\mathbf{k}_\kappa) \approx -\frac{\sqrt{3}a}{2\hbar}(\kappa p_x - p_y) \tag{2.24}$$

The approximation in *Equation* 2.24 considers only linear terms of p in $f(k)$, an approximation which is valid close to the K points [21]. Using the this approximation and set $\epsilon_{2p} = 0$ the transfer matrix element becomes

$$H_\kappa = v \begin{pmatrix} 0 & \kappa p_x - ip_y \\ \kappa p_x + ip_y & 0 \end{pmatrix}. \tag{2.25}$$

Here parameter a and γ_0 are combined to a velocity $v = \sqrt{3}a\gamma_0/2\hbar$. Since the S off-diagonal elements contains only quadratic momentum terms which are set to zero in the approximation, S can be regarded as an unit matrix. *Equation* 2.8 changes to $H\Psi = E\Psi$ indicating that *Equation* 2.25 is an effective Hamiltonian in the vicinity of the K points. The eigenvalue and the eigenstates of H are

$$E_\pm = \pm vp, \qquad \Psi_\pm = \frac{1}{\sqrt{2}}\begin{pmatrix} 1 \\ \pm\kappa e^{i\kappa\varphi} \end{pmatrix}. \tag{2.26}$$

Here ± refer the the conduction and the valence band, respectively. φ is the polar angle in the graphene plane $p = p(\cos\varphi, \sin\varphi)$. Thus the linear dispersion and the massless behavior appear at the point where the valence and the conduction bands meet, the electrons have a very high velocity. In cyclotron resonance experiments on decoupled graphene values of $10^7\,\mathrm{cm}^2/(\mathrm{V{\cdot}s})$ [8] were measured. Such high values, which lead to large charge carrier mobilities have brought about the intense interest in graphene from an applications-oriented point of view, where one goal is their use in electronic devices.

2.2 Graphene on Different Substrates

The investigation of graphene on a variety of substrates, and the interaction between them and graphene plays an important role on the way to graphene based electronic devices, since completely free-standing graphene devices are restricted to laboratory samples [14]. Interactions such as doping, hybridization or van-der-Waals interaction are often observed in many systems. For the preparation of graphene on different substrates several preparation methods are known and have been used for decades. The most important methods are exfoliation, decomposition of SiC and the growth of graphene by segregation from the crystal bulk or the cracking of carbon-containing molecules. Here I will give a short overview about three example systems: graphene on $\mathrm{SiO_2}$/Si, SiC and Ir(111).

Graphene on SiO_2/Si

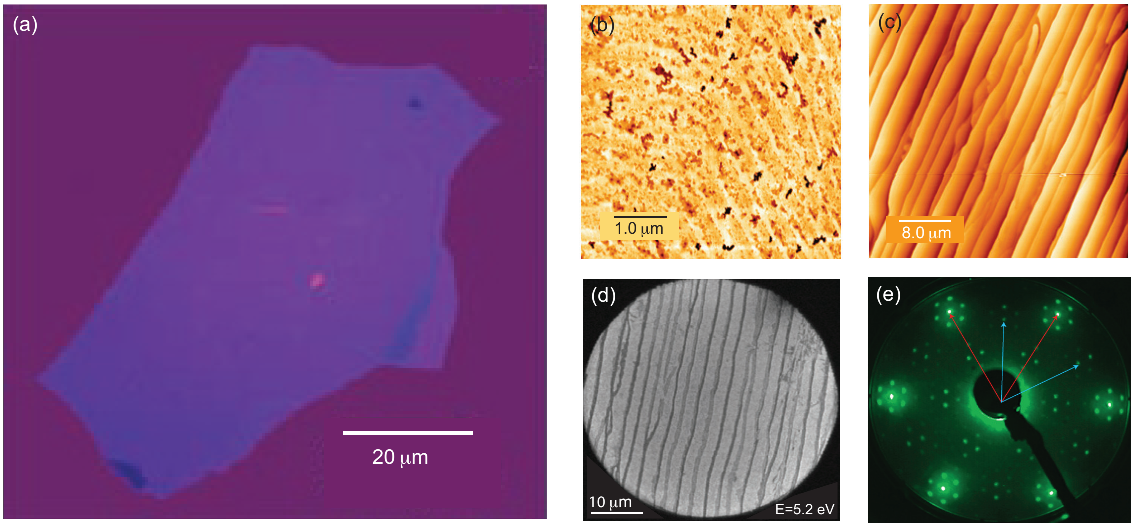

Figure 2.4: Microscopic and LEED pattern images of graphene on SiO_2/Si and SiC: (a) shows a graphene flake on SiO_2/Si prepared via the "scotch-tape" method [23]. AFM measurements (b) and (c) reveal large differences in the roughness of SiC samples prepared under UHV conditions and samples prepared in an Ar atmosphere [24]. AFM images (c), LEEM images (d) and LEED pattern (e) shows graphene on SiC grown at 1650° C in 900 mbar inert Ar atmosphere [24].

Graphene on SiO_2/Si can be prepared by mechanical exfoliation. This method starts by pressing a sticky tape (Scoth tape, Tesafilm) on a piece of graphite. Carefully removing the tape still leads to thin slices of graphene fixed to the tape. Now another piece of tape is pressed onto the reverse of the graphene slice, and this process is repeated until the slices are extremely thin as judged by eye. They are then pressed onto a silicon wafer, and monolayers of graphene can be identified visually; an important aspect of this optical identification is that the oxide on the silicon wafer has a specific thickness ($\approx 300\,\text{Å}$).

In the famous experiments on graphene/SiO_2/Si published in 2004 by Novoselov and Geim they found that electrons show two-dimension ballistic transport properties at submicrometer distances [23]. Such ballistic behavior had already been observed in carbon nanotubes before [25]. The charge carriers in this system have a mobility of 3,000-10,000 $\text{cm}^2/(\text{V}\cdot\text{s})$ at 300 K and have equal magnitude for electrons and holes [5]. The large difference of the experimental results was attributed to differences in the defect density or, in other words, to the quality of the flakes. The influence of a vanishing density of states of the charge carriers could not be observed; instead, a finite resistance was found [5, 6]. While these observations demonstrated, for the first time, the massless "Dirac Fermion" nature of charge carriers in graphene, it also showed that this material by itself has some restrictions for use in digital switching devices; in order to be useful for the latter it is necessary to create a band gap to permit switching between different types of charge carriers. Further they demonstrated that few-layer graphene can work as a hole or electron field-effect transistor obtaining an (albeit quite small) band gap between the π and π^* bands. The barrier which inhibits the use of the extrafoliation method for graphene preparation in electronic device production is the limited size and the varying orientation with respect to substrate of the graphene flakes. Advantages of this method are the high quality of the resulting graphene and the multitude of substrate which can be used.

Graphene on SiC

A more promising approach to industrial production of graphene is the decomposition of SiC. SiC occurs in several crystalline modifications, the so-called polytypes [26, 27]. All polytypes are semiconductors, exhibiting band gaps in the range from 2.39 to 3.27 eV [17].

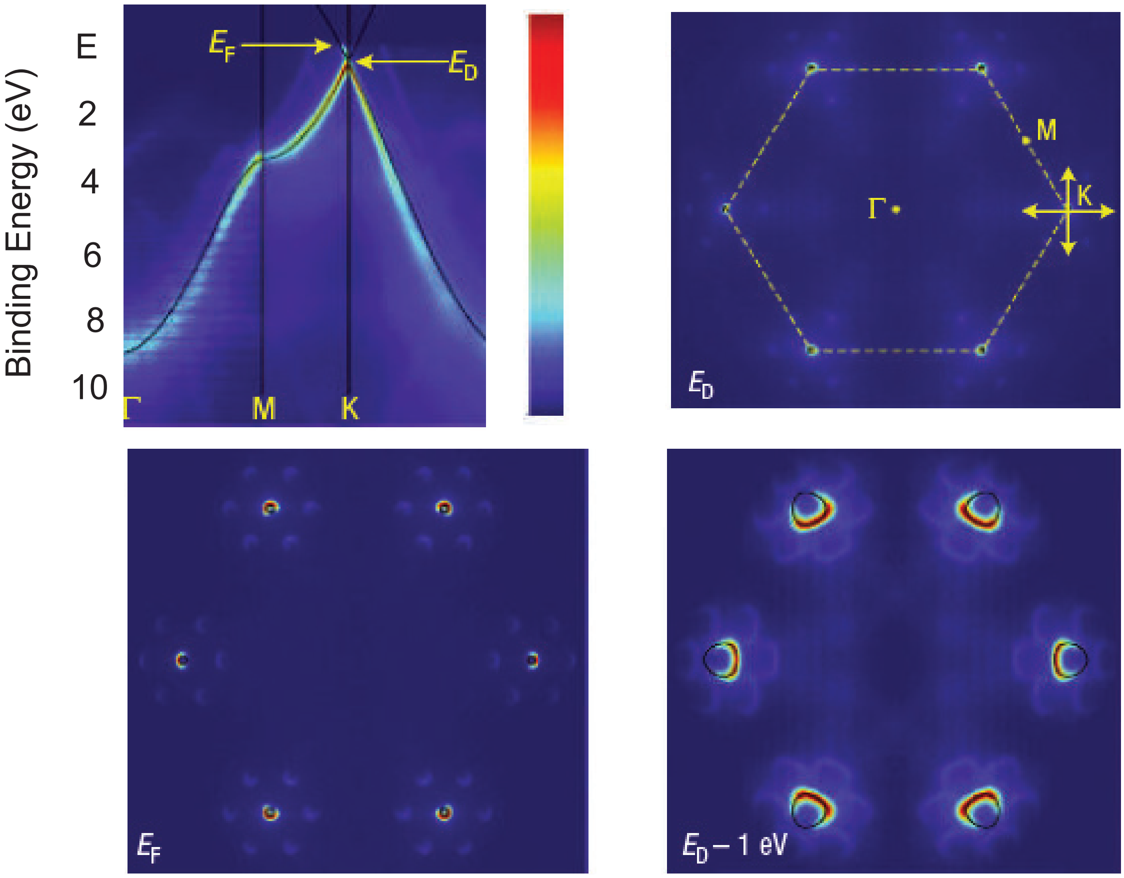

Figure 2.5: Valence bandmap and constant energy cuts of graphene on SiC: In (a) a downwards shift of the π states is visible ascribed to an electron transfer from SiC to graphene. Originating from the reconstruction satellite features appear arranged in a hexagonal structure around the K point (figure deduced from [28]).

The formation of graphene on SiC is based on the element-specific decomposition of the SiC surface at higher temperatures. Si atoms desorb from a silicon carbide surface at lower temperatures, less than 1280° C compared to C atoms. Under UHV conditions, in a temperature range from 1000° C to 1500° C the Si atoms evaporate from the surface and the remaining C atoms form graphene up to thicknesses of several layers [29, 30]. Thermal decomposition in ultrahigh vacuum is a viable method for graphene preparation; however, as is evident from the AFM micrograph in Figure 1.4 the surfaces thus prepared are quite rough on an atomic scale. Thus in order to improve the quality of the graphene layer, several variations of this method were developed. Emtsev *et al.* found that the roughness of the graphene/SiC surface is strongly reduced if the crystal is heated under an Ar atmosphere [24] (see Figure 1.4 c and d. Juang *et al.* synthesized graphene at 750° C by using a 200 nm Ni coated SiC crystal [31]. Further, an interesting procedure for large scale production is the transfer of graphene to any kind of substrates. Ways realizing a transfer of graphene grown on SiC to different substrates were reported by Unarunotai *et al.* in 2009 and 2010 [32, 33]. The hexagonal surface of silicon carbide is interesting for technical applications. This surface can be terminated by C or by Si atoms (so-called C-face or Si-face respectively). The surface atoms on the Si-face form a $(6\sqrt{3} \times 6\sqrt{3})R30°$ reconstruction, in contrast the surface atoms on C-face [27]. This different behavior has a strong influence on the growth and properties ofof the graphene layer. After the growth of one ordered C atom layer on the Si-face indicated by reconstruction spots in the LEED pattern and clear σ bands in the ARPES results, no clear π band can be observed. The π states are reduced to two strongly localized states at 0.5 eV and 1.6 eV binding energy [34, 35]. No graphene states appear at the Fermi level, hence this layer is insulating. Because of the large differences in the electronic structure compared to graphene, this first C layer on the Si-face is called the buffer or zero layer. This buffer layer saturates the dangling bonds [29, 36, 37]. Only the second layer shows the band structure as known from graphene; it is n-doped by about 450 meV. *Figure* 2.5 shows ARPES data on this graphene layer, the π band is clearly visible similar to the graphene π states in *Figure* 2.3 shifted slightly downwards to higher binding energies. This shift is ascribed to n-doping from the substrate to the graphene layer. Further six satellite bands occur in constant energy cuts around the K points; they are created by the influence of the reconstruction [28]. The growth of large high quality graphene areas and the fact that it is possible to open a band gap by applying a gate voltage [38–42] are promising prospects for future electronic applications. The method to remove the graphene from the SiC crystal gives the opportunity to use SiC as a graphene source for other systems. However the mobility of electrons in graphene on Si is strongly reduced compared to exfoliated graphene. For graphene prepared under UHV conditions and in an Ar atmosphere, values of 1,200 $cm^2/(V{\cdot}s)$ for the former and from 1,850 $cm^2/(V{\cdot}s)$ to 2000 $cm^2/(V{\cdot}s)$ for the latter case were observed in contrast to the mobility of 10,000 $cm^2/(V{\cdot}s)$ to 40,000 $cm^2/(V{\cdot}s)$ observed in exfoliated graphene [5, 6]. This indicates that the quality of exfoliated graphene is higher compared to graphene grown on SiC. Field-effect transistors built using graphene on SiC show mobilities from 600 $cm^2/(V{\cdot}s)$ to 1,200 $cm^2/(V{\cdot}s)$ by using the Si-face and 5000 $cm^2/(V{\cdot}s)$ by using the C-face [43].

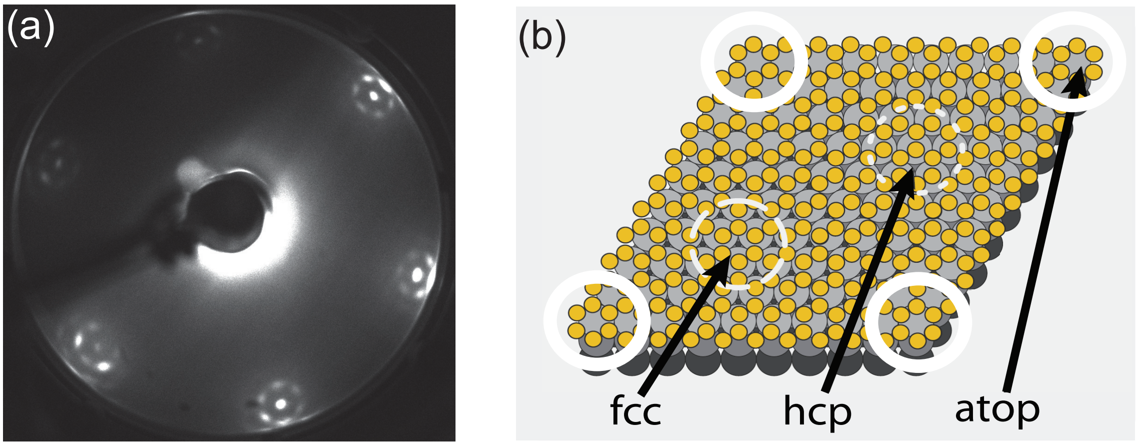

Figure 2.6: LEED pattern and structure model of graphene/Ir(111): (a) The Moiré pattern is indicated by additional diffraction spots in the LEED image. (b) shows an atomic structure model. (Figure taken from [60].)

Graphene on Metals

With the enormous interest in graphene, and the fact that carbon layers on transition metals are well known and have been studied for decades, a large number of studies have dealt with graphene growth on metals such as Ni, Co, Fe, Pd, Pt, Ir, Rh, Re, Ru, as well as Cu, Ag, and Au. A summary of the possible metal substrates was published by Wintterlin and Bocquet [16], but the list has become much larger in recent years. Two different processes are often used for graphene preparation on metals: First, segregation of C atoms from the bulk to the surface, and second, cracking of hydrocarbons on the hot metal surface. The process of cracking hydrocarbons is well known: first reviews related to this topic were published in 1991 [44–46]. At present, the method shows the largest progress on the way to the large scale growth of graphene [47, 48] (see also *Figure* 2.8). Segregation works via heating the crystal to higher temperatures. C atoms move from the bulk to the surface and form graphene. The number of layers is defined by the C atom concentration in the metal close to the surface, the heating time and the cool-down rate [16, 49–52]. Which process is used, segregation or cracking, depends strongly on the substrate material. Note that both process can occur simultaneously. On closed-packed metal surfaces graphene shows two different structures [53]. If the metallic substrate has a lattice constant that is close to that of graphene, a commensurate surface structure occurs, and graphene forms a flat layer on the metal. This is the case for graphene/Ni(111) [54], but also for Co(0001) and Cu(111). Systems in which the lattice mismatch is large (more than a few percent), an incommensurate structure is formed, a so-called corrugated moiré surface morphology such as on Ir(111) [55], Rh(111) [56] and Ru(111) [56–59]. A Moiré pattern results from a superposition of two symmetric structures which show different lattice constants, and/or a rotation angle with respect to each other.

Let us discuss the consequences of the moiré pattern on the electronic band struc-

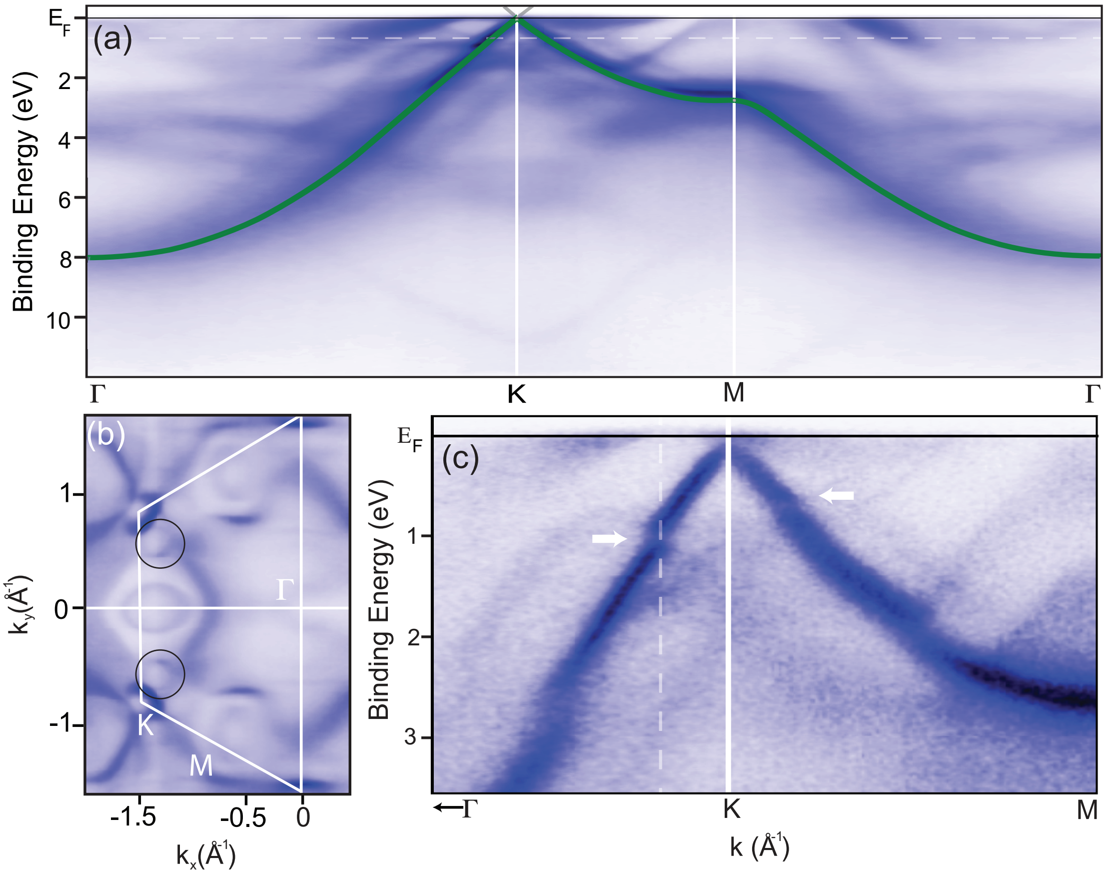

Figure 2.7: Band maps and constant energy cut of graphene on Ir(111) taken at $h\nu = 120\,eV$ *photon energy: (a) and (c) show a band map along the high symmetry axis and detailed map around the K point, respectively. White arrows mark the minigaps, which arise from the interference of the satellite and main features [61]. (b) shows a constant energy cut at 0.6 eV binding energy. Black circles mark two satellites; the others are hardly visible.*

ture through the example of graphene/Ir(111). In STM measurements on graphene Ir(111) a moiré pattern of (9.32 x 9.32) with respect to the graphene unit cell was observed, arising from the different sizes of the lattice vectors of graphene (about 2.46 Å and Ir(111) (2.715 Å) [60]). The resulting lattice mismatch is reflected in LEED measurements as additional diffraction spots surrounding the main graphene spots which are shifted by the lattice vectors. In STM measurements graphene shows a corrugation of 0.3 Å in the direction perpendicular to the surface [60]. In the ARPES spectra shown in *Figure* 2.7, satellite features surround the Dirac cones appearing in constant energy cuts, similar to graphene/SiC (see also *Figure* 2.5) [61]. Two explanations for the origin of the satellites come to mind. First, in the movement of the photoexcited electron through the solid the electron wave functions interfere at the corrugated graphene layer; such a scenario is called final state effect, and the satellite features do not exist in the band structure. In the second scenario, the electron wave functions feel the corrugation and the additional symmetry of

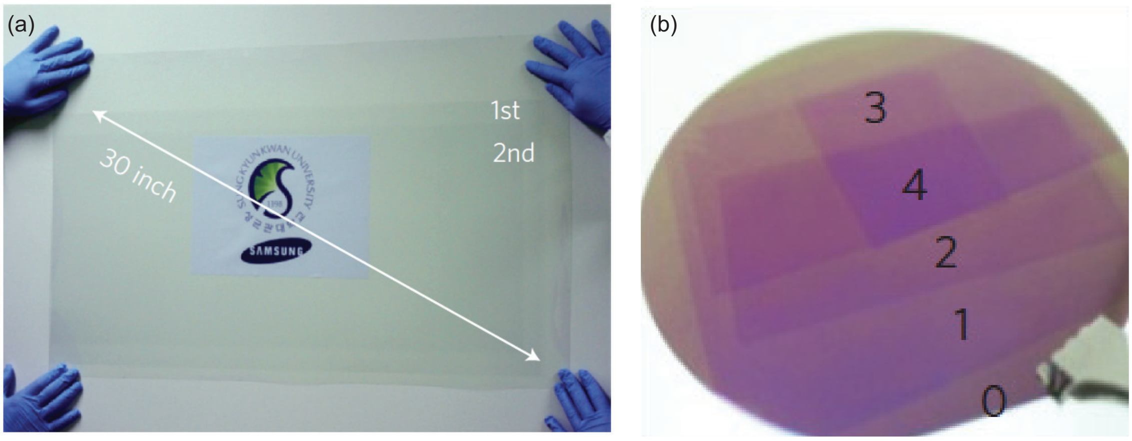

Figure 2.8: Examples of large scale graphene production: (a) shows 30 inch size graphene sheet transferred to a (PET) (b) shows a graphene stack which was deposed in a layer-bylayer transfer on a SiO_2/Si wafer.

the combined substrate-overlayer system. In this case, the corrugation influences the band structure and the additional satellites have to be taken into account in a description of the electronic properties, such as conductivity. Using symmetry aspects Starodub *et al.* assigned the observed satellites to a final state effect [62]. The coexistence of several orientations was identified in ARPES spectra , e.g. the so-called R0 and R30 orientations. R0 refers to domains which are aligned to the Ir(111) these domains shows the Moiré pattern and satellite structures as discussed above. The R30 domains stay on top of Ir(111) as a flat, almost non-interacting layer, and satellites cannot be observed.

The state of the art in large scale graphene preparation uses chemical vapor deposition (CVD) on top of Cu. Graphene is prepared at 1000° C in a constant gas flow of H_2 and CH_4 [63]. In a next step a polymer support is added. The Cu layer is removed by chemical etching, and the graphene layer is transferred to a polyethylene terephthalate substrate. The graphene film shows all the attributes of monolayer garphene, from Raman spectra, the half-integer quantum Hall effect, and the optical transparency. The work of Bae *et al.* [47] demonstrates in an impressive way that large scale fabrication is already a reality. Based on this method, graphene can be provided as a raw material for electronic devices in wafer sizes. In graphene grown on polycrystalline Ni foils and subsequently transferred to SiO_2 mobilities up to 3,700 $\mathrm{cm}^2/(\mathrm{V{\cdot}s})$ and a very low resistance down to 280 Ω were observed [64]. This mobility is considerably larger compared to graphene on SiC.

2.3 Possible Applications of Graphene

After solving the problem to store huge amounts of data by developing the GMR technique by Grünberg and Fert [65, 66], which is used in hard disk read heads, the challenge of the next decade is to find ways to handle and analyze large amounts

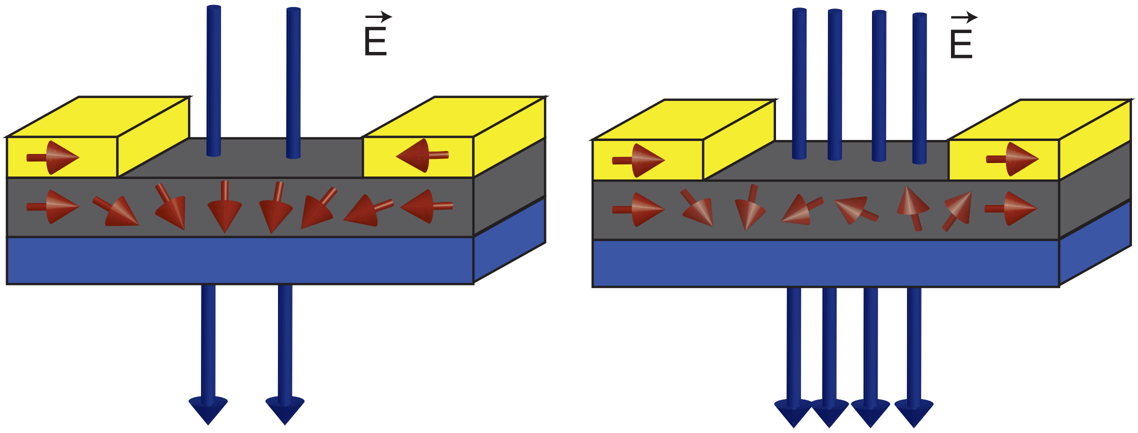

Figure 2.9: Working principles of an SFET: The left scheme present the situation of the half spin state rotation. The electrical field intensity can be used to tune the rotation velocity of spin moment as shown in the right scheme.

of data in a reasonable time. In the field of applied graphene research, several approaches were suggested in order to improve computer processing speed. Two of these are introduced here. The spin field effect transistor (SFET) leaves the notion to transfer information based on an electron current in favor of using the electron's spin as a carrier of information. This avoids the heating of the transistor because of the lack of electron phonon scattering events in transport processes. Another concept, so-called spin filter devices, focus on the increase of the data density. This can be done by increasing the number of states in one bit. At present one bit uses the states zero and one transferred in devices by applying a voltage or not. This gives the possibility to use the states 'no-current", "spin-up current" and "spin-down current". This is equivalent to a change from binary-valued logic to the three-valued logic. The data density is defined by the number of possible states; for example, a binary-valued logic byte has $2^8 = 256$ states. In a three-valued logic, one byte has $3^8 = 6561$ states. This increase in the number of possible states motivates applied sciences researchers in this topic. However the change to such spintronic devices means to use magnetic fields in computer chips, a physical parameter which computer scientists try to avoid at present. Thus the development of this technique starts from the ground.

2.3.1 Spin Field Effect Transistor

One of the most interesting properties of graphene is the long spin life time of ≈ 6.2 ns [9], bringing graphene into the focus of spintronic application research. An electron with a defined spin can travel over large distances before the spin states is destroyed by scattering, and such a long spin life time is ideal for the use in spintronic devices. One idea is to introduce a defined spin state into the graphene layer at one electrode, e.g. the left one in *Figure* 2.9. This spin state propagates now from the left electrode as a spin wave to the right electrode. At the right electrode, the spin state is detected.

Also, the the relativistic behavior of the electrons in graphene may permit spin manipulation. A relativistic particle senses an external electric field as a external magnetic field in contrast to non-relativistic particles. In graphene electrons at the Fermi level behave like mass less relativistic Dirac particles. Therefore, the external electrical field couples magnetically to the particle spin and not to the electronic charge leading to the rotation of the spin orientation with distance as shown in *Figure* 2.9. The distance for a complete rotation can be tuned by changing the magnitude of the external electric field. The preparation of a graphene layer on top of Ni is favorable for this because of the existing magnetization of the Ni substrate. This magnetization can be used to introduce a ground state of the spin orientation which can be influenced from an outer electric field without affecting the magnetization. The motivation to change from the well known established technology to such a complex system arises from the information transport which does not involve a current. The electrons at the Fermi behave like relativistic particle even without a voltage. The signal in a SFET spreads as a spin wave.

2.3.2 Spin-Filter

The principle of a spin filter device is that only one spin species participates in the transport process. Therefore a spin filter can be realized by creating a sufficient energetic splitting between spin-up and spin-down states as shown in a hypothetical band structure in *Figure* 2.10 (a). Promising systems for this approach are half-metal ferromagnets which show a spin dependent metal or insulator behavior [67, 68]. In these materials, a suitable band gap exists at the Fermi level only for bands of specific spin. In that case the spin selection is energetically resolved. Unfortunately such materials are highly sensitive to structural disorder and impurities [67, 68]. Therefore they are not implemented in computers yet.

Another approach is to use a **k**-resolved spin selection. For this, two different band structures are required, i. e. heterojunctions. If electrons move from material A into material B, empty states in B at the same point of the Brillouin zone are necessary, otherwise an additional scattering event is required to shift the electron state to the position of the empty states in material B. This additional condition decreases the transmission probability and thus leads to an increase of the interface resistivity. Karpan *et* al. found in calculations of the spin-resolved Fermi surface projection of the Ni bulk states onto the (111) surface, that the valence band structure has no majority spin states at the K points of the Brillouin zone, in contrast to the minority spin states which shows an increased value there [12, 67] (see *Figure* 2.10 (b)). This fact and the commensurate structure of the graphene/Ni(111) interface suggest this system for spin filter devices, if the heterojunction has no commensurate crystallographic structure the band structures of both materials will overlap at different positions as shown in *Figure* 2.10 (c). The K point of the solid line Brillouin zone occurs at different position of the broken line Brillouin zone.

A single atomic layer is not an efficient electron barrier, because the tunneling probability is significant. In the case of single layer graphene the transmission

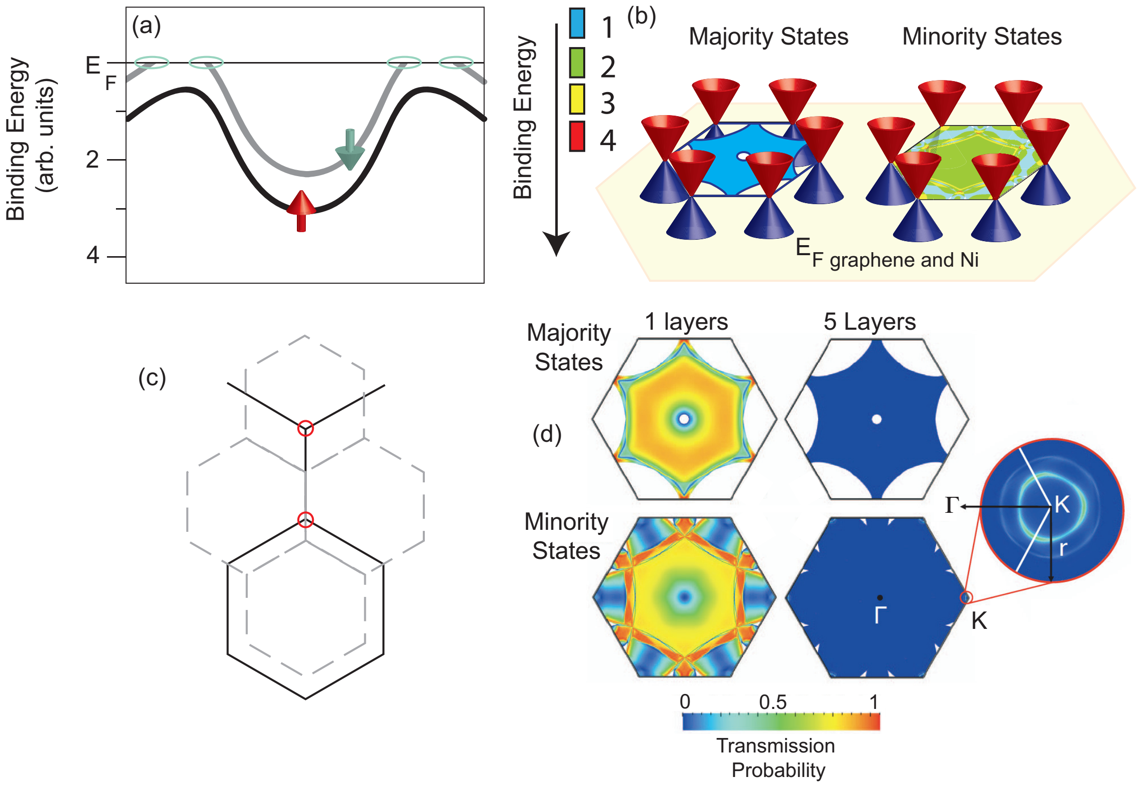

Figure 2.10: Valence band and transmission probability: (a) shows a hypothetical band structure of a half-metal ferromagnet exhibiting ad band gap for only one spin species. The Dirac cones of the graphene π bands in (b) touch only minority spin state density at the Fermi level. (c) incommensurate crystallographic structures in heterojunctions lead to the occurence of the K points of the solid Brillouin zone at several different points of broken gray line Brillouin zone.(d) shows the transmission as a function of $\boldsymbol{k}$ *and number of layers for Ni/n ML graphene/Ni junctions (n=$\{2,5\}$). (density of Ni(111) states and transmission data are deduced from [12])*

current has two compponents $I_{transmission} = I_{spindepend} + I_{tunneling}$. Depending on the tunneling probability, the efficiency of the spin filter device is reduced. Karpan *et* al. obtained a saturation of the spin filter efficiency for coverages of more than five graphene layer. Every layer reduces the tunneling probability, but this does not affect the minority transmission probability because the minority transmission condition is valid for every layer.

Note that electrons close to the Fermi energy of one spin species do not feel the barrier of the heterojunction. Therefore these electrons delocalise over the whole junction; in contrast the electrons of the opposite spin orientation remains in material A. As a consequence the spin filter is active even without voltage i.e. coupling exist already. Following by switching spin transmission configuration it is possible to transfer information current-less. Unfortunately the number of states in this working mod is reduced to spin up and spin down because of the lack of current and no-current states.

It has to be emphasized that in this model, the ideal band structure of free-standing graphene, i.e. the Dirac cones near the Fermi level, was used. This ideal band structure is not, however, preserved after adsorption of graphene onto the Ni(111) surface as shown in *Chapter* 7. Karpan *et al.*, in their study of 2008 propose to decouple the graphene stack by intercalation of noble metals such as copper; this is thought to preserve the spin filter efficiency. The chances and the perspectives for the applications of graphene as spin-filter are discussed in *Chapter* 5, 6.1 and 7.

Chapter 3

Experimental Methods

This chapter gives an introduction to the methods used starting with the physical principles of the methods and continuies with a description of the data treatment.

3.1 The Photoelectric Effect

In the past, a lot of work has been done on the aspects of the photoelectric effect and the possible applications, following the publication of text books [69–71] and reviews about the general problems and effects [72–78] to the very specific details discussions were published [79–83].

Photoelectron spectroscopy is based on the excitation of electrons from an initial state into an unoccupied final state by absorption of photon. If the photon energy is high enough the electron can be excited into unbounded continuum states above the vacuum level. In case of solids this final state can belong to a continuum above the vacuum level in which the electron can now travel through the solid and escape into the vacuum. If this final state is above the vacuum level the electron can escape from the surface. Father and son, Antoine and Henri Becquerel observed already in 1839 that a metal plate becomes discharged, if it is exposed to light [84]. In 1902 Lenard [85, 86] found the $E_{\mathrm{kin}} \sim 1/\lambda$ dependence of the kinetic energy of the electrons on the reciprocal wavelength of the light, which contradicted the linear dependence of the kinetic energy on the photon flux expected from classical physic. The correct description of this process was developed by Einstein in 1905. Einstein described this effect by a single photon which transfers its energy to a single electron [87]

$$E_{\mathrm{kin}} = h\nu - E_{\mathrm{binding}} - \Phi. \tag{3.1}$$

E_{kin} represents the kinetic energy of the electron after it escaped from the surface into the vacuum, which is given as the difference between the energy of the incoming photon $h\nu$ and the binding energy of the electron in the solid E_{binding} plus the work function Φ. This was one of the first experimental demonstrations of the, at that time young, quantum theory. Later on, several fields of application were developed such as X-ray photoelectron spectroscopy (XPS) [72, 88], ultraviolet photoelectron

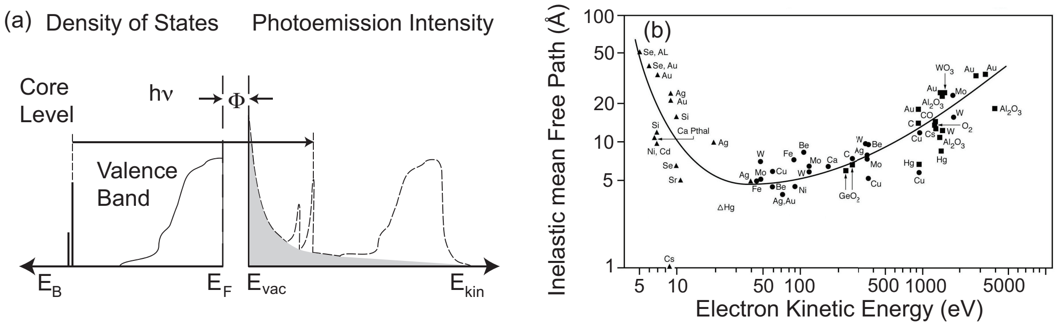

Figure 3.1: The dashed line in (a) gives the typical shape of a PES spectrum. According to the energy conservation low and regarding final state effects, secondary electron signal and cross section of the PES effect the PES intensity can be assigned to the electronic density of states (DOS) of the sample. The gray colored area marks the secondary electron signal. These are electrons which were involved in inelastic process after the excitation and appear at smaller kinetic energies. (b) presents the "universal" curve which give the inelastic mean free path of an electron in a solid (deducted from [89]).

spectroscopy (UPS), near edge X-ray absorption fine structure spectroscopy (NEXAFS) and more. UPS and XPS are distinguished only by the photon energy region which is used which makes them sensitive to different electronic states. The photon energy for UPS measurements ranges from 5 eV to 100 eV and for XPS from 100 eV to several keV but these numbers are not hard limits. Ultraviolet light is more sensitive to the valence band electron states and first atomic layers.

Because of the smaller cross section of absorption XPS measurements are not so sensitive to the valence band energy region but the photons have enough energy to excite electrons from the deeper core-levels. In a NEXAFS experiments the scan runs over the photon energy of an element specific absorption edge of a contained element and gives a view of the unoccupied state above the Fermi level.

Three Step Model

The three step model describes the photoemission process in a very simplified picture, separating the process into three different process steps, which are affected by different physical phenomena. It starts with excitation of an electron via absorption of a photon. The second step describes the motion of the electron through the solid. The final step deals with the influence of the escape from the surface.

1. *The excitation and Fermi's Golden rule*: The excitation probability P of the photoemission (PE) process can be described as a perturbation of the electronic ground-state $|i\rangle$ by an incident electromagnetic field which excites an electron into a free state $|j\rangle$ above the Fermi level E_F. Using first order perturbation theory, this

process is described by Fermi's golden rule

$$P_{ij} = \frac{2\pi}{\hbar}\frac{e^2}{4m^2}\left|\langle j\left|\hat{\mathbf{p}}\mathbf{A} + \mathbf{A}\hat{\mathbf{p}}\right| i\rangle\right|^2 \rho_j(E\delta_E\delta_{\mathbf{k}}\delta_J, \tag{3.2}$$

with $\mathbf{A}$ the vector potential of the electromagnetic field, $\hat{\mathbf{p}}$ the momentum operator and ρ_j the density of final states. Nonlinear terms in $\mathbf{A}$ are neglected. This equation determines the excitation probability $P_{i,j}$, with the delta functions ensuring the conservation of energy (δ_E), momentum ($\delta_\mathbf{k}$) and angular momentum (δ_J) (such as spin and orbital momentum). The momentum of the photons is three orders of magnitude smaller for photon energies used in UPS and XPS than the momentum of the electrons and can be neglected in this process. Due to energy and momentum conservation, the excited electron carries information about the energy and the momentum of the ground and the excited state. The transition energy and the momentum in the detected final-state can be affected by correlation and relaxation effects during the photoemission process [69]. Based on the fact that this influence is not related to the ground state, these effects are summarized in the so-called final state effects. During the motion though the solid, the electron can interact with its environment. These interactions are also added to the group of final-state effects and are discussed in the next paragraph.

2. *Motion through the solid*: The excited electrons move through the solid and scattering processes inevitably happen. During these scattering events the energy and the momentum of the scattered electrons are changed. Only unscattered electrons carry the information on the excited state. The signal of electrons which were involved in one or more inelastic scattering processes appears as continuously growing background at low kinetic energies in the PE spectrum, drawn as a gray area in *Figure* 3.1 (a). The inelastic scattering leads to a limited mean free path of electrons in a solid, depending on the kinetic energy of the electrons as illustrated in *Figure* 3.1 (b). In this curve, a clear minimum exist around $E_\mathrm{kin} = 50\,\mathrm{eV}$ [69, 90]. For kinetic energies of less than 50 eV the scattering process is determined by electron-electron interaction in contrast to kinetic energies above 50 eV where mainly phonon-electron interactions occur [91]. The probabilities of these simultaneously occurring interactions lead to the minimum in the mean free path. This minimum is the reason of the high surface sensitivity of UPS measurements, where electrons have typically kinetic energies between 20 eV and 100 eV after the excitation. Photons of higher energies such as in XPS measurements can transfer several hundred eV to the excited electron and therefore the mean free path length reaches several nm. This has to be kept in mind for comparison of data taken at different photon energies, where not only the cross section is different but also the sensitivity to different sample regions. While traveling through the solid, the electron can interact further with quasiparticles such as plasmons and phonons [69]. Interaction effects with quasiparticles are assigned to the final-state effects.

3. *Escape from the surface*: The escape from the surface is strongly affected by the broken lattice symmetry at the crystal-vacuum interface. Momentum conservation in a particular direction demands translational symmetry, which is not preserved perpendicular to the surface leading to a change of $\mathbf{k}_\perp$ at the interface.

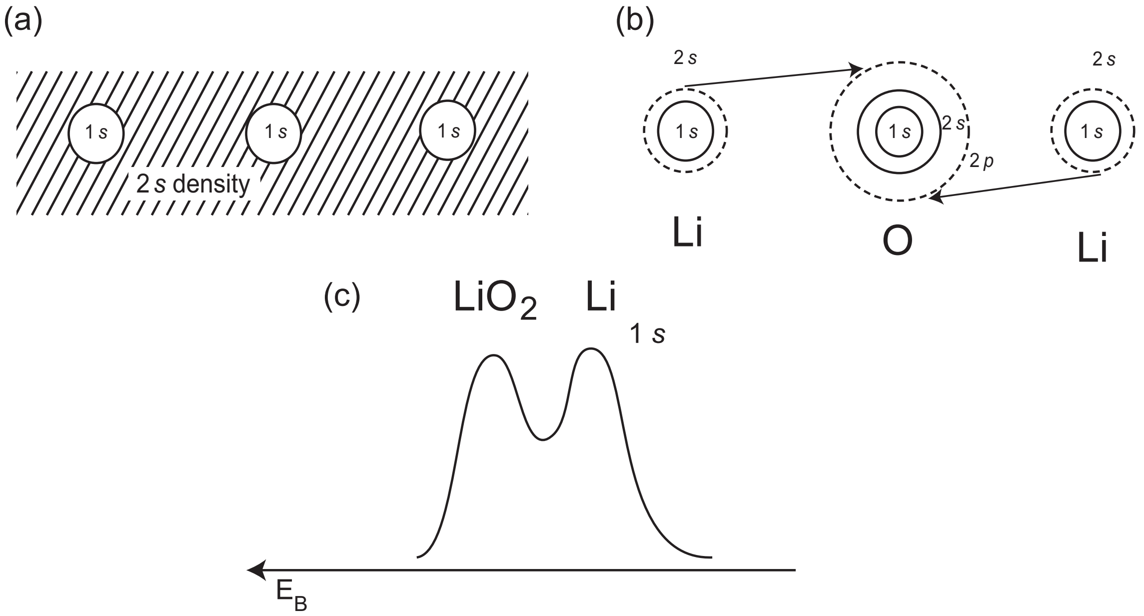

Figure 3.2: (a) and (b) describe schematically the valence electron distribution in lithium metal and lithium oxide. In lithium metal the 2 s electrons occur as a nearly constant background in contrast to lithium oxide where the 2 s valence electron is strongly localized close to the oxygen atom. In case of a sample which contains both lithium species a double structure occurs (deducted from [69]).

Parallel to the surface, the translation symmetry is preserved inside the solid with the lattice constant of the crystal and outside in the vacuum region by definition of a homogenous space. Therefore, the wave vectors, $\mathbf{k}_{\|}$, inside and outside of the solid are equivalent in contrast to the wave vector perpendicular to the surface. Further, the transmission through the surface affects the kinetic energy of the electrons. The surface-vacuum interface of a solid is a natural potential barrier typically in the range of 4.5 eV [92]. This barrier reduces the kinetic energy of the electron during the transition through the surface. The reduction of the kinetic energy is represented as Φ in *Equation* 3.1. Following from the momentum conservation of $\mathbf{k}_{\|}$ this energy reduction affects only $\mathbf{k}_{\perp}$ leading to refraction change of the propagation direction of the electron (see also *Figure* 3.3). This refraction is of particular importance in angle resolved photoemission spectroscopy and will be discussed later in *Section* 3.2.2.

3.2 Photoelectron Spectroscopy

3.2.1 X-Ray Photoelectron Spectroscopy

The XPS method is used to determine the binding energy of core level electrons. Considering an electron in a core level state, its binding energy is to a first approximation determined by the Coloumb potential generated by the atomic nucleons and

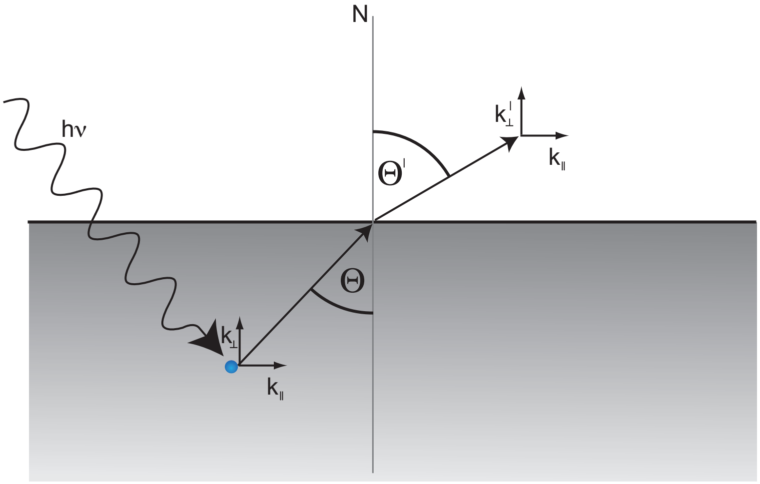

Figure 3.3: The excited electron travels to the surface with $k_\parallel$ and $k_\perp$ at an angle of Θ to the surface normal. After the transmission through the surface the electron leaves the solid at an angle Θ' and a wave vector k'. $k_\parallel$ is equal inside and outside of the solid.

the other core level electrons of the same atom. The exact binding energy is further influenced by the valence band electron density in the closed environments of the atom. Every valence band electron partly screens the core level electron from the core nucleons. Therefore, a redistribution of the valence electron density changes the binding energy of a core level electron resulting in a shift of the core level emission line in the XPS spectrum. Reductions of the valence electron density reduce the screening effect from the core potential, shifting the core level emission to a higher binding energy. An increased electron density shifts the emission line in the opposite direction. A simple example is the lithium $1\,s$ level in lithium metal and lithium oxide. A schematic picture of the electronic structure of these two compounds is given in *Figure* 3.2. In lithium metal the $2\,s$ electrons are delocalized over the whole solid with a finite probability density around the lattice sites of the Li atoms. These electrons screen the Li $1\,s$ level from the center nucleon potential. In case of lithium oxide, shown in *Figure* 3.2 (b), the Li $2\,s$ charge is basically localized around the strongly electronegative oxygen site in order to establish the preferred closed-shell $2\,p^6$ configuration. Because of the now strongly reduced valence electron density in the vicinity of the lithium core, their screening effect for the Li $1\,s$ electrons is lost, resulting in a higher binding energy. Simultaneously, the O $1\,s$ binding energy is reduced due to additional screening by the two added $2\,p$ electrons. *Figure* 3.2 (c) shows the schematic XPS spectrum of a sample containing lithium and lithium oxide; the occurrence of a double peak structure shows clearly that lithium exist in two different chemical environments.

3.2.2 Angle Resolved Photoelectron Spectroscopy

In order to investigate the electron band dispersion, $E(k)$, in solids the intensity of emitted electrons as a function of the kinetic energy, E_{kin}, and the emission angle, Θ', is measured in ARPES experiments. These experimental parameters, E_{kin} and Θ' define the $k'_\perp$ and $k'_\|$ of the electron after the escape from the solid (see also *Figure* 3.3). As already mentioned in the discussion of the three step model $k_\|$ is preserved during the transmission through the surface. Hence, the $k_\|$ in the vacuum and in the solid is given by equation 3.4

$$k = \sqrt{k_\|^2 + k_\perp^2} \tag{3.3}$$

$$k_\| = \frac{\sqrt{2m}}{\hbar}\sqrt{E_{\text{kin}}}\sin\Theta \tag{3.4}$$

$$k_\perp = \frac{\sqrt{2m}}{\hbar}\sqrt{E_{\text{kin}} + V_0 - \frac{\hbar^2}{2m}k_\|^2} \tag{3.5}$$

Unfortunately, $k_\perp$ is not preserved during the transition through the surface. The work function reduces the kinetic energy affecting only the $k_\perp$ component of the wave vector. As a consequence, the calculation of $k_\perp$ in equation 3.5 is only possible under the assumption of an inner potential.

Graphene, which is the object of the presented work, is a two dimensional material revealing a constant $k_\perp$ for valence band electrons [69]. In two-dimensional systems the influence of the k_z dispersion is restricted to a few meV shift of the bands as a function of photon energy [93]. Therefore, the discussion of the graphene band structure and intercalants is restricted to $k_\|$.

Based on the 2 dimensional nature of graphene the discussion of the wave vector can be restricted to the $\text{k}_\|$ component, which is preserved upon the transmission through the interface and can be calculated from the emission angle and the kinetic energy after the escape from the surface. Finally, the energy balance of the excitation process of the electron into the vacuum is described by the Einstein Equation 3.1.

3.2.3 Experimental Setup

As shown in the last section, in order to obtain the two-dimensional band structure it is necessary to measure the emission angle and the kinetic energy of the emitted electrons.

A technical approach to measure a range of emission angles is to rotate the sample with respect to the analyzer. There are two established sample rotation principles, which are distinguished only by different rotation axes as presented in *Figure* 3.4. In both cases the analysis of the horizontal emission angle, Θ, is realized by a 2 D imaging detector. The vertical component of the emission angle is determined by a scan of the rotation angles. In the left drawing of *Figure* 3.4 the sample rotates around the β axis and data are collected for every particular angle β. Therefore such sample motion is called "β-flip". In the right drawing of *Figure* 3.4 the sample

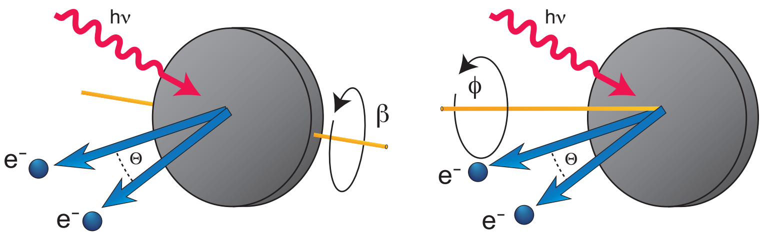

Figure 3.4: Two possible rotations modes which are used in ARPES experiments in order to measure a range of emission angles, i. e. rotation around the β and the ϕ angle, respectively.

rotates around the surface normal. Data are collected for every particular azimuthal angle ϑ. The resolution of the emission angle in a β-flip scan is defined by the resolution of the 2 D imaging detector, in the horizontal direction and by the step size of the rotation in the vertical direction. In case of a rotation around the surface normal, the detector resolution defines the polar angle resolution and the azimuthal angle resolution is defined by the step size. In comparison of sample motion the β flip is favorable because of constant angle resolution in contrast to the azimuthal angle scan where the resolution decreases with an increase of the emission angle. In this work two experimental stations with both motion types are used.

The first chamber is equipped with a 6-axis manipulator allowing the β rotation over a range of 70°, and a spherical energy analyzer (PHOIBOS 100) produced by SPECS GmbH (see also *Figure* 3.5). The second chamber uses the azimuthal rotation of the sample. The electron energy analyzer of this chamber is a self-built so-called toroidal analyzer. This device was developed and built by the groups of Prof. R. Leckey and Prof. J. Riley from La Trobe University, Australia [94]. Both chambers are similar in that point that they use curved electron trajectory to project the kinetic energy distribution onto a real space axis. That means electrons of different kinetic energies are detected at different positions.

The following overview over the measuring process focuses on the chamber which is equipped with the PHOIBOS analyzer. Electrons which were excited by photons escape from the sample in the direction of the analyzer. After the entry of the electrons into the analyzer, these electrons are focused by a stack of electrostatic lenses allowing to operate the analyzer in different operation modes (see *Table* 3.1 and [96]). These operation modes have different acceptance angle ranges and focusing. Subsequently, the electrons enter hemispheres of different electrical potentials. The inner sphere is at positive and the outer one at negative potential. The difference of the potential between the spheres together with the entrance and exit slits defines the kinetic energy range of electrons which can pass. This energy can be tuned by the potential difference between both half spheres. The kinetic energy of the electrons, which pass the analyzer from the center of the entrance slit to the center of the exit slit, is called pass energy. This pass energy can be used to set the resolution and the size of the observed energy window. After the escape from the sphere the number of electrons is multiplied by a multichannel plate in oder to

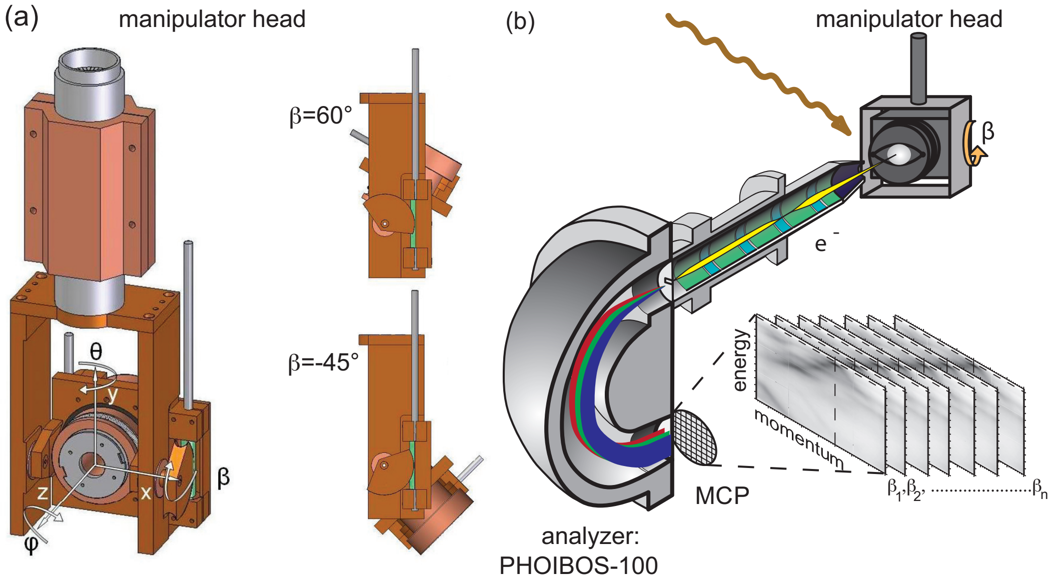

Figure 3.5: (a) shows the construction of the manipulator head. In order to avoid destructions of the manipulator head the β rotation was restricted to the angle range of -45° $\leq \beta \leq$ 30° (deducted from [95]). (b) Principle arrangement of the manipulator head with the spherical energy analyzer. The electrons enter the analyser as a focused beam at the entrance slit. After pass of the sphere the electrons are spreaded in vertical direction depending on the kinetic energy.

increase the signal, and they are accelerated and hit a fluorescent screen. The screen images are recorded by a CCD camera. The vertical and the horizontal axis of the screen image is the energy dispersive and angle Θ axis, respectively (see als *Figure* 3.5 b). The brightness, $I(E_{kin}, \Theta)$, of a specific pixel in the screen image reflects the number of electrons which were emitted at a kinetic energy and the angle Θ. Therefore, the screen image provides information only of a particular slice of the valence bands because only the horizontal component of the emission angle is measured. The adoption of the measuring process in the case of the Toroid chamber can be given briefly. A detailed description of the toroidal analyzer is given in reference [94]. The advantage of this construction is the huge horizontal angle acceptance of 140° in contrast to the PHOIBOS analyzer (see also *Table* 3.1)

The sample motion works as surrounding process step of the measuring process of a single image, which is described in the paragraph above. In case of the PHOIBOS chamber the sample holder is moved to a particular angle β_1, and data is collected for a defined time before going to the next angle β_2. In case of a large β range such a scan can run over several hours. All images, stacked together, create a 3-dimensional data set $I(E_{kin}, \Theta, \beta)$. Noteworthy is that in contrast to the β angle which is known from the physical angle of the sample holder orientation with respect to the analyzer direction during the measurements, E_{kin} and Θ are stored as the numbers of the row and column of the pixel of the CCD camera. The row assignment to E_{kin} is implemented through a routine in the measuring software. In order to assign

Lens mode	Acceptance angle	Typical Application
High Magnification II	± 9 °	XPS, alignment
Low Angular Dispersion (LAD)	± 3 °	ARPES with high resulution
Wide Angle Mode (WAM)	± 13 °	ARPES over a wide angle range

Table 3.1: This table presents the in this work of the PHOIBOS analyzer lens modes used.

the particular columns to a certain angle Θ, symmetry aspects of the k-space are used. Equal features of the band structure have to occur at equal emission angles in β and Θ. A better understanding of the symmetry conditions is gained from constant energy cuts shown in *Figure* 3.6. The elliptic structures, denoted by green dashed ellipses in *Figure* 3.6, have to occur at the same emission angles for β and Θ. Therefore, the known β angle can be used to assign emission angles to certain columns in a data treatment procedure explained in the next section.

The presented ARPES data were measured at the "Berliner Elektronenspeicherring-Gesellschaft für Synchrotronstrahlung" (BESSY) facility at different beamlines: TGM 4, UE 56/PGM 1 and 2. The data presented in *Figure* 7.2 (a) and (d) were measured with the toroidal chamber. All other data were collected with the PHOIBOS chamber.

3.2.4 Data Evaluation of Angle Resolved Photoelectron Spectroscopy Measurements

The measured data set is a 3-dimensional matrix $I(E_{\mathrm{kin}}, column, \beta)$. In order to transfer this data into k-space using *Equation* 3.4, it is necessary to assign every column to a certain emission angle Θ.

The symmetry of the crystal leads to equal valence band features in equal symmetry directions at equal emission angles. This condition is used to assign every column to an emission angle. For example, in case of a four fold symmetric crystal surface aligned with a high symmetry axis parallel to the β movement, the column which exhibits the same band feature like a certain β angle can be assigned to the equal emission angle. This condition is valid for every direction in k-space including

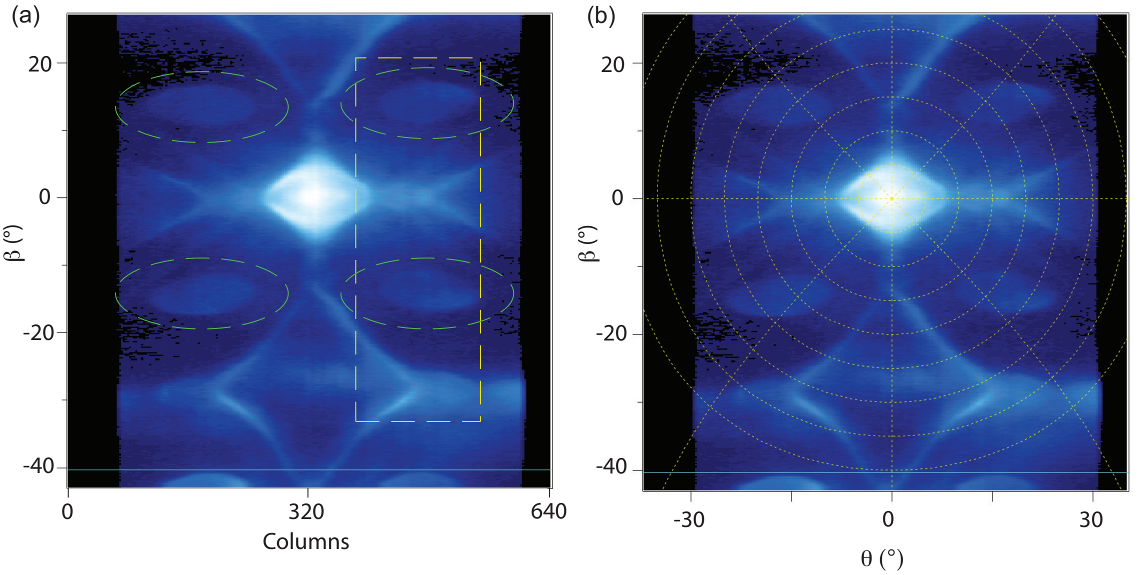

Figure 3.6: Data treatment of O/W(110) results used constant energy cuts at 300 meV: The ordinate labels the physically angle β at which the image was taken. Clearly visible in (a) are the symmetrical structures marked with green ellipse which can be used to assign the columns to the unknown angle θ. The yellow dashed rectangle denotes the measured emission angle range of a typical LAD scan. (b) A Polar grid is useful to determine the pixel_Θ/angle relation.

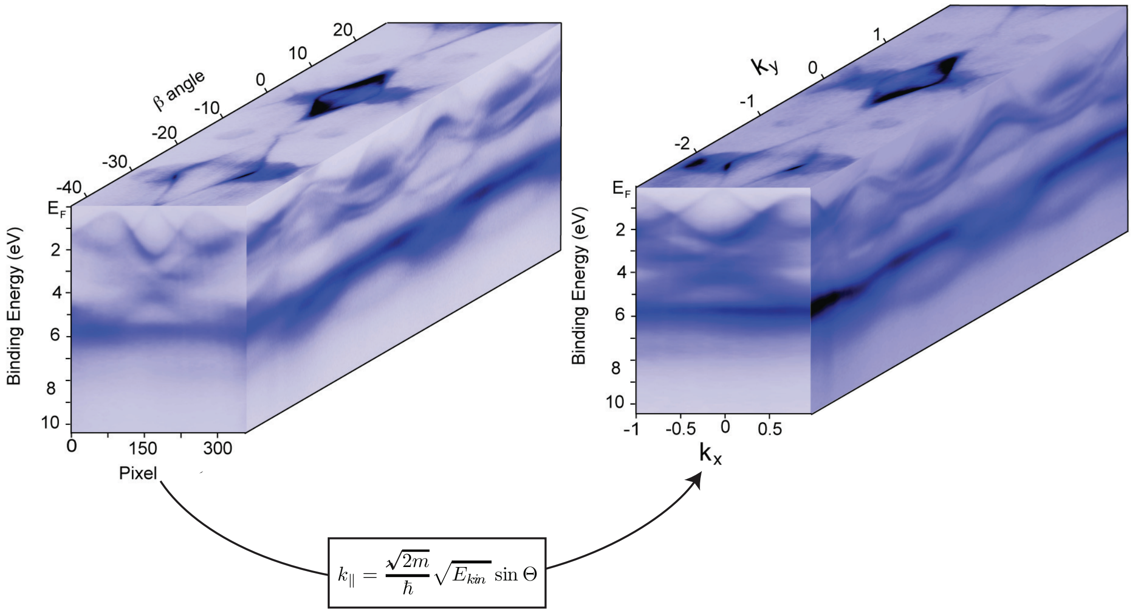

Figure 3.7: This figure summarizes the transformation of ARPES raw data set of O/W(110) taken at 100 eV photon energy into the k-space.

non-high symmetry directions. A useful procedure is to project a polar angle grid on top of a constant energy cut of the dataset as shown in *Figure* 3.6. All equal structures have to occur on a circle of the polar angle grid indicating the equal emission angles independent if direction is a high symmetry one or not.

Further difficulties can arise in measurements in the LAD mode. The strongly restricted emission angle acceptance handicap or even avoid the possibility to use the symmetry conditions. The angle range of a possible LAD is marked in *Figure* 3.6 as a yellow dash rectangle. The small size lead to the loss of several equal band structure features. It becomes more difficult if the scan does not include the Γ point. A way out is to used a treated WAM dataset in $I(E_{\mathrm{kin}}, \Theta, \beta)$ configuration as reference. The change of the lens mode does not influence the emission angle of the electron, therefore it is possible to assign the columns of the LAD scan to the Θ angles of the WAM dataset.

After this assignment of the columns to emission angles the dataset exists as a 3-dimensional matrix $I(E_{\mathrm{kin}}, \Theta, \beta)$ and *Equation* 3.4 is used to transfer the dataset into k-space. This transformation creates a new dataset $I(E_{\mathrm{kin},k_x,k_y})$ The transformation of a complete dataset after the measurements into the k-space is summarized in *Figure* 3.7.

3.3 X-ray Absorption Spectroscopy and X-Ray Magnetic Circular Dichroism

3.3.1 Linear Polarized Light and Solids

If linear polarized light is used in absorption experiments it is possible to derive an angle dependence of the absorption strength from the angle between the electric field vector of the incoming photon and the orbital orientations of the empty states. Near-edge x-ray absorption fine structure spectroscopy uses this fact to investigate the orbital orientations [71, 97].

The electrical field vector $\mathbf{E}$ of linearly polarized light can be described as a vector field $\mathbf{A}$

$$\mathbf{E} = -\frac{1}{c}\frac{\partial \mathbf{A}}{\partial t} \tag{3.6}$$

$$\mathbf{A} = \mathbf{e}A_0 e^{i(kr-\omega t)}. \tag{3.7}$$

Here it is assumed that the light propagates as a plane wave. *Equations* 3.6 and 3.7 show that the vectors $\mathbf{E}$ and A are collinear. The outcome of inserting the vector field $\mathbf{A}$ into Fermi's golden rule, *Equation* 3.2, yielding the transition probability $P_{\mathrm{i,j}}$, is

$$P_{\mathrm{i,j}} = \frac{2\pi}{\hbar}\frac{e^2}{4m^2}\left|\langle j\left|\hat{\mathbf{p}}\mathbf{e}A_0 e^{i(kr-\omega t)} + \mathbf{e}A_0 e^{i(kr-\omega t)}\hat{\mathbf{p}}\right| i\rangle\right|^2 \rho_{\mathrm{j}}(E)\delta_{\mathrm{E}}\delta_{\mathbf{k}}\delta_{\mathrm{J}}. \tag{3.8}$$

Now, the well-known dipole approximation $\mathbf{kr} \ll 1$ can be used to simplify this equation [71, 98]. This approximation, assuming a nearly constant electrical field strength over the whole initial state, is valid if the wavelength is significant larger than the real space dimension of the initial state $\mid i\rangle$. In case of x-rays this condition is well fulfilled.

$$\mathbf{A} = \mathbf{e}A_0 e^{i(kr-\omega t)} \overset{\mathbf{kr}\ll 1}{\approx} \mathbf{e}A_0 e^{-i\omega t}. \tag{3.9}$$

Inserting the approximated vector field into *Equation* 3.8 yields

$$P_{\mathrm{i,j}} = \frac{2\pi}{\hbar}\frac{e^2}{m^2}A_0^2 \left|\langle j\left|\mathbf{e}\hat{\mathbf{p}}\right| i\rangle\right|^2 \rho_{\mathrm{j}}(E)\delta_{\mathrm{E}}\delta_{\mathbf{k}}\delta_{\mathrm{J}}. \tag{3.10}$$

The product of the unit vector $\mathbf{e}$ with the momentum operator $\hat{\mathbf{p}}$ selects the component of momentum parallel to $\mathbf{A}$. Finally, the collinearity between the vectors $\mathbf{A}$ and $\mathbf{E}$ leads to the selection of states having a momentum in-plane with the polarization of the light.

If the initial states have an orbital momentum different from zero the shape of the core level orbitals can induces a further angle dependence of the absorption strength leading to additional signatures in the absorption signal. In order to avoid such initial state effects the use of an *s* core level absorption edge is recommended in NEXAFS experiments, which have the goal to yield information about final state symmetry.

A better understanding of the physical meaning of the dipole matrix element can be obtained using the real space equivalent of the momentum operator [99, 100]

$$\langle j\left|\mathbf{e}\hat{\mathbf{p}}\right| i\rangle = \mathrm{im}\left(\frac{E_{\mathrm{j}} - E_{\mathrm{i}}}{h}\right)\langle j\left|\mathbf{e}\hat{\mathbf{r}}\right| i\rangle. \tag{3.11}$$

This identity shows that the angle dependence of the absorption strength on distribution of the probability of finding is valid as well as for the distribution of the momentum.

Equations 3.10 and 3.11 include the experimental parameter A_0 which is linearly connected to the amplitude E_0 of electrical field vector which is created by the sum of all incoming photons. In order to obtain a pure sample dependent relation, the absorption cross section σ, it is necessary to eliminate the photon intensity dependence of $P_{\mathrm{j,i}}$ via division of *Equation* 3.10 by the photon flux Φ

$$\sigma_{\mathrm{i,j}} = \frac{P_{\mathrm{i,j}}}{\Phi}. \tag{3.12}$$

The photon flux Φ can be written as time-average of the pointing vector $\overline{S}$ divided by the energy of a single photon.

$$\Phi = \frac{\overline{S}}{\hbar\omega} = \frac{\epsilon_0 c E_0^2}{2\hbar\omega} = \frac{\epsilon_0 c A_0^2 \omega^2}{2\hbar\omega}. \tag{3.13}$$

After the elimination of the photon intensity dependence only the known experimental parameters, incident angle of the light and photon energy are contained in the *Identity* 3.14.

$$\sigma_{\mathrm{i,j}} = \left(\frac{4\pi\hbar}{m}\right)^2 \frac{\alpha}{\hbar\omega}\left|\langle j\left|\mathbf{e}\hat{\mathbf{p}}\right| i\rangle\right|^2 \rho_{\mathrm{j}}(E)\delta_{\mathrm{E}}\delta_{\mathbf{k}}\delta_{\mathrm{J}}. \tag{3.14}$$

The total absorption strength of the sample at a certain photon energy is measured, therefore the cross section of all possible excitations has to be add to the total cross section including states at lower binding energies. However, usually the cross section of a certain core level at photon energies close to the resonance region are dominant compared to the cross section of core level states far away at smaller binding energies

$$\sigma = \sum_{i,j} \sigma_{i,j}. \tag{3.15}$$

Two facts render the absorption measurements element specific. First, the matrix element of a particular transition and with its transition probability vanishes for transitions starting and ending in states of different elements. Second, the absorption edges usually occur at different photon energies avoiding the superposition of the absorption signals. Both facts together ensure an element specific investigation of the absorption strength.

In summary, the angle dependence of absorption strength from the incident angle is used to investigate the orientation of orbitals of empty states. This method is limited to ordered systems because if states exist in arbitrary orientations, the NEXAFS absorption strength will be isotropic.

For ordered systems, however, absorption experiments with linearly polarized light is a powerful method to investigate the orientation of molecule orbitals and to control the degree of order.

3.3.2 Circular Polarized Light and Solids

In order to investigate the magnetic moment of a sample, XMCD experiments use the dependence of the absorption strength on the strength of the magnetic moment and the dependence on the angle between the photon spin and magnetic moment [101–105]. The photon spin $\langle S_{h\nu} \rangle = \pm 1$ carried by circularly polarized photons connects the magnetic properties of the sample with absorption strength.

First, it has to be emphasized that the handedness of circular polarized light is not consistently defined [106]. In this work the Feynman convention is used [107]. It allocates the right polarized light via positive photon helicity to "spin-up" and left circular light to "spin-down".

In typical XMCD experiments two absorption spectra are taken measured with opposite photon helicities or inverted magnetizations of the sample (see also *Figure* 3.10). The information about the magnetic moments is contained in the differences of the absorption strength between both spectra, the so-called XMCD contrast.

For a description of the XMCD method it is necessary to distinguish between non spin-orbit split s core levels and spin-orbit split core levels such as p, d, and f. Here the description is given for the $p_{3/2}$ and $p_{1/2}$ levels followed by a comparison with the non split s level.

A completely filled p core level exhibits no net orbital moment. The orbital moments compensate in pairs. After the excitation of one electron, this electron leaves the atom and couples to the remaining uncompensated orbital moment. This

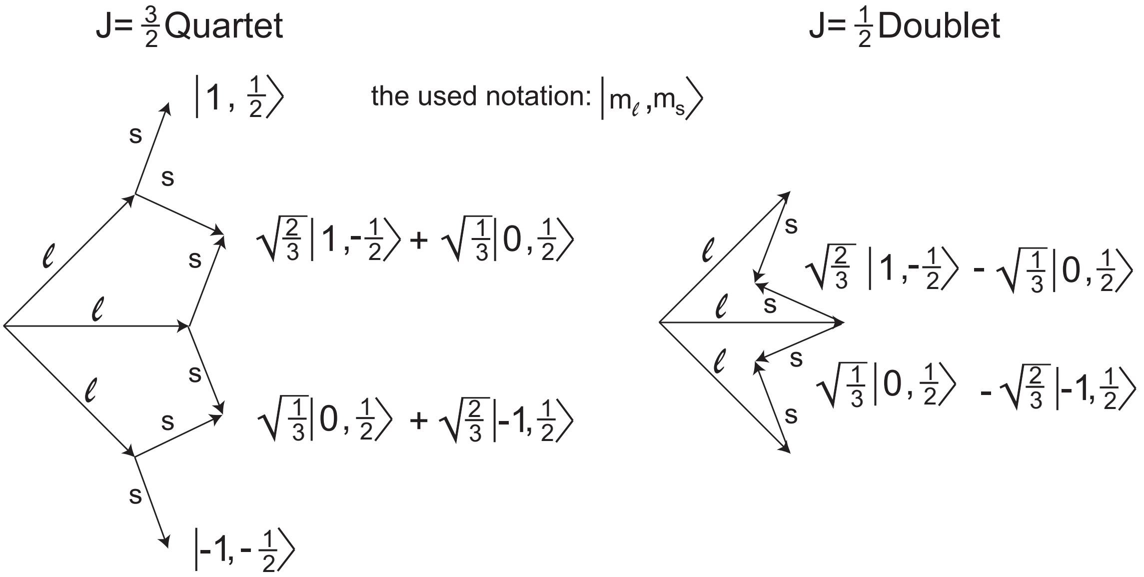

Figure 3.8: Possible final state configurations of p core level absorption

coupling creates a final state split into the $p_{3/2}$ and $p_{1/2}$ final state energy levels in absorption spectra. Both energy levels occur at different photon energies. The possible configurations of the total angular momentum $J = |l \pm s|$ are shown in *Figure* 3.8.

The J scheme of *Figure* 3.8 makes clear that all single configurations of m_l and all single configurations m_s exist equally in every absorption level. Thus a spin or orbital polarization of the excited electrons does not originate from the possible configurations of the final states. However, the number of configurations is twice as large for $J = \frac{3}{2}$ as for $J = \frac{1}{2}$. This has to be taken into account for a quantitative analysis of the dichroism contrast.

p electrons can be excited into empty s or d valence band states. The magnetic properties of the transition metals are determined mainly by d electrons. For the ferromagnets Fe, Co, and Ni the combined $4\,s$ and $4\,p$ contribution to the magnetic spin moment is less than $5\,\%$, and the orbital magnetic moment is entirely due to $3\,d$ electrons [108–110]. Therefore, the s and p valence band magnetism can be neglected. Further, as shown in *Figure* 3.9 (a) in the Stoner model [103, 111], which is a strongly simplified model, the DOS of the s and p states is extended over a large energy range compared to the DOS of the d states. Hence these DOS can be assumed to be constant and occur as a step function-like signal in the absorption spectra. Thus the whole XMCD contrast is assigned to $3\,d$ valence band magnetism.

The selection rule $\Delta s = 0$ defines that the photon spin couples only to the orbital momentum ensuring an unaffected spin state of the excited electron. Absorption of circular light changes $m_l = \pm 1$ for right and left circular polarization creating an orbital polarization of the excitation current [103, 112, 113]. Noteworthy is that the orbital polarization of the excitation current is equal for both absorption edges.

Figure 3.9 (a) shows a Stoner model of a hypothetical sample which has only an orbital moment [102, 103, 111]. States which have an orbital moment aligned parallel to the magnetization are shifted energetically downwards in contrast to electrons which have orbital moment aligned antiparallel to magnetization. The equilibrium of the Fermi level in both kinds of valence band states leads to an electron transfer generating different number of holes for differently oriented orbital polarized valence bands. The absorption strength is linearly connected to the numbers of holes which is described as $\rho(E)$ in Fermi's golden rule (see *Equation* 3.2). Samples which have no orbital polarization of the valence band have the same number of empty states for all orbital moments. Therefore the absorption strength for photons of both polarizations are equal and no dichroism contrast can be observed. In case of magnetic systems exhibiting an orbital polarization of the valence band the absorption strength is increased for the helicity which excites electrons into the minority states. As a consequence of the equal orbital polarization of the excited electrons from both absorption levels the resulting XMCD contrast has the same sign for both levels and is shown for this hypothetical system in *Figure* 3.9 (c). Considering the different number of states for $J = \frac{3}{2}$ and $J = \frac{1}{2}$ final state the absorption signals have ratio of 2. This process gives the opportunity to investigate the orbital moment of the valence band structure.

As well as for the investigation of the orbital magnetic moment an orbital polarized excitation current is necessary, a spin polarized excitation current is needed to study of spin polarization of the valence band. This spin polarized excitation current cannot occur from the photon spin electron spin interaction, such a coupling is strictly forbidden by the selection $\Delta s = 0$. In fact for a certain helicity the excitation probability of electrons in a spin-up or spin-down configuration is linked to the spin-orbit coupling $|l + s|$ and $|l - s|$ leading to opposite spin polarization for both levels. Fano calculated an opposite phase shift in the final state wave function for spin-up and spin-down as a function of the sign of the coupling. This phase shift creates a different overlap of the initial state with the final state affecting the absorption probability [103, 114, 115]. Therefore, the phase shift connects the photon helicity, the sign of the coupling and the spin state to the absorption strength. This phase shift is inverted between the $J = \frac{3}{2}$ and $J = \frac{1}{2}$ leading to the opposite spin polarization for the $J = \frac{3}{2}$ and $J = \frac{1}{2}$ level. The dichroism contrast of a hypothetical pure spin polarized valence band is shown in *Figure* 3.9 (b). Because of the opposite spin polarization between $|l + s|$ and $|l - s|$ level the dichroism contrast shows a ratio of -2 for both absorption energy levels. In summary, the photon spin influences via spin-orbit coupling the excitation probability, but not the spin state of the core level electron itself.

In real systems, spin and orbit polarization occur simultaneously leading to a superposition of both effects [103]. The resulting dichroism contrast is shown in *Figure* 3.9 (c). The loss of the 1:2 or 1:-2 ratio between both levels opens the door to calculations of both magnetic moments.

In the case of an s core level, there exists no orbital moment. The photon transfers the spin moment to the orbital momentum of the electron. This creates an orbital polarized excitation current which can be used to investigate the orbital

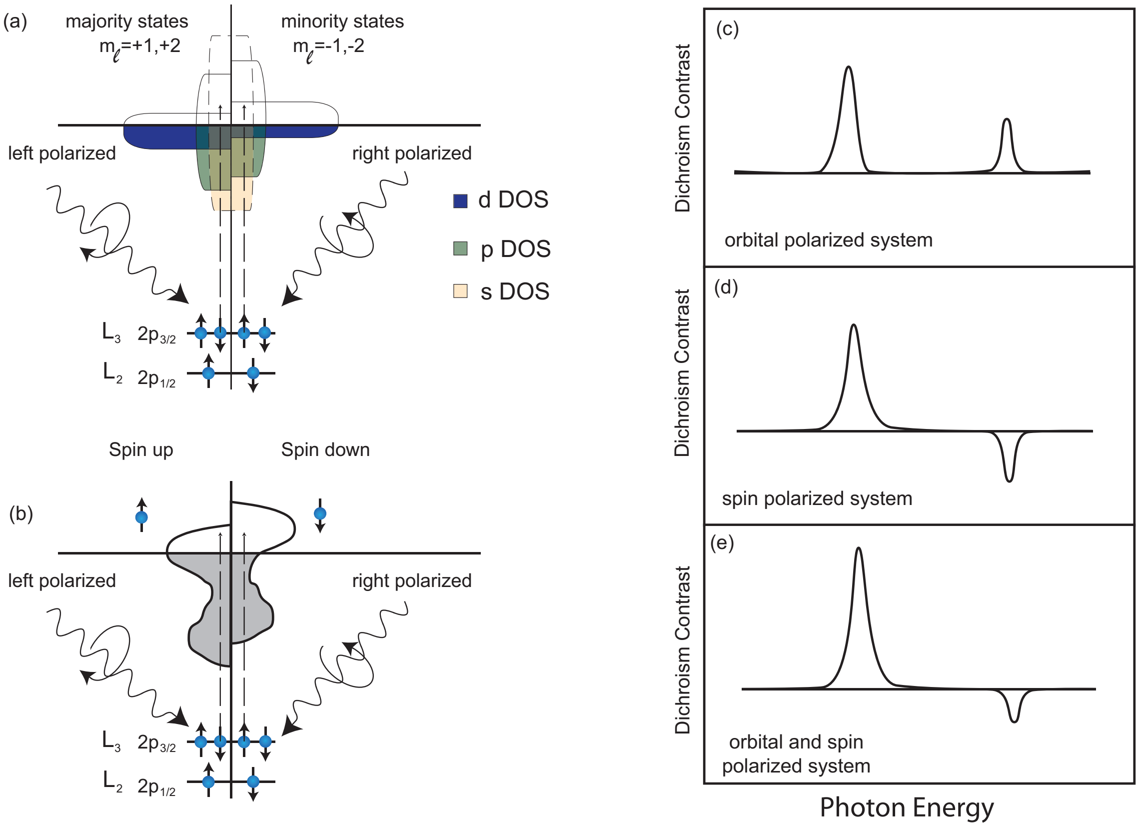

Figure 3.9: (a) shows the principe of an electron excitation by circular polarized light from the 2p core level into an orbital-polarized valence band. The similar process is shown for a spin-polarized valence band in (b). The resulting XMCD contrast for three hypothetical systems (c) only orbital-polarized valence band, (d) only spin-polarized and (e) a spin- and orbital-polarized, is drawn on the right hand side. (graphs (c), (d) and (e) are deducted from [103])

polarization of the valence band. In contrast, there exist no spin-orbit coupling, which can connect the helicity with the spin state depended absorption probability. As a consequence, the excitation current is completely spin unpolarized.

So far, the absorption strength was discussed only in terms of the number of holes in the valence band. However, the absorption also depends on the incident angle of the photon. The reason is that the photon spin defines a quantization axis of the excitation current. The magnetization direction of the sample defines the quantization axis of the valence band. The excitation current is only spin and orbital polarized with respect to the photon spin i.e., along the incident direction. During the excitation, the polarization of the electrons is projected onto the quantization axis of the sample, which is equal to the magnetization direction. For a maximal XMCD effect, both axes have to be aligned parallel, otherwise the orbital and spin polarization of the excitation current is projected partly onto the other Cartesian axes until no XMCD effect can be observed. This is the case if both axes are perpendicular with respect to each other. In the case of in-plane magnetization, the parallel alignment cannot be fulfilled therefore experimentalists use nearly grazing incident angle between 10° and 20°.

The theoretical description of the absorption process was developed by Thole [81] and Carra [82], who formulated to the so-called sum rules which connect the absorption probability for different photon helicities with the spin and orbital momentum of the sample:

$$\frac{\int_{j^+ + j^-} dE(\mu^+ - \mu^-)}{\int_{j^+ + j^-} dE(\mu^+ + \mu^- + \mu^0)} = \frac{1}{2}\frac{l(l+1) + 2 - c(c+1)}{l(l+1)n_h}\langle L_z\rangle, \tag{3.16}$$

$$\begin{aligned} &\frac{\int_{j^+} dE(\mu^+ - \mu^-) - [(c+1)/c]\int_{j^-} dE(\mu^+ - \mu^-)}{\int_{j^+ + j^-} dE(\mu^+ + \mu^- + \mu^0)} \\ = \; & \frac{1}{2}\frac{l(l+1) + 2 - c(c+1)}{3cn_h}\langle S_z\rangle \\ + \; & \frac{l(l+1)[l(l+1) + 2c(c+1) + 4] + 3(c-1)^2(c+2)^2}{6lc(l+1)n_h}\langle T_z\rangle. \end{aligned} \tag{3.17}$$

l and c are the quantum numbers of the orbital momentum of the initial state and final state, respectively. n_h denotes the number of holes in the valence band. The spectrum of the positive magnetized sample is μ^+ and for the negative magnetization μ^-. The function μ^0 is the so-called white light spectrum and is defined as $\mu^0 = (\mu^- + \mu^-)/2$. The integral intervals are assigned to energy ranges of j^+ for $|l+s|$ and j^- for $|l-s|$ marked in *Figure* 3.10 (a) for the Ni $L_{2,3}$ absorption edge. The three terms $\langle L_z\rangle$, $\langle S_z\rangle$ and $\langle T_z\rangle$ are the expectation values of the orbital moment, the spin moment and the intra-atomic dipole operator, respectively. This description was developed in an atomic framework. The use of an atomic model even for solids is justified by the strong localization of the core levels and was tested in a lot of experiments. These *Equations* 3.16 and 3.17 allow to calculate the orbital and spin moment of sample.

As an example, the Ni $L_{2,3}$ absorption spectra of the Ni(111) for in-plane magnetization are shown in *Figure* 3.10. In this experiment and for all XMCD measurements shown in the presented work, the helicity of the photons was fixed and the sample magnetization was changed. This is a often used measuring principle. The sum rules for the $L_{2,3}$ absorption into the $3\,d$ valence band are:

$$\langle L_z\rangle = \frac{2}{3}\frac{n_h}{P\cos\gamma}\frac{\Delta A_3 + \Delta A_2}{A_3 + A_2} \tag{3.18}$$

$$\tag{3.19}$$

$$\langle S_z\rangle = \frac{1}{2}\frac{n_h}{P\cos\gamma}\frac{\Delta A_3 - 2\Delta A_2}{A_3 + A_2} - \frac{7}{2}\langle T_z\rangle. \tag{3.20}$$

In order to write the equations more clearly the integrals of general sum rules are already solved. ΔA_3 and ΔA_2 represent the integrals of the XMCD contrast which is defined as the difference in the absorption intensity between both magnetization

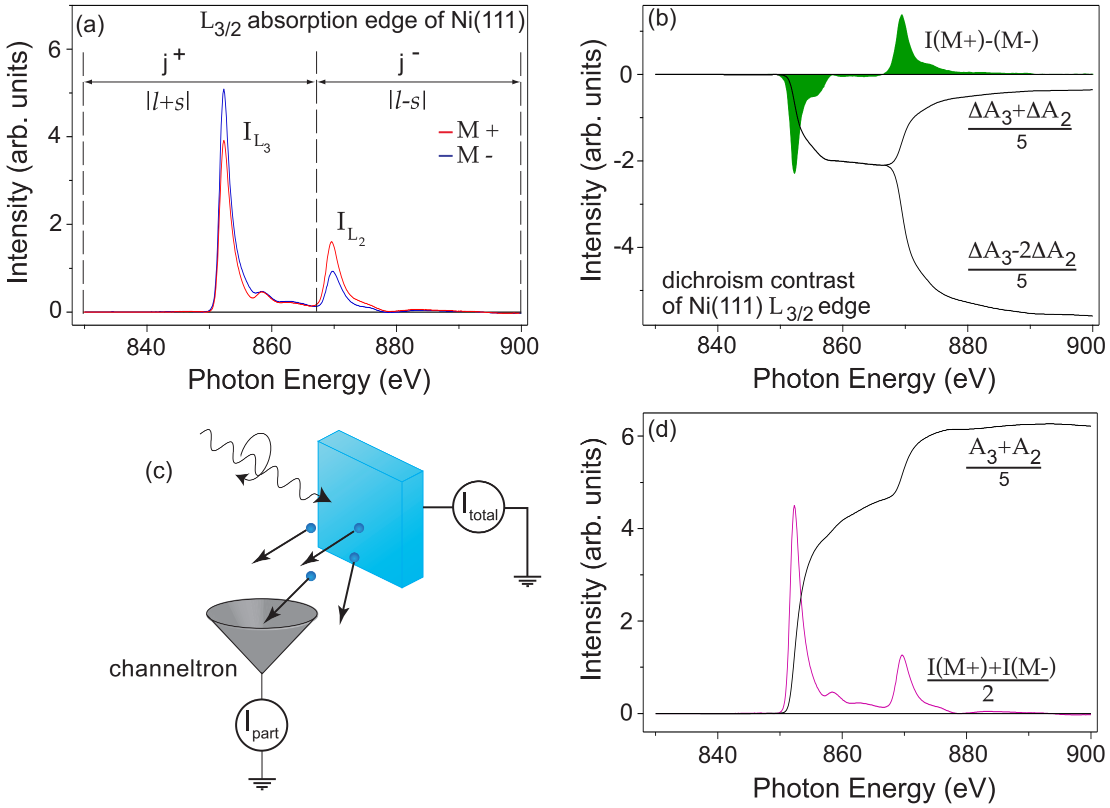

Figure 3.10: (a) shows the typically XMCD absorption spectra of the Ni $L_{2,3}$ edge for both photon helicities or both magnetizations. The integral intervals, which are used in the sum rules are labeled as j^+ and j^-. The XMCD contrast and the solutions of the integrals are shown in (b) and (d). (c) shows a principle XMCD experimental setup.

or both helicities $I(M^+) - I(M-)$ (see also *Figure* 3.10 and *Equations* 3.19 and 3.20). The indices 2 and 3 mark the spin-orbit split absorption levels, respectively. The integral of the white light intensity over both absorption regions are noted as $A_3 + A_2$. Stöhr und König pointed out that for the case of $3\,d$ transition metals the intra-atomic dipole operator $\hat{T} = \hat{S} - 3\hat{r}(\hat{r} \cdot \hat{S})$ can be neglected [106, 108]. In *Equations* 3.19 and 3.20 two new experimental parameters are included. In many cases, X-ray sources do not deliver 100 % polarized light. Hence P includes the degree of circular polarization of the light. The projection of the spin polarization of the excited electrons onto the magnetization axis is noted by the term $\cos\gamma$ with γ being the angle between both quantization axis.

In case of the C $1\,s$ absorption edge, which was used to investigate the induced magnetic moments of the graphene layer, the sum-rules are reduced to:

$$\langle L_z \rangle = \frac{n_h}{P\cos\gamma}\frac{\Delta A}{A}. \tag{3.21}$$

An investigation of the spin moment with the sum rules is not possible because $l = 0$.

This becomes obvious by the occurrence of $l = 0$ at denominator of the second term on the right side in *Equation* 3.17.

Furthermore, from the selection rules it follows that the transitions from $p \rightarrow d$ and $p \rightarrow s$ are contained in the XMCD spectra. However, the $p \rightarrow d$ channel is the dominating channel by a factor of more than 20 [116]. Hence the $p \rightarrow s$ channel can be neglected. This grants experimental access to the occupation of the *d*-states.

3.3.3 Experimental Setup

What is not described yet is how the absorption strength can be measured, if the final states exist in vicinity to the Fermi level, the excited electrons can not overwhelming the work function. The absorption creates a core hole. The recombination of the core hole occurs partly through the Auger and fluorescence processes [71]. In the presente work the fluorescence yield of the absorption process was not investigated hence it is not discussed here. In Auger processes the core hole is recombined by an electron at low binding energy transferring the energy gain to an electron which can leave the sample. If the kinetic energy is large enough these electrons can leave the sample.

All NEXAS experiments were performed at the MAX-LAB Synchrotron Radiation facility at the dipole beamline D1011.

The PEY mode used channeltron uses a retardation potential in order to remove slow electrons from the absorption signal. These slow electrons included in scattering processes originate from deeper ranges of the sample. Therefore the PEY is more surface sensitive compared to the TEY which counts all electrons which leave the sample.

The PEY detection mode cannot be used in a permanent outer magnetic field. The Lorenz force influences the electron trajectory which affects the measured absorption signal. Therefore the samples were measured in remanence. The remanent magnetic field of a $\approx$200 Å thick ferromagnetic layer is very weak and can be neglected.

Some general comments: the helicity of the beamline should be fixed in order to avoid artificial signals. These signals can occur if the photon flux or the degree of the spin polarization for both helicities is not perfectly equal. The measurement of the C *K* edge is always very difficult due to the C impurities in beamline mirrors. These C impurities on the mirror surface are created via segregate of C atoms contained in the bulk of the mirror or decomposition of hydrocarbons during beamline operation. Therefore the beamline creates its own C *K* edge absorption signal. The use of reference sample or a Au grid at the end of the beamline, which records the photon flux after the beamline, is useful.

3.3.4 Data Evaluation in Absorption Measurements

The absorption spectrum of the Ni $L_{2,3}$ edge shown in *Figure* 3.11 (a) serves as an example for the stepwise data treatment; the aim is to obtain the XMCD contrast

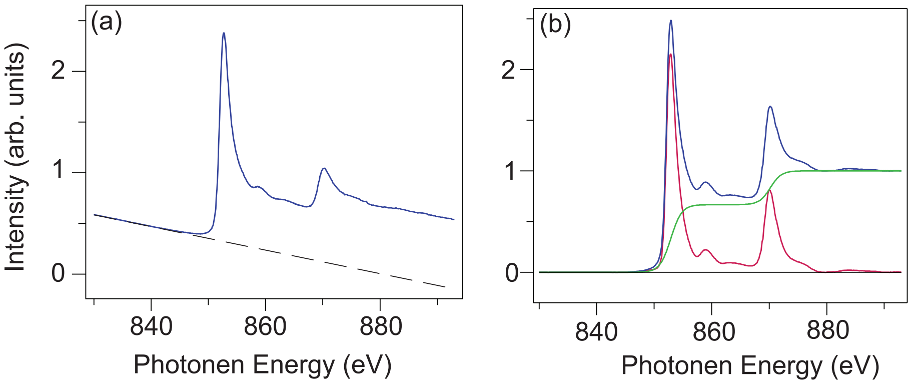

Figure 3.11: A typical raw XAS spectra is shown in (a). This spectra exhibits a strong decreasing linear back round, which has to be removed. In (a) the linear fit is drawn as black dashed line. (b) shows the stepwise data treatment. The treatment starts with normalization of the post-edge signal to one shown by alignment of a two stepped step-function and ends with the subtraction of the step-function from the spectra.

spectra as shown in 3.10 (a).

An absorption spectrum of one particular absorption edge often contains a linearly decreasing background: A fit of this background is illustrated in *Figure* 3.11 (a) as a black dashed line. This background belongs to absorption edges at lower binding energies and is not related to the chosen absorption edge and has to be removed from the spectra. This can be done by a linear fit to the pre-edge region as illustrated in *Figure* 3.11 (a). Therefore, it is recommend to extend this part of the spectra in order to improve the quality of the linear background fit. The data treatment proceeds with the normalization of the spectra to the post-edge region. This range should be extended as well as the pre-edge region. In this region typically oscillations of the absorption intensity occur and are used in EXAFS experiments, another type of absorption experiments [117, 118]. These oscillations originate from scattering effects of the excited electrons with the neighboring atoms. The spectrum after normalization is drawn as a blue curve in *Figure* 3.11 (c). It exhibits a double step structure which arises from electron excitations into the unoccupied s and p continuum states [103]. The sum rules are valid only for a particular transition such as $2\,p \rightarrow 3\,d$. Therefore these continuum transition signals have to be removed from the spectrum. This removal of the continuum transitions is possible because of the very small contribution of these valence band states to the magnetism. The equation of the step function is given by

$$\mu_{step} = \left(1 - \frac{2}{3}\frac{1}{1+e^{\frac{E-E_{L_3}}{\delta}}} - \frac{1}{3}\frac{1}{1+e^{\frac{E-E_{L_2}}{\delta}}}\right) \tag{3.22}$$

and is drawn as a green curve in *Figure* 3.22. In this equation E_{L_2} and E_{L_3} represent the peak positions of the absorption edges. δ reflects the broadening of the edge, which arises from the temperature broadening and the limited life time of the excited state. This parameter is uncertain and has to be fitted to the rise of the curve at the front side of the absorption resonance. The pre-factors $\frac{2}{3}$ and $\frac{1}{3}$ take into account the different occupations of the $p_{3/2}$ and $p_{1/2}$ levels. The total heights of the step function, μ_{step}, has to be aligned to the center of the intensity oscillation in the post-edge region because of scattering effects which are not related to the spin and orbital moment. After the subtraction of this step function the data appears in the shape of the red curve in *Figure* 3.11 (c). This is the structure of spectra to which the sum rules are applied.

Chapter 4

Sample Preparation

This chapter starts with description of the preparation of an atomic clean Ni(111) surface; then the method used to grow a single and multilayer layer graphene is explained and closes with the method to intercalate Fe and Al underneath graphene on Ni(111).

In order to avoid contamination, all samples were prepared in situ. All experimental stations were equipped with an additional preparation chamber. The base pressure for every measuring and preparation chambers did not exceed $8{\cdot}10^{-10}$ mbar even for the entire metal deposition procedure.

4.1 Graphene on Ni(111)

4.1.1 Preparation of the Ni(111) Surface

Two different methods were used to prepare an atomically clean Ni surface: first, epitaxial growth of a thick Ni layer on top of a W(110) crystal, and second a macroscopic Ni(111) cleaned by sputtering and annealing. Both methods have been known for a long time.

Cleaning Procedure of W(110)

The first method of Ni(111) growth on a W crystal as a template to grow Ni in (111) surface structure uses the fact that Ni, for coverages higher than two monolayers, grow with (111) surface orientation [119–122]. This preparation starts with cleaning cycles of the W(110) crystal. In the first step the W(110) crystal is annealed for 1 h up to 1300° C, such that impurities contained in crystal segregate to the surface. Subsequently, the crystal is exposed for 1 h at the same temperature to an oxygen atmosphere of $1 \cdot 10^{-6}$ mbar. *Figure* 4.1 presents the LEED pattern of the crystal after the O_2-treatment where clear additional diffraction spots appear, indicating the creation of a surface superstructure. In order to obtain a clean W surface the crystal is then flashed up to 2300° C for a few seconds. The LEED measurements of the flashed crystal give a clear pseudohexagonal reflection spot arrangement showing that oxygen is removed. The cleanliness of the crystal was controlled by XPS; if

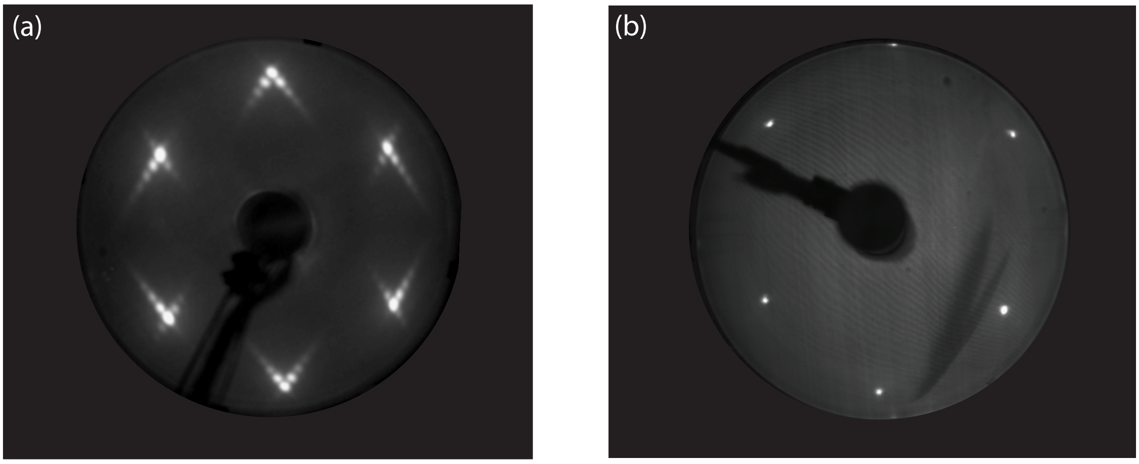

Figure 4.1: (a) shows the LEED pattern of a highly oxidized W(110) surface at $E_{\mathrm{kin}} = 78\,eV$ *of the electrons revealing a pseudo-hexagon because of the slightly different lattice vectors* ***a*** *and* ***b*** *in the two dimensional surface units cell of the W bcc. The additional spots arranged in cross-like structure surrounding the main W(110) reflection spots arise from the oxide layer, which grow in regular domains. (b) shows the crystal after three flashes. The additional spots of the superstructure have vanished indicating a clean W(110) surface at* $E_{\mathrm{kin}} = 91\,eV$ *of the electrons.*

impurity emission signals were observed, the cleaning procedure was repeat until all contaminations were removed from the surface.

Preparation of a Clean Ni(111) surface: Epitaxial Grown Thick Ni(111) Layer or Sputtering of a Macroscopic Ni(111) Crystal

The Ni layer was grown epitaxially on top of a W(110) substrate by depositing a 200 Å thin Ni film via a molecular beam. Subsequently annealing for 3 min up to 300° C followed by a 5 min cool-down phase to room temperature forms a highly ordered Ni(111) surface. The post-annealing is a very important step to receive a highly ordered surface starting a self-ordering process while the cool-down phase [120]. The self-ordering process is reflected in the improvement of the surface quality indicated by sharpness of the LEED diffraction spots and the sharpness of valance band structures as well.

The second method uses a macroscopic Ni(111) crystal. The cleaning procedure consists of sputtering and annealing cycles. While annealing to temperatures of 1000° C bulk contaminations segregate on top of the surface, similar to the annealing step of the W cleaning cycle. The resulting contamination layer was removed by sputtering with Ar^{+} ions of a kinetic energy of 2 keV. This cycle ends with an atomically clean but very rough Ni(111) surface. In order to smoothen the surface, the crystal was annealed for a short period up to 1000° C. The surface quality and cleanliness was controlled by LEED and XPS. If contaminations were observed the cleaning cycle was repeated.

Both methods are well established and they have been used successfully over decades. Sharp diffraction spots occur in the LEED pattern as shown in *Figure* 4.2 (a).

4.1.2 Growth of Graphene on Top of Ni(111)

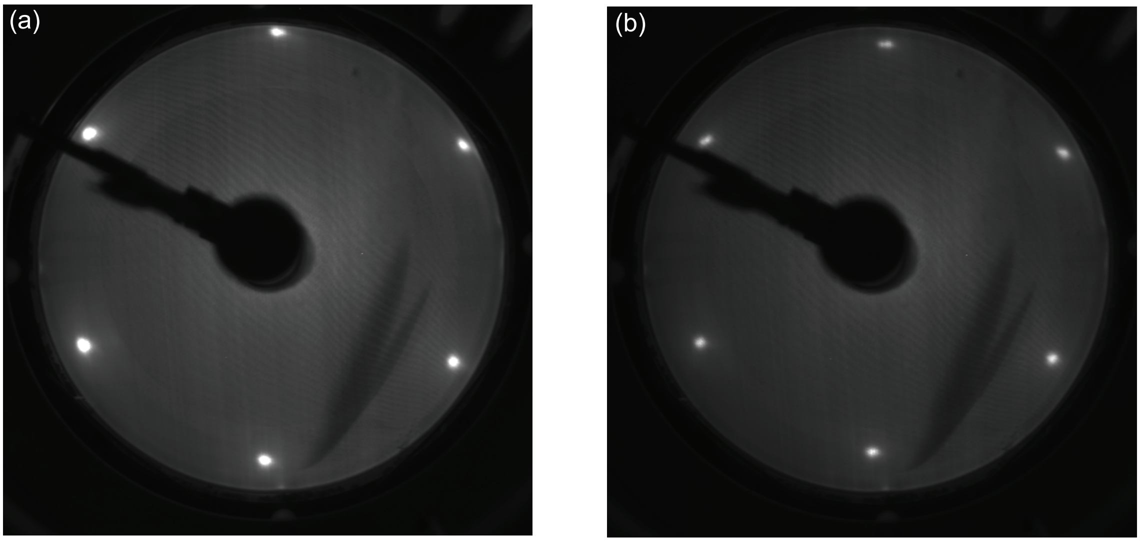

Figure 4.2: LEED pattern of Ni/W(110) measured at $E_{\mathrm{kin}} = 85\,eV$ and graphene/Ni/W(110) . The E_{kin} of the electrons was ≈100 eV.

The graphene layers were prepared in a CVD process on top of atomically clean Ni(111) surface. The crystal was heated up to 600° C for 3 min in order to attain thermal equilibrium. After this preheating, propylene gas up to a pressure of $1{\cdot}10^{-6}$ mbar was introduced into the preparation chamber for 15 min to 20 min. Subsequently, heating was stopped and the crystal cooled down to room temperature under the propylene atmosphere. At lower processing times (less than 10 min) a partially complete graphene layer was observed indicated by a less intense C 1 *s* peak in XPS measurements and weak graphene bands in the ARPES spectra. For processing times of more than 20 min, no changes were observed, due to the catalytic action of the Ni surface to this reaction and the passivation of the Ni surface by the graphene layer [123, 124]. This behavior was already observed in graphene on TaC(111) [125].

The quality of the graphene/Ni(111) sample was verified with LEED, XPS, ARPES and STM measurements and is discussed in the following chapters. The occurrence of hexagonally arranged diffraction spots in the LEED pattern, without any remarkable differences compared to the LEED pattern of graphene/Ni(111), shows that graphene grows in a (1×1) structure on top of Ni(111) (see also *Figure* 4.2 (b)), a threefold symmetry of the reflection spot intensities was observed by varying the kinetic energy of the electrons in the LEED measurements. The occurrence of this threefold symmetry indicates inequivalent chemical environments for the two C atoms. These differences of the environments influence the diffraction

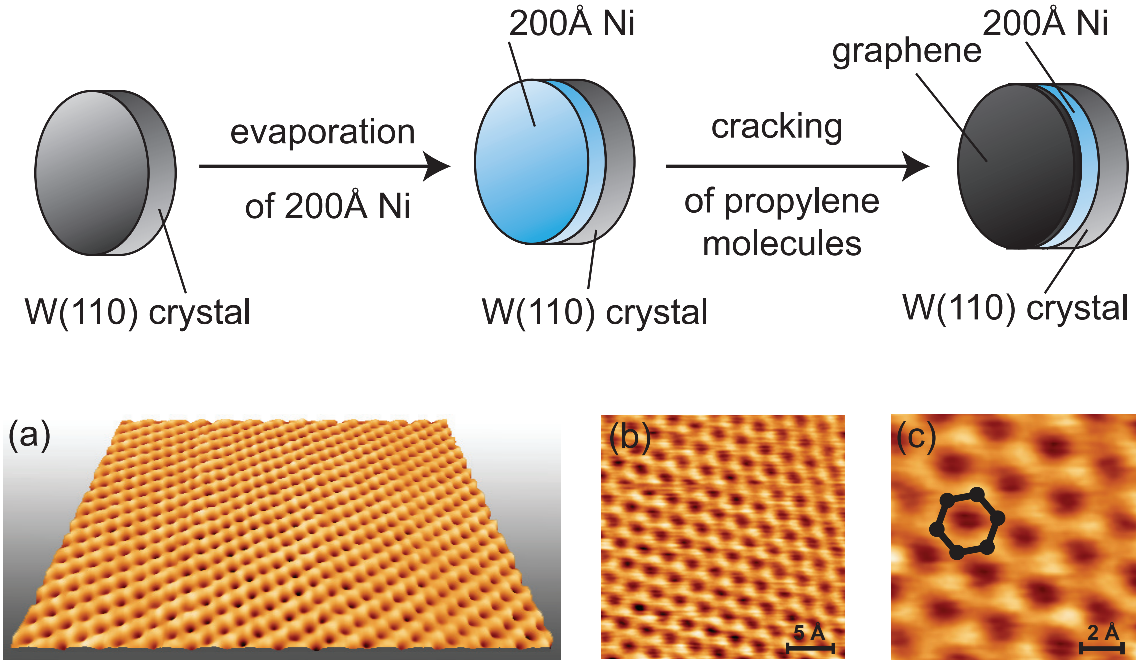

Figure 4.3: Preparation steps and STM images of graphene/Ni(111): The upper part shows the stepwise preparation of a graphene/200 Å Ni/W(110) sample via epitaxial growth of Ni followed by a CVD growth of graphene. In the lower part STM images using different zoom are shown (deduced from [126]).

potential of the graphene surface leading to differences in spot intensity.

In the upper part of *Figure* 4.3 the preparation steps and the layered structure of graphene/Ni/W(110) are shown.

4.1.3 Growth of Multilayer Graphene on top of Ni(111)

The preparation of ordered graphene multilayers on Ni(111) is complex and I give only an overview of the experiences obtained during a long series of preparation experiments. First, in order to overcome the passivation effect of the first strongly bound graphene layer, pyridine C_5H_5N was used as the precursor gas at higher pressures $> 1 \cdot 10^{-6}$ mbar. Additionally, a doser positioned 2 cm in front of the Ni(111) surface was used to guide the gas toward the surface. Therefore the pressure at the Ni(111) surface can be assumed to be much higher compared to the rest of the chamber.

In a first series of sample preparations, the influence of the temperature was studied, starting from 480° C and heating to 850° C over a process time of 10 min. Three temperature regions were found which lead to different graphene growth layers. For preparation temperatures below 500° C, the growth was self-limited, similar to recently published results [127] in which nitrogen containing hydrocarbon precursor gases were also used. In the temperature range from 500° C to 590° C, multilayer graphene structures grow on the surface. For temperatures above 590° C the growth stops after growth of a high quality single graphene layer without any remarkable N content. From the fact that for a temperature above 590° C the self-limiting growth arises simultaneously with the loss of any N impurities it can be speculated that the contained N atoms acts somehow as the starting point for the next layer.

After the preparation of a monolayer graphene with or without N impurities, subsequent reheating and exposition to a pyrdinic atmosphere did not affect the monolayer. The growth did not proceed. The reason why it runs only in a one step process is still unclear.

An influence of the cracking time on the multilayer graphene could not be found. Based on the knowledge of the growth of single layer graphene, process times longer than 10 min were chosen. Cracking times for longer times such as 30 min also show no clear effect on the number of layers.

Difficulties in the preparation of graphene arise from the influence of the pyridin precursor gas on the vacuum chamber. First of all, pyridin sticks to the walls of the chamber leading to a long recovery period before the pressure is back in the 10^{-10} mbar region. Therefore, the exposure time cannot be clearly defined. Further, pyridine renders ceramics conductive after ≈ 4 min. This is a problem for the ion gauges which begin to give false readings, making a controlled preparation very difficult. This also affects the e^{-}-beam heater, used here to heat sample, to malfunction.

In summary, a clear preparation method was not found. A more fruitful approach can be to look for other precursor gases which do not strongly affect the measuring devices and show the growth of multilayer as well. The experimental setup should be equipped with a small reactor chamber in order to reduce the pumping volume leading to a more precise process time. These suggestions together are strongly advised in order to find controllable preparation methods.

4.1.4 Intercalation of Fe, Al and Au underneath graphene on top of Ni(111)

The phenomenon of intercalation was intensively investigated in the 1970‘s and 80‘s in graphite intercalation compounds. It was found that it is possible to intercalate many elements, even up to entire molecules. These foreign particles are placed well ordered between the graphite planes. Between which planes the particles are placed upon intercalation depend strongly on the type of particle [2]. Similar behavior was observed in the special case of single layer graphene (monolayer graphite) [52, 128–132]. As in graphite intercalation compounds, the intercalation process for graphene depends on the foreign particles. It was observed that only one monolayer of Au intercalates, while Cu intercalates up more than 10 atomic layers [130, 131]. The mechanism of the intercalation is still under contrary debate. Several scenarios are favored, the first is that the foreign particles use steps, edges or defects to intercalate [133]. A further scenario describes the intercalation as an atom exchange.

Another description of the process is supported by the changes of the orientation of the graphene layer indicating a dissolution of the graphene layer in the intercalation metal layer followed by a regrowth of the graphene layer on top of the intercalated layer. In this process a reorientation is easily possible rather than a rotation of a full graphene sheet during the intercalation process. The intercalation of metals Al, Fe and Au were selected because of their significance for future electronics. The intercalation of the Fe and Al was performed on graphene/Ni(111) samples. The intercalation of a Au monolayer underneath multilayer of graphene was also studied.

For the intercalation of Fe, an 1ML thick Fe layer was deposited on top of graphene on Ni(111). The pressure during the metal deposition did not exceed $8{\cdot}10^{-10}$ mbar. Subsequently, the sample was annealed up to 300° C for a period of 10 min. The intercalation process was observed and controlled by changes in the XPS core-level emission intensity [123]. The increased C 1*s* signal intensity accompanied by a decrease of the Fe core-level signals shows that Fe is intercalated underneath the graphene layer (see *Section* 6.1). Based on the Fe stabilization in a (1×1) structure no changes occur in LEED images.

In order to intercalate one monolayer underneath graphene on Ni(111), one atomic layer Al was deposited on top. In Al intercalation experiments, a temperature of 400° C for a few seconds was found to be a good process parameter. The intercalation was controlled by LEED, XPS and ARPES measurements (see *Section* 6.2). Strong changes such as the occurrence of a superstructure in LEED and the restored Dirac-cone in ARPES experiments clearly indicate a successful intercalation process (see *Section* 6.1). The challenging difficulty of the Al intercalation process is the fact that Al can easily dissolve into the Ni bulk. Higher temperatures or longer annealing periods lead to a completely dissolving of the Al into deeper regions of the Ni bulk, leading to a fully restoration of the graphene/Ni(111) signature in ARPES and LEED experiments.

The intercalation of Au was performed on a multilayer of graphene after annealing to 300° C for 2 min. The graphene layer becomes fully decoupled via Au intercalation verified in ARPES measurements (see *Chapter* 7). The detailed discussion of the control of the intercalation process is presented in the respective chapter.

Chapter 5

Electronic Structure of Graphene on Ni(111)

In this chapter the results of experimental and theoretical investigation of the graphene/Ni(111) system are presented and discussed from the aspects of fundamental research and possible future applications. Graphene on Ni(111) is an interesting system in the field of graphene research. The unique conditions in this system are the good lattice fit of the graphene adlayer to the Ni(111) surface and the strong interaction between the ferromagnetic $3\,d$ bands of the Ni substrate and the graphene π system.

5.1 Crystallographic Structure

The prepared graphene layer was structurally characterized by LEED measurements. For comparison of the pure Ni and the graphene/Ni(111) system, both LEED images are presented in *Figure* 5.1 (a) and (b), respectively. These measurements show, in the case of graphene/Ni(111), a hexagonal diffraction spot arrangement with the same dimension and orientation as the atomically clean Ni(111) surface. This implies that graphene grows in an (1×1) structure on top of Ni(111). The possibility to grow in this structure arises from the very good lattice match between a graphene layer and the Ni(111) surface. The difference between the lattice constant of graphene and Ni(111) is only ≈1.3 % [16, 134, 135]. The earlier published STM results [126], shown in *Figure* 5.1 (d) and (e), clarify that graphene stays as a flat layer on top of Ni(111), in contrast to systems such as graphene/Ir(111) or graphene/Rh(111) where the lattice mismatch leads to a buckled graphene top layer [16, 55, 60, 132, 136]. Starting from the lattice match between graphene and Ni(111) several crystallographic arrangements of the (1×1) structure are possible. In the literature, the widely accepted structure of graphene/Ni(111) has the carbon atoms arranged in the so-called *top-fcc* configuration on Ni(111), shown in *Figure* 5.1 (c) [67, 134, 137]. In this arrangement, one sublattice is on top of the Ni atoms, labeled as $\mathrm{C^{top}}$, the other sublattice is on the fcc hollow site above the Ni(111) atom of the third Ni layer, labeled as $\mathrm{C^{fcc}}$. This structure model is supported by the contrast in

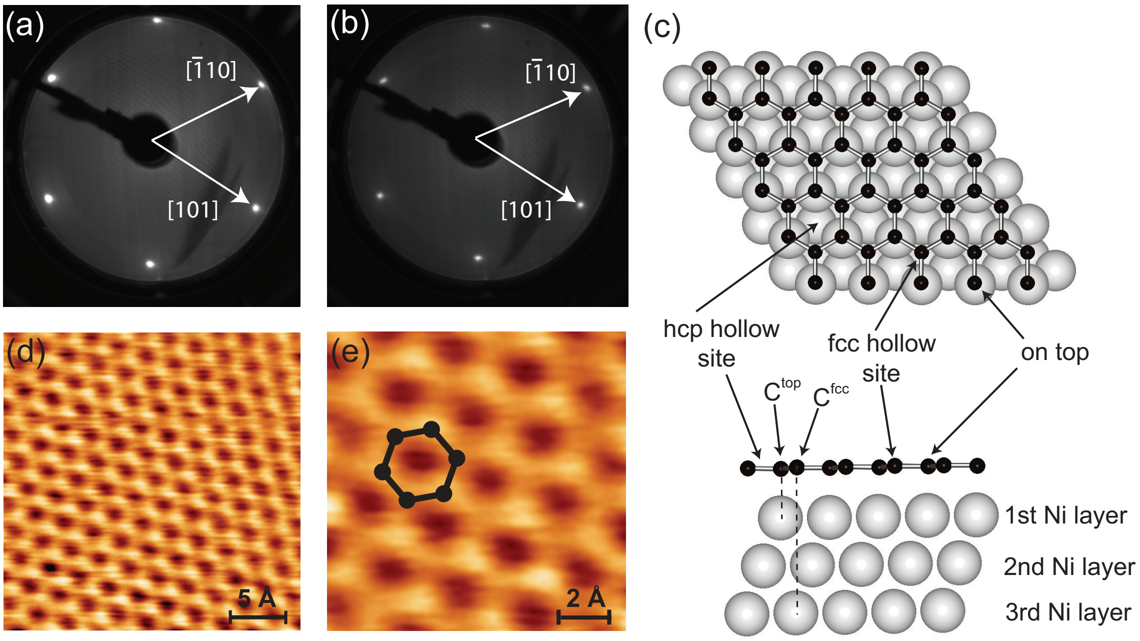

Figure 5.1: The LEED spots for the graphene/Ni(111) surface (b) appear in exactly the same arrangement compare to the clean Ni(111) (a). The favored structure model is presents in (c). In STM images (d) and (e) no superstructure can be observed.

the STM results presented in *Figure* 5.1 (e).

In the STM data the contrast differs between two atoms of the graphene unit cell, suggesting non-equivalent positions of both C atoms over the Ni(111) surface. Further, a three-fold symmetry of the diffraction spot intensity is observed in LEED measurements when varying the kinetic energy, also supporting the idea that different positions are occupied by the two C atoms in one unit cell as well. A small displacement of 0.005 Å in the height between both C atoms in one unit cell was reported in LEED intensity measurements at an early stage [137]. This displacement in the height between the non-equivalent C atoms is in good agreement with the results of DFT calculations, presented in *Section* 5.6. These calculations give a distance between the first Ni layer and the C atom of 2.145 Å in case of the $\mathrm{C}^{\mathrm{top}}$ atom and 2.146 Å in case of the $\mathrm{C}^{\mathrm{fcc}}$ atom. This distance much is smaller than the interlayer distance in graphite ($d_z = 3.37$ Å [1]); indicating a stronger interaction between the graphene and Ni compared to the weak interlayer interaction in graphite.

5.2 Core Level Spectroscopy

The XPS core level spectra of graphene/Ni(111) are presented in *Figure* 5.2. All features in the overview spectrum can be assigned to the graphene on Ni(111) system and the W(110) substrate. The C 1*s* peak consists of a single component and appears at 284.7 eV binding energy, in good agreement with earlier published results [123, 138]. In the overview spectra no contamination signals are visible. The absence

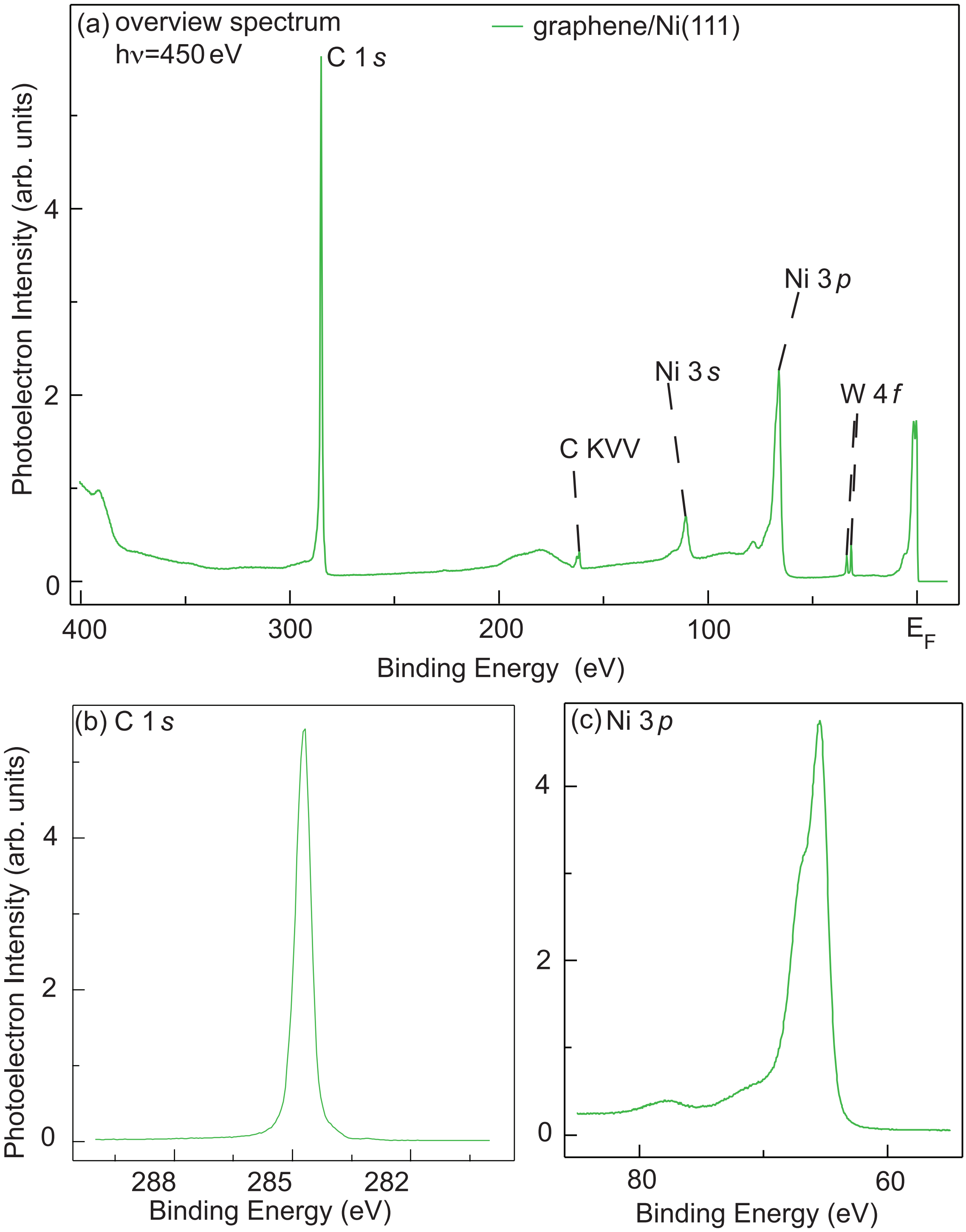

Figure 5.2: Core level and overview spectra of graphene/Ni(111) taken at 450,eV photon energy: (a) shows overview spectrum spectra of graphene on Ni(111). Diagrams (b) and (c) show the C 1s and the Ni 3p peak measured with a higher resolution.

of additional components of the C 1 *s* emission peak is sign of the cleanliness as well. The occurrence of several components would indicate that C atoms exist in different chemical environments reflected by a chemical core level shift. The C 1 *s* and Ni 3 *p* emission spectra, shown in *Figure* 5.2 (b) and (c), respectively, were measured with higher resolution. A frequently observed small peak in XPS spectra of graphene/Ni(111) at 284 eV is not visible. This peak can be assigned to a Ni carbide phase [139]. The absence of this peak is thus a sign of the high quality of our films.

The doublet structure at 31.5 eV and 33.7 eV binding energy belongs to the W 4 *f* level [92]. Based on the high photon energy and the large amount of W bulk underneath the graphene/Ni(111) sandwich layer this core-level is still visible. It shows that the thickness of the Ni layer was overestimated or the Ni film is broken during the cracking procedure. In ARPES spectra no W(110) valence band features are visible indicating that if the Ni is broken it happened only at rear places.

5.3 ARPES Results

The ARPES spectra, shown in *Figure* 5.3, were measured at a photon energy of 65 eV. This photon energy was found to yield an optimal ratio between the graphene π and the Ni 3 *d* states cross sections [92].

In this data the valence band structure of graphene/Ni(111) appears strongly modified compared to the band structure of free-standing graphene [13, 15]. Around the Γ point the parabola-like π band appears at 10.3 eV binding energy, a shift of 2.4 eV downwards to high binding energies. Near the K point the π band does not reach the Fermi level as known from free-standing graphene occurring at 2.8 eV binding energy [140]. Above 2.8 eV, a triangular shape intensity structure with a clear minimum at the center is visible (see also *Figure* 5.5). Two sides of the triangle are the continuation of the π band. The horizontal side of triangle belongs to the 3 *d* Ni states which occur between 2.5 eV and E_F. The $\sigma_{1,2}$ bands are hardly visible at the Γ point below 4.5 eV. The weakness of the emission intensity of these states follows from the small cross sections of the photoemission process of these states in the first Brillouin zone [141]. In contrast to the π band, which becomes distorted around the K point, the σ bands appear similar as in free-standing graphene, but are rigidly shifted to higher binding energies, by about 1 eV. The experimental results in *Figure* 5.3 (a) for the graphene/Ni(111) system are in very good agreement with the previously published experimental and theoretical data [126, 129, 130, 134, 142, 143]. The observed differences in changes between the π and σ states indicate that the interaction between the graphene and Ni(111) is mainly restricted to the graphene π band and the 3 *d* Ni states.

The varying extent regarding the changes in shift and line shape of the π and the σ bands can be explained by the different strengths of the interaction with the electron system of the Ni substrate. The main reason for this is the different orientation of the molecular orbitals from which the π and the σ states originate. The σ bands arise from the overlap of the the sp^2 hybridized C 2 *s*, 2 p_x and 2 p_y orbitals.

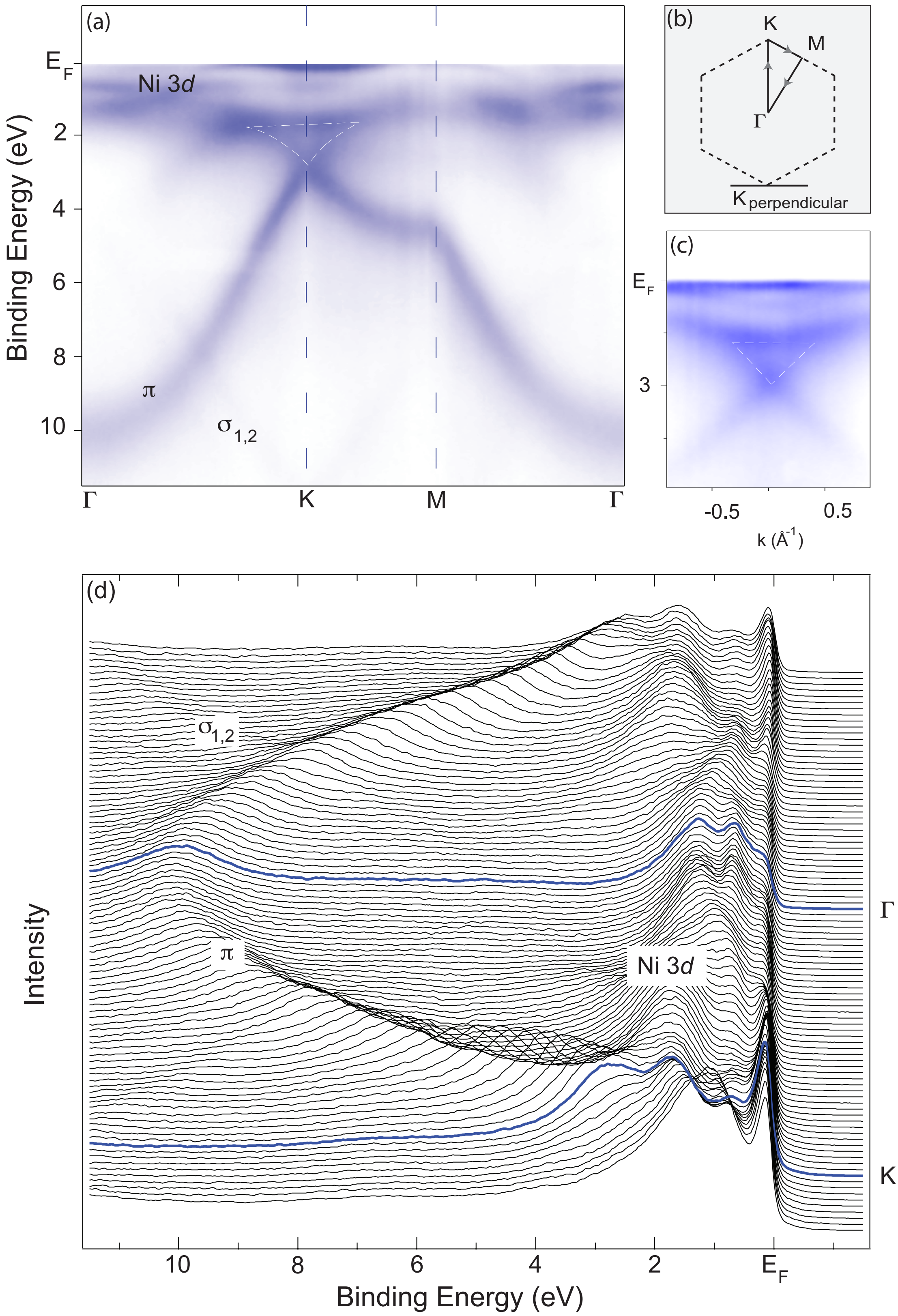

Figure 5.3: ARPES spectra of graphene on Ni(111) taken at photon energy of $h\nu = 65$ *eV. (a) shows a band map through the Brillouin zone along the high symmetry axis* Γ*-K-M-*Γ*. (b) presents a waterfal plot along the* Γ*-K direction.*

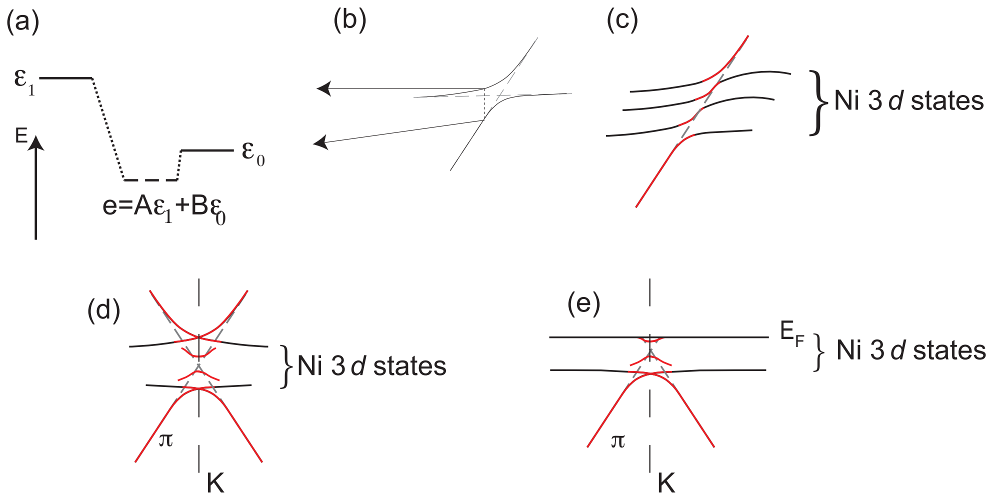

Figure 5.4: Schematic overview of orbital interactions. (a) Two states with energies ϵ_0 and ϵ_1 interact. The mixed state e has a smaller energy compared to the single states ϵ_1 and ϵ_0. The ratio between A and B is defined by the energy difference $E(\epsilon_1) - E(\epsilon_0)$. In a band situation this is reflected in (b) by the repulsion of bands near the former crossing point. (dashed lines), which leads to a new dispersion (solid lines). In the case of Ni(111) three different 3d electron states (d_{xz}, d_{yz} and d_{z^2}) can participate in an interaction with the graphene π states presented in (c). The π band crosses the three Ni states at the Brillouin zone border which leads to a mirror-like behavior shown in (d). In (e) a hypothetical Fermi level is added.

These hybridized orbitals are directed to the neighboring C atoms (see *Figure* 2.2). Hence, the σ electron system lies in the plane of the graphene layer. This in-plane orientation leads to a very small overlap of the σ state wave functions with the Ni 3 *d* state wave functions in real space. The π band originates from the overlap of the p_z orbitals which are orientated out-of-plane with respect to the graphene layer [138, 142, 144]. A detailed discussion of the orientation follows in *Section* 5.4 below. This out-of-plane orientation leads to a remarkable real-space overlap of the π electron system with the electron system of the Ni substrate. Similar to the π and σ bands, the Ni 3 *d* bands only participate strongly in the interaction if the original *d* orbitals have a z-component, such as d_{xz}, d_{yz} and d_{z^2}.

The interaction of the Ni(111) substrate with the σ states is restricted to a downwards shift, indicating an n-doping of the graphene layer. This is consistent with a core level shift of about 100 meV of the C 1 *s* to smaller binding energies, originating from the higher electron negativity of C compared to Ni [145]. This n-doping affects the π states as well.

However, the π states are shifted further by about 1.4 eV and occur in a distorted line shape at the K point, a fact that cannot appears from a doping effect. These additional changes can be assigned to a strong hybridization between the π states and the Ni 3 *d*.

Let us briefly sketch the principles of the band hybridization in a simplified schematic picture.

If two states with different energies ϵ_0 and ϵ_1, as shown in *Figure* 5.4 (a) become occupied by a single particle classical physics would places by 100 % the particle into the state at smaller energy.

Quantum theory uses the concept of expectation values and the probability of finding to define a particle at one or several states. In the example in *Figure* 5.4 (a) quantum theory would places partly in both states, because of the energy uncertainty principle and the energy gain from the quantum statistic. The resulting wave function occurs as a superposition $e = A\epsilon_1 - B\epsilon_0$ of both single states. The ratio A/B is defined by the energy difference $E(\epsilon_1) - E(\epsilon_0)$. An increase of the energy difference would increase the amplitudes of state at lower energy. In the case of the states have the same energy the particle exists by half and half in both states. Because of the superposition the resulting states have characters of both original states such as π or d character in the graphene on Ni(111). Therefore this effect is called hybridization. A further requirements for a strong hybridization is a significant real space overlap which requires the equivalence of the symmetry of the original electron systems.

In the next paragraphs the concept of hybridization will be applied to the graphene/Ni(111) band structure. The $3\,d$ bands of Ni occur in an energy region between the Fermi level and 3 eV binding energy. Three bands originate from d_{xz}, d_{yz} and d_{z^2} states and exhibit a significant real space overlap with the graphene π states. The lattice match between the graphene and the Ni(111) surface ensures the equivalence of periodicity supporting the real space overlap further. Therefore these three $3\,d$ bands can hybridize with π states.

Special attention has to be paid to the situation at the Brillouin zone border around the K point, because the π and $3\,d$ states have similar binding energies here. In other regions such as around the Γ point the $3\,d$ and the π states are well separated. As a consequence, hybridization effects can only occur around the K point. The Brillouin zone border acts as a mirror plane as shown in *Figure* 5.4 (e).

This model reproduces well the π band structure at the K point observed in the ARPES experiment. The hybridized π and Ni $3\,d$ bands together with unaffected Ni $3\,d$ bands reproduce the triangular shaped intensity. In this model two new hybridization states appears in the band gap between π and π^*. In the region of the superposition between the π states and Ni $3\,d$, the resulting wave functions have mixed character from electronic π and $3\,d$ states supported strongly by the DFT calculation results discussed below.

A hint of the strength of the character mixture between π states and $3\,d$ states is obtained from constant energy cuts above and below 2.8 eV binding energy, at which the π band touches the $3\,d$ Ni bands. The constant energy cut at 2.5 eV binding energy through the triangular hybridization structure is shown in *Figure* 5.5 (b). The hybridized bands possess mainly $3\,d$ character at this energy. This becomes obvious from the intensity paths along the Γ-K and K-M-K directions, starting at the K point, *Figure* 5.5 (b). If the hybridized bands at 2.5 eV were a

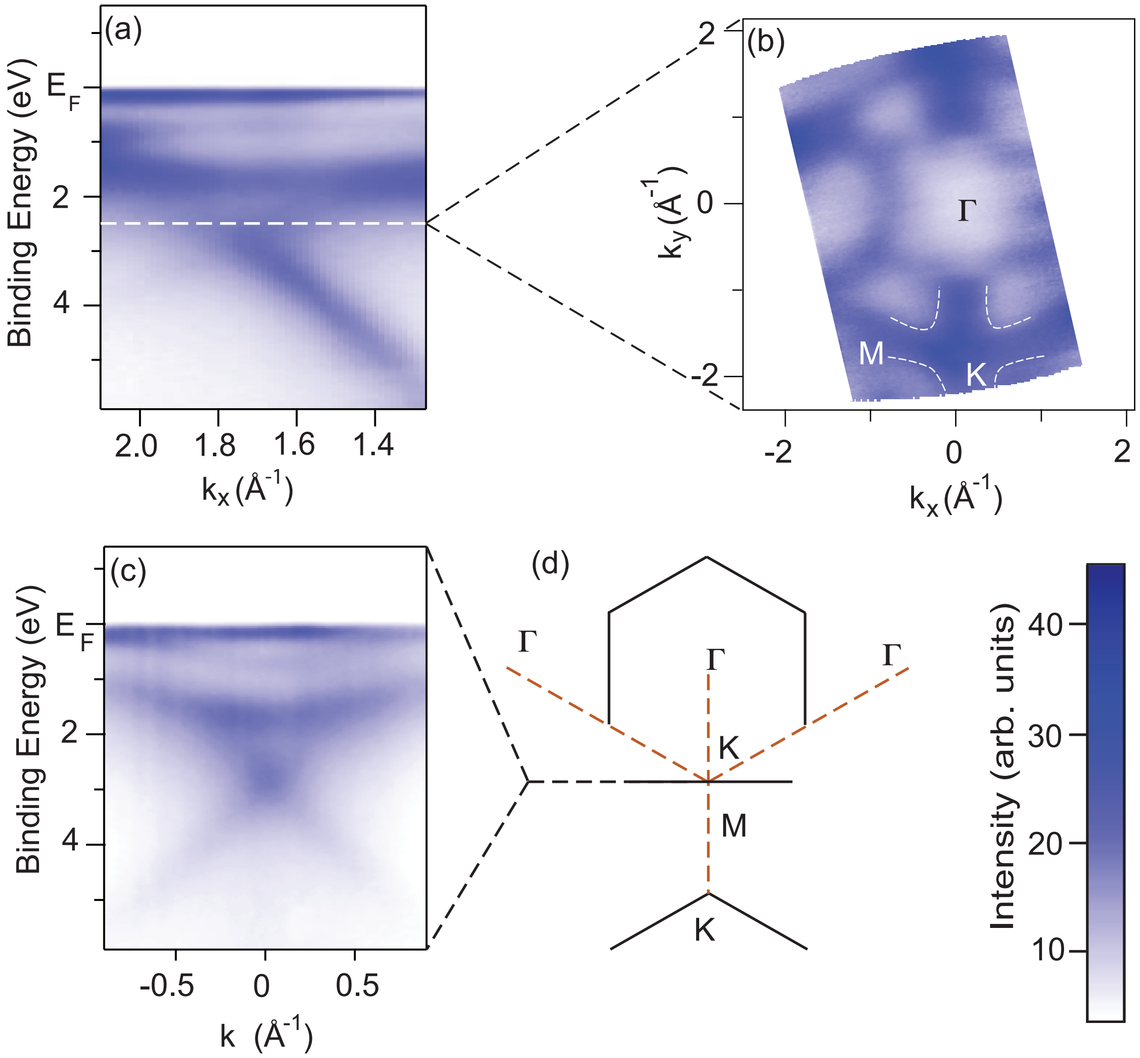

Figure 5.5: ARPES spectra of graphene/Ni(111) presented in (a), (b) and (c) measured at a photon energy of 65 eV: (a) and (c) are cuts through the K points along and perpendicular to the Γ*-*K *direction. (b) shows a constant energy cut at 2.5 eV binding energy. The 3 d Ni bands which are related to hybridization can be clearly seen. (d) gives a top view scheme of the Brillouin zone. Orange dashed lines marks the direction of the 3 d bands which contribute to the hybridized states.*

strong mixture of π and d character or mainly π character, a triangular or circular intensity distribution centered at the K point would be expected, similar to π^* band in free standing graphene.

Below 3.1 eV binding energy the graphene π band appears with pure π character (see also *Figure* 5.6 (a)). From this we can conclude that in this energy range, the hybridized bands are created by the p_z orbitals. The range containing a mixture of both d and π characters is restricted to an energy window of less than 600 meV.

However, the question of the exact band gap size between π and π^* cannot be

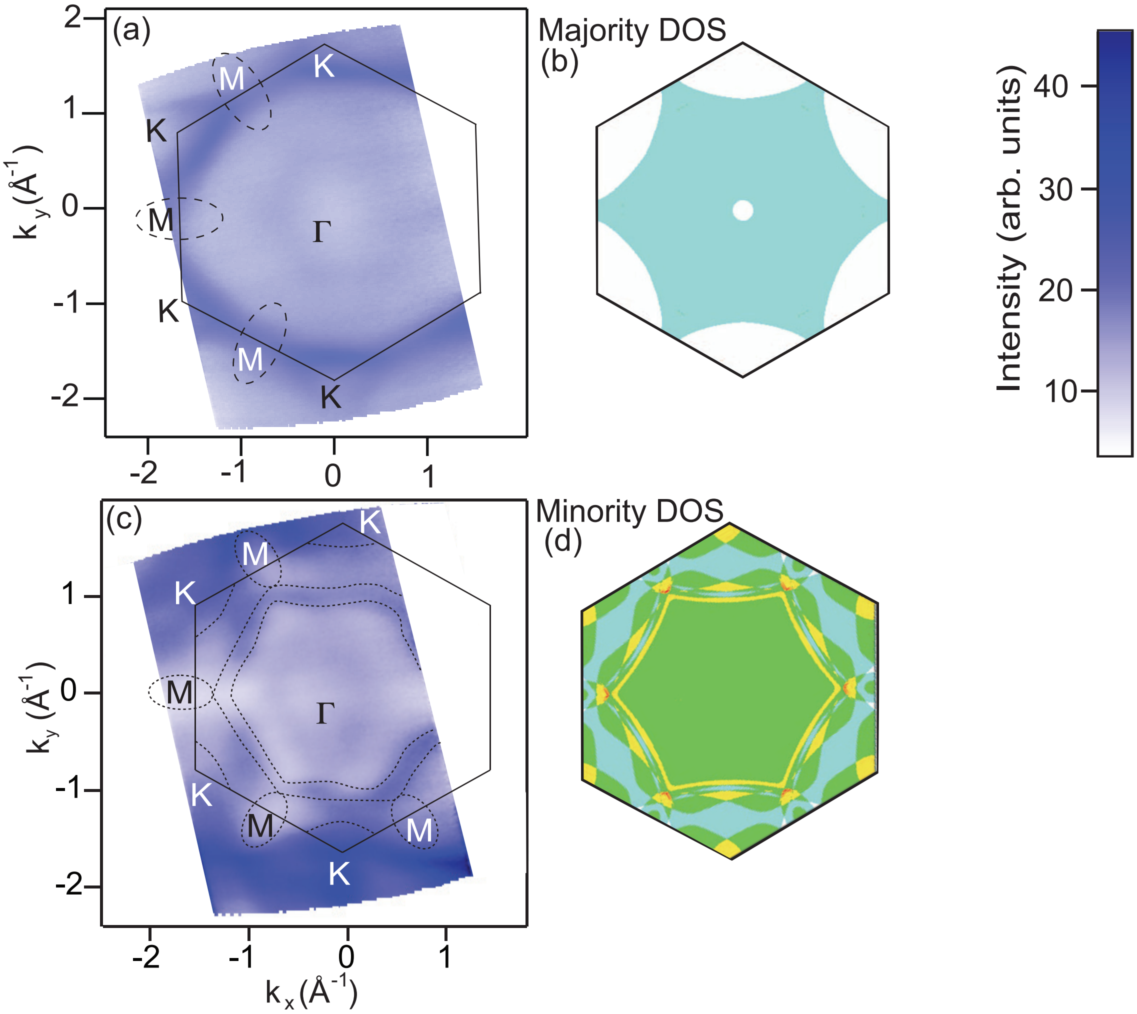

Figure 5.6: (a) and (c) constant energy cuts of graphene/Ni(111) at 4 eV binding energy and the Fermi level, respectively: In the Fermi energy cut at the M points bright ranges appear that show less intensive regions. (b) and (d) show the Fermi surface density of the bulk Ni projected on the (111) surface [12, 67].(figures (b) and (d) deduced from [67])

answered by these experimental data. In the spectra in *Figure* 5.3 (a) and *Figure* 5.6 (a), a strong intensity close to the Fermi edge appears near the K point. This could be related to the lowest states of the π^* band. However, calculations also show an increased density of the minority 3 *d* Ni states [12, 67]. Furthermore, a superposition of photoelectron intensity of different states can be assumed in this range. The answer about the originating states' character is not given by experimental results. Finally a the lower limit of gap size as 2.6 eV can be concluded.

Note, however, that in a recent paper by Varykhalov *et. al* an interpretation of the photoemission intensity from graphene on Ni(111) and Co(0001) in this region is given which proposes that no gap appears at all at the K point; in other words, the crossing of the bands in *Figures* 5.5 (a) and (c) is interpreted as a Dirac cone of the π band. Therefore they used a strong doping to explain the downwards shift of the Dirac cone by 2.8 eV. From my point of view this explanation is not valid, because it contradicts the small shift of the σ states. At present the debate on the correct interpretation of these features is still going on.

The intensity behavior of the π band supports the model of the crystallographic structure from *Section* 5.1. The observation that the π band vanishes in the second Brillouin zone was explained by Shirley *et al.* in 1995 [141] as a destructive interference of two electrons emitted from different sublattices. The occurrence of a weak intense π band in the second Brillouin zone indicates an asymmetric potential of the two sublattices. In graphene/Ni(111) all C atoms of one sublattice are located on top of the Ni atoms and all C atoms of the other sublattice are on a fcc hollow site as shown in *Figure* 5.1 (see also [134, 144]). This difference in the position for all atoms of one sublattice compared to all atoms of the other one leads to a strictly different potential for these sublattices. From this, the final state wave function of electrons from one sublattice becomes slightly changed with respect to the final state wave function of the emitted electrons from the other one. Therefore, the condition of destructive interferences is not exactly fulfilled. Such a behavior has already been observed in graphene/SiC samples [146].

Figure 5.6 (c) shows a constant energy cut of graphene on Ni(111) at the Fermi level. In comparison with theoretical spin-resolved bands, projected onto the (111) surface the increased intensity at the K points and the hexagonal structure at the inner part of the first Brillouin zone can be assigned to the minority spin states of the Ni(111).

5.4 X-Ray Absorption Spectroscopy

In order to study the graphene orbital orientation at the graphene/Ni(111) interface, linearly polarized light was used and the sample orientation relative to the x-ray wave vector was varied [102]. Moreover, the detection mode was chosen as PEY because it is more sensitive to the interface compared with TEY. The C 1 s NEXAFS spectra of the graphene/Ni(111) system were measured as a function of the angle α between the direction of the incoming linearly polarized light and the surface of the sample, i.e., between the electrical vector of the light and the sample normal as shown in the inset in *Figure* 5.7. The NEXAFS spectra of a graphite crystal measured at 30° and 90° are shown in the upper part of the figure and are used as a reference (the spectra were taken from [147]). Spectral features observed in the photon energy regions from 283 eV to 289 eV and from 289 eV to 315 eV are ascribed to C 1 $s \rightarrow \pi^*$ and C 1 $s \rightarrow \sigma^*$ transitions, respectively. The NEXAFS spectra of graphite could only be explained by assumption of a poor core-hole screening and excitonic effects [148–152]. Following from the similar line shape of the C 1 s absorption edge for graphene on Ni(111) it can be concluded that the same processes occur. In the case of the graphene/Ni(111) system, the NEXAFS C 1 $s \rightarrow \pi^*, \sigma^*$ spectra show considerable changes compared with the graphite spectra, indicating a strong chemisorption. The

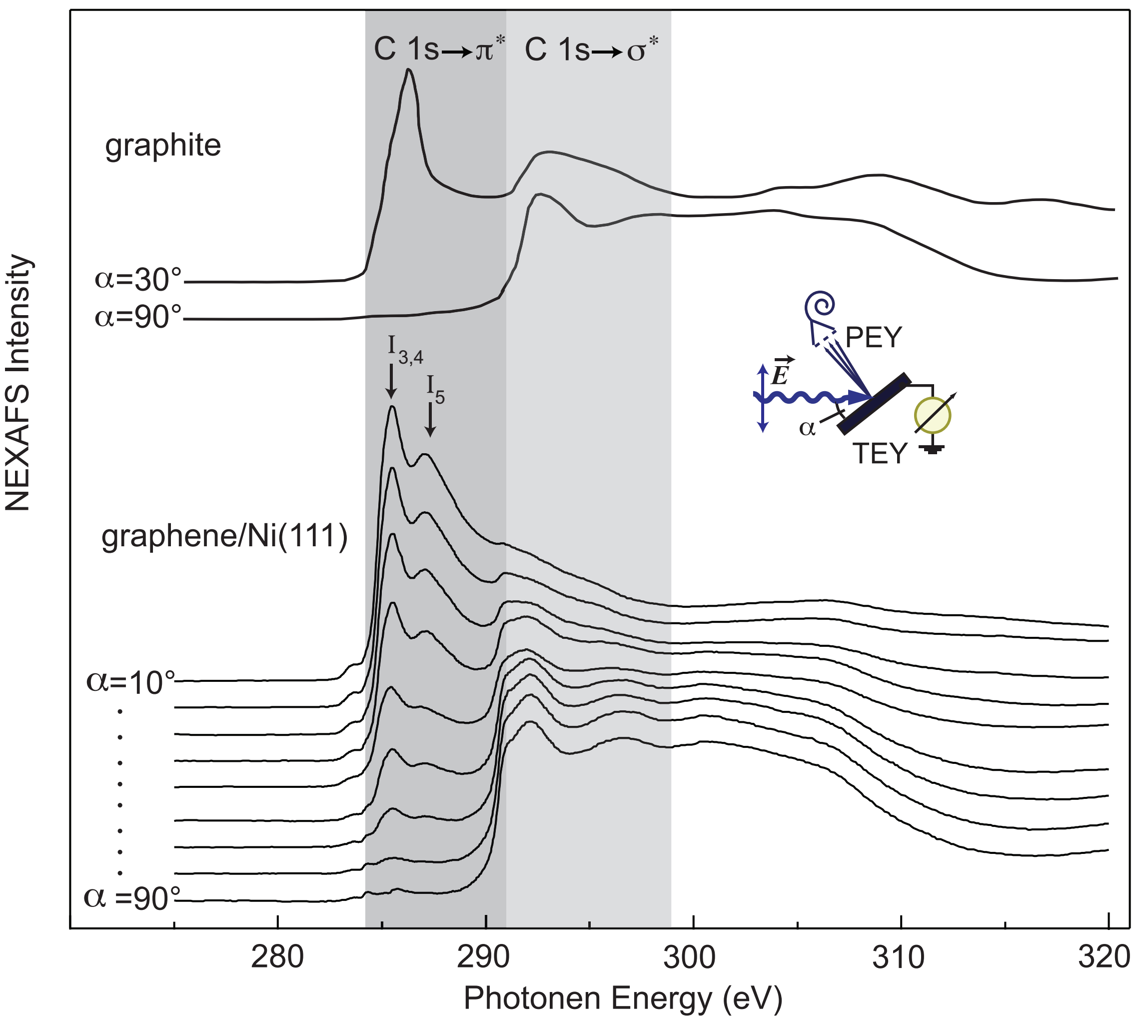

Figure 5.7: Series of NEXAFS spectra of graphene/Ni(111) for varied angles starting from 10° to 90°: The NEXAFS spectra of graphite, deducted from [147], in the upper part serve as a reference. In relation to the XAS spectra of graphite, the XAS spectra of graphene/Ni(111) can be separated into two photon energy regions with a opposite angle dependence. The first region, dark gray shaded, from 283 eV to 289 eV is assigned to the π^* resonance of graphene, while the second region, bright gray shaded, is assigned to the σ^* resonance. Moreover, both resonances shows considerable changes compared to the XAS spectra of graphite that indicates a strong interaction to the Ni substrate.

small shoulder visible in the NEXAFS spectra at 283.7 eV photon energy can be associated with the excitation of electrons from the C 1*s* level of the C atoms which stay in the carbidic phase. Since this feature does not demonstrate any dichroic signal (see *Section* 5.8) it will not be discussed any further.

In contrast to the NEXAFS spectra of graphite a double peak structure occur in the π^* resonance region at 285.5 and 287.1 eV photon energy. These peaks can be analyzed by DFT calculation, shown in *Section* 5.6, and recently published calculations of the C K-edge electron energy loss spectra for the graphene/Ni(111) interface [134]. Both calculations shows the creation of several interface states I_{1-5} (see also *Table* 5.1 and *Figure* 5.9). $I_{3,4}$ occur in the energy region from 0.12 eV to 0.55 eV above the Fermi level, therefore the absorption signal at 285.1 eV photon energy can be assigned to a C $1\,s \rightarrow I_{3,4}$ transition. These states are created by C p_z−Ni $3\,d$ hybridization. The absorption signal at 287.1 eV photon energy can be assigned to a C $1\,s \rightarrow I_5$ transition. This state I_5 occur 3.2 eV above the Fermi level and originates to hybridization between the C p_z and the Ni *sp*, $3\,d$ states.

After the assignment of the main features to their origins, it is possible to analyzes the orientation of the originating orbitals. The angular dependence separates the NEXAFS spectra into two regions, the C $1\,s$ transition into the π^* and σ^* states. Both regions show a reverse light incident angular dependence. The C $1\,s \rightarrow \sigma^*$ transition has a clear maximum at $\alpha = 90°$. In this configuration, the electric light vector is parallel to the graphene layer, hence, all σ orbitals are oriented in-plane. In contrast, the spectral features from $1\,s \rightarrow \pi^*$ and interface states will have a maximum if the electric light vector is pointing out-of-plane. Therefore, it can be concluded that all p_z driven orbitals are oriented out-of plane with respect to graphene.

In summary, several interface states were identified investigating the excitation from the C $1\,s$ core-level into unoccupied states above the Fermi level with angular dependence. A further result is the orientation of the π electron system out-of-plane in contrast to the σ electron system which stays in plane. These results support the clear separation of the interaction between the two different graphene electron π and σ systems to the Ni substrate.

5.5 X-Ray Magnetic Circular Dichroism

XMCD spectroscopy of the C K and Ni $L_{2,3}$ edge was used to investigate the magnetic interactions between the graphene and the ferromagnetic substrate Ni(111), the results are shown in *Figure* 5.8. Based on the sum-rules the spin and orbital momentum of Ni were calculated as $\mu_S = 0.69\,\mu_B$ and $\mu_L = 0.07\,\mu_B$, respectively, from the Ni $L_{2,3}$ TEY XAS spectra. These values are in very good agreement with previously published Ni bulk values [153, 154] as well as with the spin-magnetic moment ($\mu_s = 0.67\,\mu_B$) calculated for the graphene/Ni(111) system [134].

Figure 5.8 (b) shows the dichroic signal at the C K edge. This signal shows unambiguously that Ni induces a magnetic moment in the graphene layer. In order to increase the measured magnetic contrast at the $1\,s \rightarrow \pi^*$ absorption edge, thiese XMCD spectra were collected in the PEY mode at an angle $\alpha = 20°$. The observed difference in the NEXAFS spectra collected at this angle in *Figures* 5.7 and 5.8 is based on the different polarization of the light as follows: it is linearly polarized in *Figure* 5.7, revealing strong angular dependence of absorption due to the different orbital orientation in graphene, and circularly polarized in *Figure* 5.8 where both $1\,\mathrm{s} \rightarrow \pi^*$ and $1\,\mathrm{s} \rightarrow \sigma^*$ transitions are nearly equivalent. The C K XMCD spectra show that the major magnetic response occurs in the transitions of the $1\,s$ electron

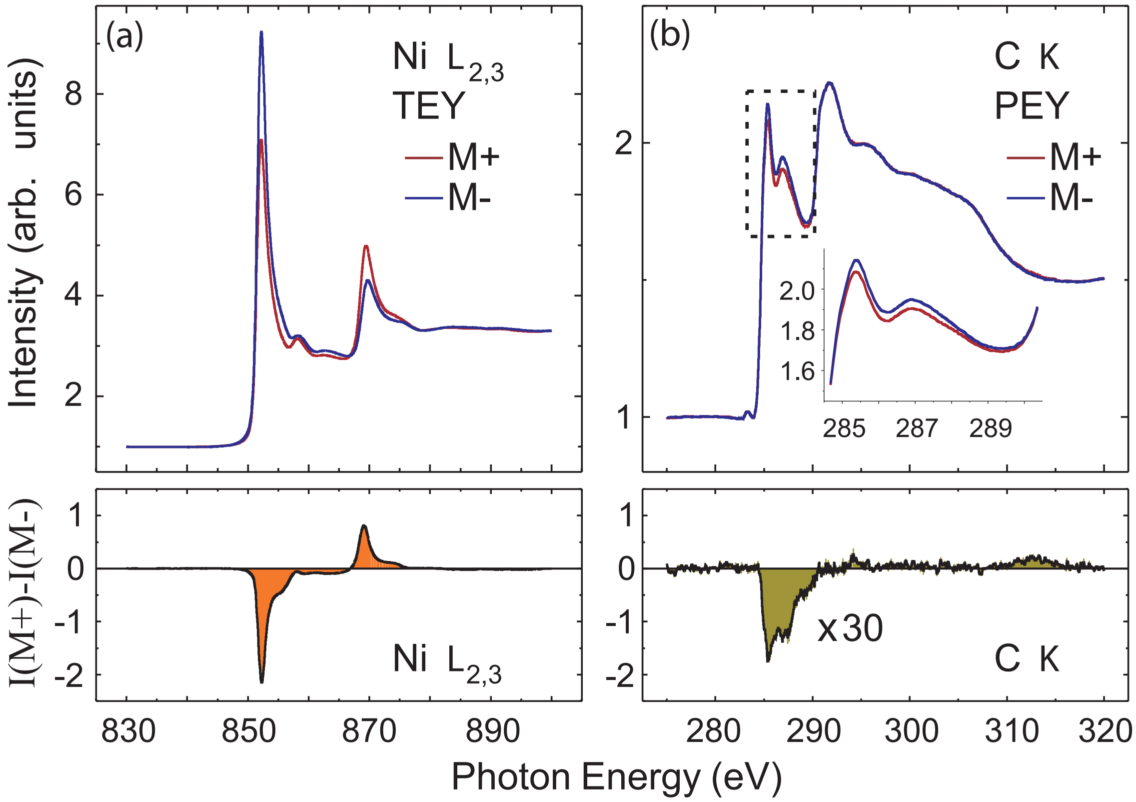

Figure 5.8: Absorption spectra for circular polarized light are shown of graphene/Ni(111): The upper left panel shows the Ni $L_{2,3}$ absorption signal for different magnetizations. In case of the C K edge this XMCD contrast, presented in the right panel, is ≈ 30 times smaller compared to the Ni contrast.

into the π^* states, while transitions into the σ^* states yield practically no magnetic signal, indicating that only the C p_z orbitals which hybridize with the Ni $3\,d$ bands are spin-polarized. The sharp structure at the $1\,\mathrm{s}\rightarrow\pi^*$ absorption edge originates from the hybridization between C p_z with Ni $3\,d$ and between C p_z with Ni p_x, p_y $3\,d$ states (see earlier discussion in *Section* 5.3 and [134]).

At the C K edge, transitions occur from non-spin-orbit-split $1\,s$ initial states to $2\,p$ final states. Thus, the corresponding dichroic signal can only provide information about the orbital moment [81, 82]. Regarding the negative sign of the XMCD signal, it can be concluded that the average orbital moment of carbon atoms, i.e., averaged over all carbon positions in the graphene layer, is aligned parallel to both, the spin and orbital moments of the nickel layer. Unfortunately, the orientation of individual spin and orbital moments of both Ni and C at different sites cannot be determined by the experimental XMCD data, because the absorption probability is measured simultaneously of all atoms.

At this point of the analysis, one may ask for a quantitative value of the induced magnetic moment per C atom. However, due to the impossibility to extract the spin magnetic moment from the K edge XMCD spectra, a comparison with similar systems may permit an estimation. Ferromagnetism of carbon in Fe/C multilayers was demonstrated and a magnetic moment of 0.05 μ_B was measured [155]. In these Fe/C multilayers, magnetism was shown to be related to the hybridization of the Fe $3\,d$ orbitals and C p_z orbitals exactly like in the case of graphene/Ni(111). In addition, induced magnetism in carbon nanotubes in contact with a flat ferromagnetic Co substrate was demonstrated and a spin transfer of 0.1 μ_B per carbon atom was deduced [156]. Considering these analogous systems, the induced magnetic moment for graphene on Ni(111) is estimated to be in the range of 0.05-0.1 μ_B per carbon atom.

5.6 Comparison of Experimental Results with DFT Calculations for the Graphene/Ni(111) System

The DFT calculations were performed by Dr. Elena Voloshina (FU Berlin) providing theoretical support of graphene/Ni(111) and graphene/ Ni(111) studies including intercalants. In DFT studies, the electronic and structural properties of the graphene-substrate system are obtained using the Perdew-Burke-Ernzerhof (PBE) functional [157]. For solving the resulting Kohn-Sham equation the Vienna Ab initio Simulation Package (VASP)[158, 159] with the projector augmented wave basis sets [160] was used. The plane-wave kinetic energy cut-off was set to 500 eV. The supercell applied to model the graphene-metal interface was constructed from a slab of 13 layers of metal atoms with a graphene sheet adsorbed at both sides and a vacuum region of approximately 14 Å. In optimizing the geometry, the positions (z-coordinates) of the carbon atoms as well as those of the top two layers of metal atoms were allowed to relax. In the total energy calculations and during the structural relaxations the **k**-meshes for sampling the supercell Brillouin zone are chosen to be as dense as 24×24 and 12×12, respectively. The results of the spin and orbital resolved calculations are shown in *Figure* 5.9.

Similar to the ARPES results, the DFT calculation exhibits strong changes between the band structure of free-standing graphene and graphene/Ni(111). A shift by ≈ 2.4 eV to higher binding energies occurs for the π states around the Γ point. Simultaneously, a large band gap of ≈ 3 eV opens between the π and π^* and fully distorts the Dirac cone. In this band gap several new interface states appear, labeled as I_{1-4} in *Figure* 5.9. I_{1-4} are located around the K point below or close to the Fermi level. The localization below the Fermi level leads to a partly occupation. Further, an interface state I_5 appears at 3 eV above the Fermi energy around the M point. This interface state is the origin of the second absorption signature in NEXAFS spectra at 287.1 eV photon energy (see *Figure* 5.7). Thus this interface state exists far away from the Fermi energy and is not relevant for the physical bonding mechanism and transport effects.

The interface states I_1 appears around 3 eV binding energy and can be interpreted as the π character content of the in that range mainly d created hybridization bands.

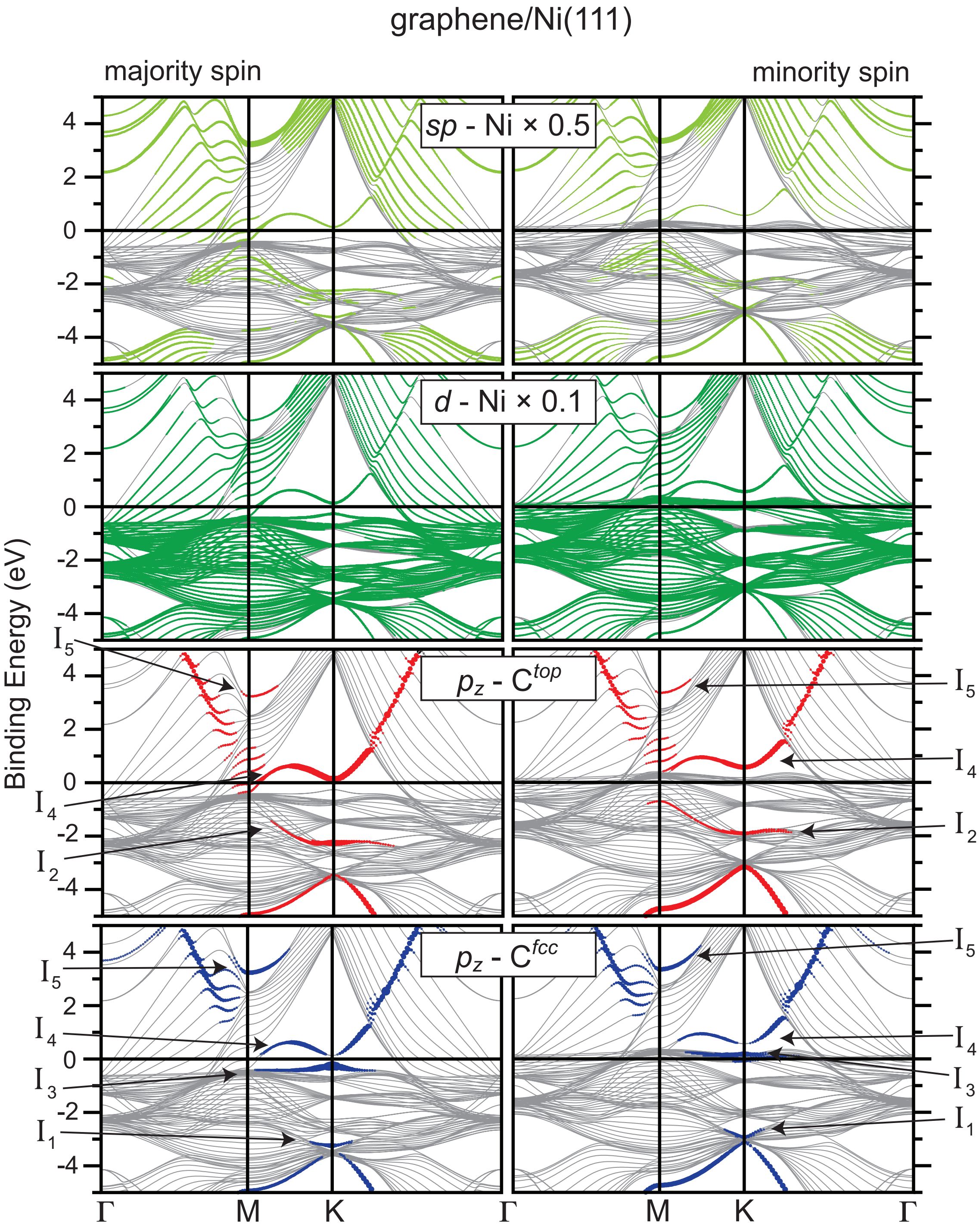

Figure 5.9: Results of the spin resolved DFT calculations. The width of the colored bands marks the strange of characters, respectively. It emerge several new interface states, labeled as I_{1-5}. A huge band gap appears between the π and π^* band of around 3 eV.

state	binding energy (eV)	
	spin ↑	spin ↓
I_5	−3.20	−3.32
I_4	−0.12	−0.55
I_3	0.28	−0.16
I_2	2.28	1.93
I_1	3.27	2.93

Table 5.1: This table summarizes the binding energies of the spin resolved interface states in the graphene/Ni(111).

The π content vanishes towards lower binding energies. This interface states belongs to the on-top sublattice of the graphene layer and are fully occupied for both spin species. The new interface state I_2 exists in the middle of the band gap of the graphene π band structure and belongs to the C^{fcc} sublattice. Both interface states $I_{1,2}$ are fully occupied because they occur below the Fermi level.

The most interesting hybridization effect is the occurrence of interface states I_3 at the Fermi level affecting transport phenomena and induced magnetic moment. This state has different binding energies for the spin-up states $I_3^\uparrow$ and spin-down states $I_3^\downarrow$. This energy difference becomes relevant because of the difference in occupation. $I_3^\uparrow$ is centered at 400 meV binding energy and nearly fully occupied. The fact that this state belongs to the spin up states means that the resulting magnetic moment is aligned parallel to the magnetic moment of Ni(111) substrate. In contrast to the occupation of the $I_3^\uparrow$ interface state, $I_3^\downarrow$ is nearly empty because of the centering above the Fermi level at 100 meV binding energy (see *Figures* 5.9). Therefore, the magnetic moment of the interface $I_3^\downarrow$ can not compensate the magnetic moment of $I_3^\uparrow$. Finally, a net magnetic moment is proposed from the DFT calculation aligned parallel to the magnetic moment of the Ni substrate. This prediction of an induced magnetic moment to the graphene π states is very well demonstrated in XCMD experiments, presented in *Section* 5.8.

In summary, the DFT calculations show a strong distortion of the π band which leads to gap opening of several eV. In this gap, new interface states emerge, originating from different sublattices. In the ARPES spectra, the observed n-doping is realized by the occupation of the interface states I_{1-3} and stops with the partly filled $I_3^\uparrow$ and $I_3^\downarrow$. A difference in the occupation magnitude of $I_3^\uparrow$ and $I_3^\downarrow$ explains an induced net magnetic moment to the graphene π states.

5.7 Discussion

The aim of this section is to summarize the results of the graphene/Ni(111) experiments and calculations, to arrive at a complete picture of the electronic band structure. While the absorption of graphene on Ni(111), several effects occur simultaneously complicating a description of the binding mechanism.

As explained in *Section* 5.1, one of sublattices is located on top of the Ni surface atoms and the other one on the fcc hollow site. An asymmetric potential arise from the different absorption sites of both sublattices creating a band gap at the K point between the π and the π^* band [161–163]. By affecting the photoemission final states of different sublattices reversely the asymmetric potential leads to the lost of the destructive interference from the emitted electrons from different sublattices in the second Brillouin zone [141]. In 2007 Bostwick *et al.* found a relation to assign the π band intensity ration between the first and the second Brillouin zone to a certain band gap size [146]. In the case of graphene/Ni(111) follows a energy gap size of about $\Delta E = 600\,\mathrm{meV}$ what cannot be observed. The occurring band gap is at least 2.6 eV as the energy difference between the π band and the strong intensity at Fermi level around the K point. Therefore this asymmetric potential can not be the reason for the full size of the observed gap.

A further effect influencing the graphene band structure strongly is the hybridization of the π states with the Ni 3 d states. These electron systems have a significant real space overlap. Around the Γ point at the center of Brillouin zone the π states energetically fare away from the 3 d states bound up to 10 eV binding energy. This changes along Γ-K direction. Around the K point the π band touches the 3 d Ni bands and strong hybridization effects can be observed.

In the XPS spectra the C 1 s emission intensity occurs shifted to smaller binding energies, indicating an n-doping of the graphene layer consistent with the rigid shift of σ states to higher binding energies. Because of the strong downwards shift of the σ states by of 1 eV, a strong core level shift can be expected. The reason, why the C 1 s core level is shifted only by about 100 meV, is the energetic separation of interface states. If the doping level reaches the next higher interface state the Fermi level jumps by several hundred meV accompanied by only a small charge transfer. Therefore a small charge transfer leads to a large sift of the Fermi level.

DFT calculations clearly show that this n-doping proceeds from the occupation of the new interface states I_{1-3} in the band gap region between the π and the π^* bands. In *Figure* 5.10, the DFT results are plotted on top of the ARPES spectra, thereby the calculated band structure is aligned to the graphene π band and the graphene/Ni(111) hybridization structure. A misfit of the Fermi energies appears from theory and experiment by 150 meV. This can be explained by the limited number of layers, which was used in the DFT calculations and the van der Waals interaction which was not considered in calculations. Later calculations for the graphene/Al/Ni(111) system take this interaction into account leading to better fit of the theoretical and experimental Fermi levels (see *Figure* 6.14). The interface state I_2 fits very well to a prior unidentified intensity structure at the K point around 2 eV binding energy.

Furthermore the DFT calculation propose an interface state at the M point at 4 eV above the Fermi level. This interface state was found in NEXAFS spectra as a second component at the C 1 $s \rightarrow \pi^*$ absorption signal.

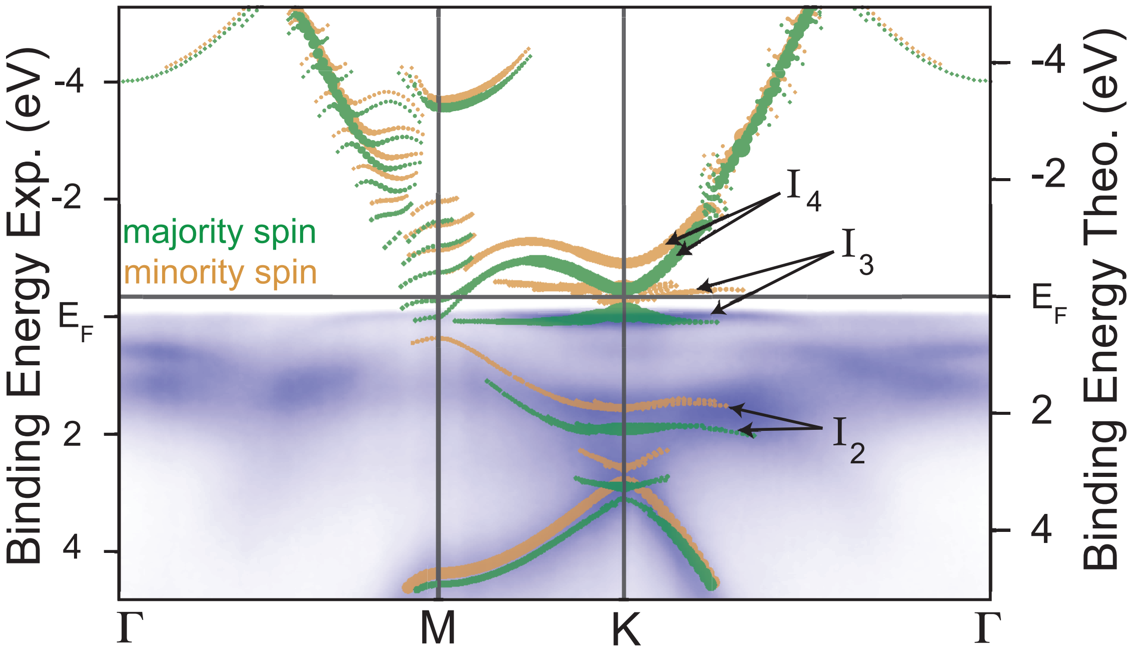

Figure 5.10: This graphic depicts the theoretical results projected on top of the ARPES emission spectra of graphene on Ni(111). Concerning the DFT calculations, the dot size marks the strength of the p character. The green and the orange dots represent the majority and minority band structure, respectively.

The XMCD measurements show a considerable induced magnetic moment on the graphene. This effect is explained by the partial occupation of the majority interface state $I_3^{\uparrow}$ and minority interface state $I_3^{\downarrow}$ appearing very close to the Fermi level. From the fact that the measured magnetic moment is aligned parallel to the magnetic moment of the Ni layer, it can be concluded that the occupation of the $I_3^{\uparrow}$ dominates the occupation of both interface states, confirming the results of the calculation, showing that the $I_3^{\uparrow}$ emerge at higher binding energies. Furthermore, in the projection of the DFT calculations on top of the APRES spectra using the π band structure as a reference, the interface $I_3^{\uparrow}$ occurs almost below the experimental located Fermi level, in contrast to $I_3^{\downarrow}$, which occurs almost unoccupied in comparison to experimental Fermi energy.

All in all, what happens while the graphene grows on top of Ni(111)? The π

electron system overlaps with the 3 *d* states of the Ni substrate. This leads to a band gap opening because of the no-crossing rule of interacting bands. The absorption of the graphene layer on Ni(111) creates five new interface states, which belongs to the graphene and the Ni electron system. The difference of the electron negativity generates an n-doping by the occupation from the interface states I_{1-3} and stops with the partly filled $\mathrm{I}_3^{\uparrow}$ and $\mathrm{I}_3^{\downarrow}$. This charge transfer from Ni to graphene affects a chemical shift of the C 1 *s* core-level to smaller binding energy. Further, a magnetic moment arises via different occupation magnitudes of $\mathrm{I}_3^{\uparrow}$ and $\mathrm{I}_3^{\downarrow}$, which are populated by different spin species. Hence, the spin magnetic moments do not compensate each other and ends in a XMCD contrast in absorption experiments.

One of the favorite application for the system graphene/Ni(111) is to realize a spin filter device suggested by Karpan *et al.* [12, 67], which principles are described in *Section* 2.3.2. In that model used by Karpan, the band structure of free-standing graphene was assumed. The suggested spin filter is based on the meeting of the spin minority Ni 3 *d* with graphene Dirac cone at Fermi level around the K point. That assumption fails in reality because of a huge gap appearing between the π and π^* bands. Close to the Fermi level, two new interface states occur around the K point. If the interface states are not completely occupied, they can participate in transport processes. Comparing the DFT and ARPES results, mainly the $\mathrm{I}_3^{\uparrow}$ majority spin states of graphene are partly occupied as supported by the XMCD data. In this case the spin selection at K point runs with the opposite spin species as proposed by Karpan. The transport process in the Brillouin zone is located at the K point. Therefore, the first graphene layer acts as a majority-spin injector.

The goal of future experiments should be to control the occupation of the $\mathrm{I}_3^{\uparrow}$, $\mathrm{I}_3^{\downarrow}$, and π^* states. Both interface states are occupied by opposite spin species. For varied doping levels, it should be possible to tune the degree of spin polarization of the graphene band structure at the Fermi level. If both interface states are completely occupied, it would be possible to shift the π^* band to the Fermi level with further n-doping. In that case, the conditions of Karpan's assumed model are similar and the graphene/Ni(111) interface acts as a minority injector.

Chapter 6

Intercalation of metals Fe and Al underneath graphene on Ni(111)

6.1 Intercalation of Fe

Thin layers of Fe have attracted the interests of scientist for a long time due to the occurrence of magnetic shape anisotropy and crystallographic structure effects and, more importantly, because of the role they play in the giant magnetoresistive effect (GMR), for the discovery of which Grünberg and Fert received the Nobel Prize in Physics in 2007 [65, 66] and, more importantly, in the field of magneto nanostructure research [164]. Magnetic anisotropy describes the different amount of work necessary to magnetize a sample in a specific direction. This effect relates to the crystallographic structure and the shape of the sample. If a sample has a very small size in one or two dimensions, it is easier to magnetize the sample along the large-sized dimension; this effect is called shape anisotropy, a very important property in thin layers. Thin Fe films grown on Ni(111) and on Cu(111) appear to grow in the *fcc* γ-phase structure, in contrast to bulk Fe which occurs in the *bcc* structure [165], the substrate imprinting its structure to the film, as it were. As a consequence of the shape anisotropy and the crystallographic structure in the thickness range from 1 - 4 ML, Fe shows a ferromagnetic behavior and is non-ferromagnetic in the range from 4 - 11 ML [166–173].

Fe exhibits an increased magnetic moment of the $3\,d$ states compared to Ni, which is likely to influence the induced magnetic moment of the graphene layer discussed in *Chapter* 5. If graphene is used as a protection layer in order to passivate the surface of ferromagnetic metals [123, 124] in future electronic devices, a deeper understanding of magnetic coupling is required. Furthermore, to intercalate Fe underneath graphene is a simple way to prepare a graphene/Fe interface (the growth of graphene on Fe(100) was recently demonstrated [174]). Fe films may also be used to implement the spin filter action in graphene devices discussed in detail above. The intercalation of Fe films underneath graphene is also interesting from another point of view. In Fe films deposited on a substrate, many structures of interest are metastable-island growth may have the upper hand over layer-by-layer growth, a thin film deposited under non-equilibrium conditions may break up upon annealing, etc.. Such processes might be avoided by a protective graphene film which acts as a surfactant or stabilizing agent for higher coverages.

The Fe intercalant is supposed to be a perturbation of the pristine graphene on Ni(111) system. Therefore the system graphene/Fe/Ni(111) must be discussed in relation to the graphene/Ni(111) system.

6.1.1 Crystallographic Structure and Stabilization of Fe in the γ-fcc Phase

Figure 6.1 shows the LEED images of (a) graphene/Ni(111) and (b) graphene on 1 ML Fe(111)/Ni(111). The absence of any remarkable changes, except for a considerable sharpening of the diffraction spots, demonstrates that Fe is intercalated in a (1×1) structure underneath graphene. After intercalation the three-fold symmetry of the system is preserved as deduced from the LEED pattern. Considering the possible crystallographic structures, Fe atoms below the graphene layer can be placed either in the *fcc* or in the *hcp* hollow sites above the Ni(111) surface. According to the symmetry of the system obtained after Fe intercalation (also confirmed by DFT calculations discussed in *Section* 6.1.5), the two most energetically favorable configurations of the graphene layer and the iron atoms in the graphene/Fe/Ni(111) system are: (i) the Fe atom is placed in the *hcp* hollow site and the carbon atoms are in the *top-hcp* configuration with respect to Ni(111); (ii) the Fe atom is placed in the *fcc* hollow site and the carbon atoms are in the *top-fcc* configuration with respect to Ni(111) [126, 134, 142, 144]. The latter arrangement is shown in *Figure* 6.1 (d) and presents the case of the *top-hcp* configuration of the graphene layer on a metallic surface where one of the carbon atoms in the graphene unit cell is placed above the interface metal atom (Fe) and the second one is in the *hcp* position with respect to the metal. The interaction between the graphene layer and the underlying Fe is stronger compared to graphene/Ni(111) as discussed at length on the basis of DFT calculations in section 6.1.5. This is reflected in the shorter graphene-Fe interface distance: atoms C^{top} and C^{hcp} are placed at 2.114 Å and 2.089 Å above the Fe layer, respectively, as obtained from DFT calculations. Differences in energy between *top-hcp* and *top-fcc* configuration clarify that the third metal layer is also involved in the binding mechanism.

6.1.2 Core Level Spectroscopy

The intercalation process was monitored by means of core level spectroscopy of Fe on top and underneath graphene(see *Figure* 6.2). Deposition of Fe reduces the C 1 *s* intensity (not shown here). After the intercalation, the Fe atoms are inserted underneath graphene. Hence the C 1 *s* intensity has to recover to the value characteristic for graphene on Ni(111); we will see a similar example in the case of intercalated aluminium in *Chapter* 6.2. The intensity of the Fe core levels such as Fe 3 *p* shows the opposite behavior. The C 1 *s* peak for the Fe/graphene/Ni(111) system occurs at

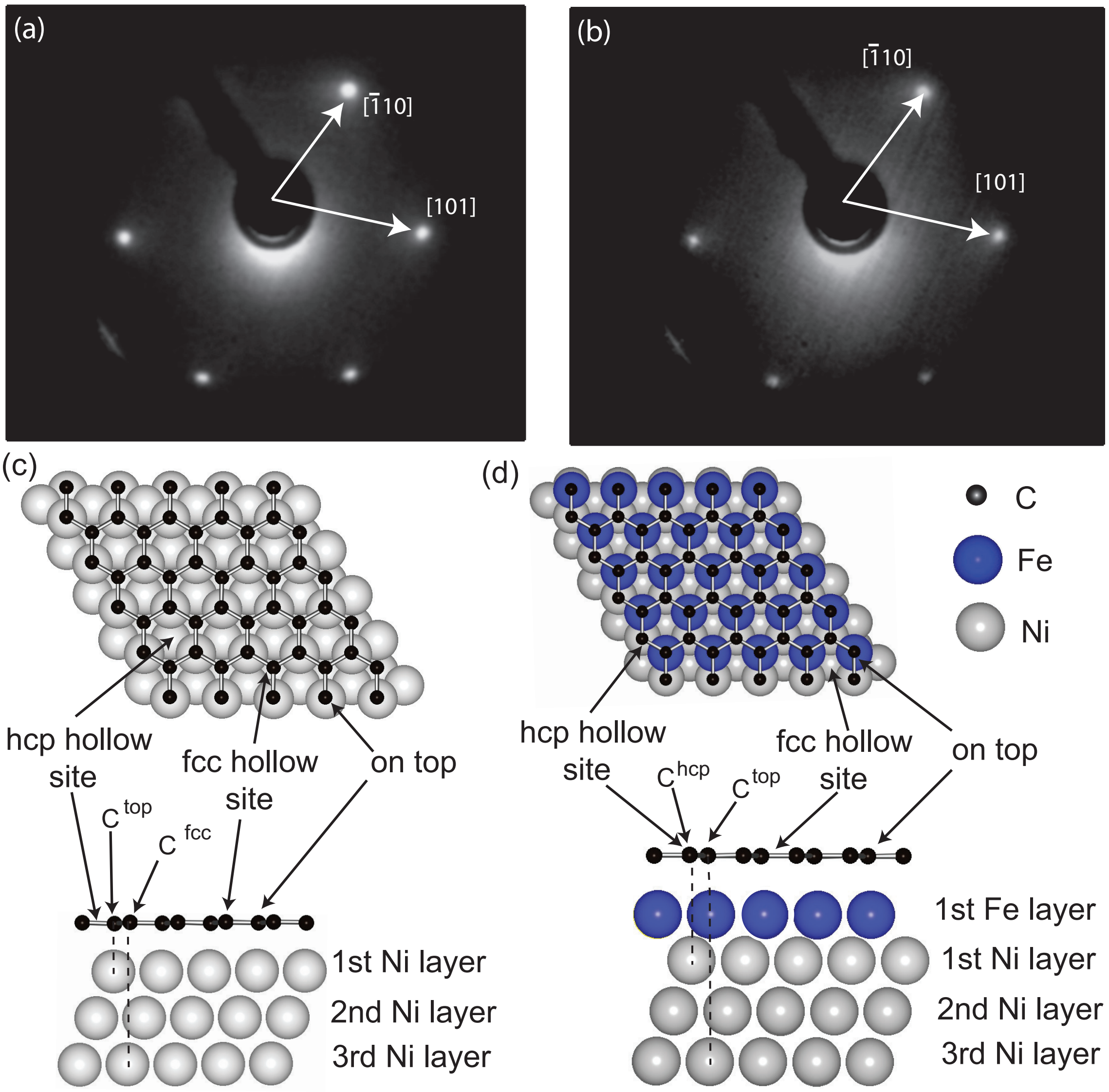

Figure 6.1: LEED pattern and atomic structure model of graphene/Ni(111) and graphene/1 Fe ML/Ni(111): (a) and (b) show the LEED diffraction patterns of graphene/Ni(111) and graphene/1 ML Fe/Ni(111), recorded at an electron energy of 120 eV and 125 eV, respectively. (c) and (d) show one favorable atomic structure for both systems supported by DFT calculations discussed below.

285.3 eV binding energy. After the annealing step the peak shifts around 200 meV to higher binding energies. One explanation is that in the Fe/graphene/Ni(111) configuration, charge carriers are transferred from the Fe layer and from the Ni substrate to the graphene layer. In the case of graphene/Fe/Ni(111) electron transfer occurs only from the Fe side to the graphene. These arguments are supported by the binding energy of the Fe $2p_{3/2}$ and $2p_{1/2}$ core levels before and after the intercalation step. In the Fe/graphene/Ni(111) configuration, the Fe $2p$ core level occurs at 706.8 eV and 720.1 eV binding energy. During the intercalation process the $2p$ core

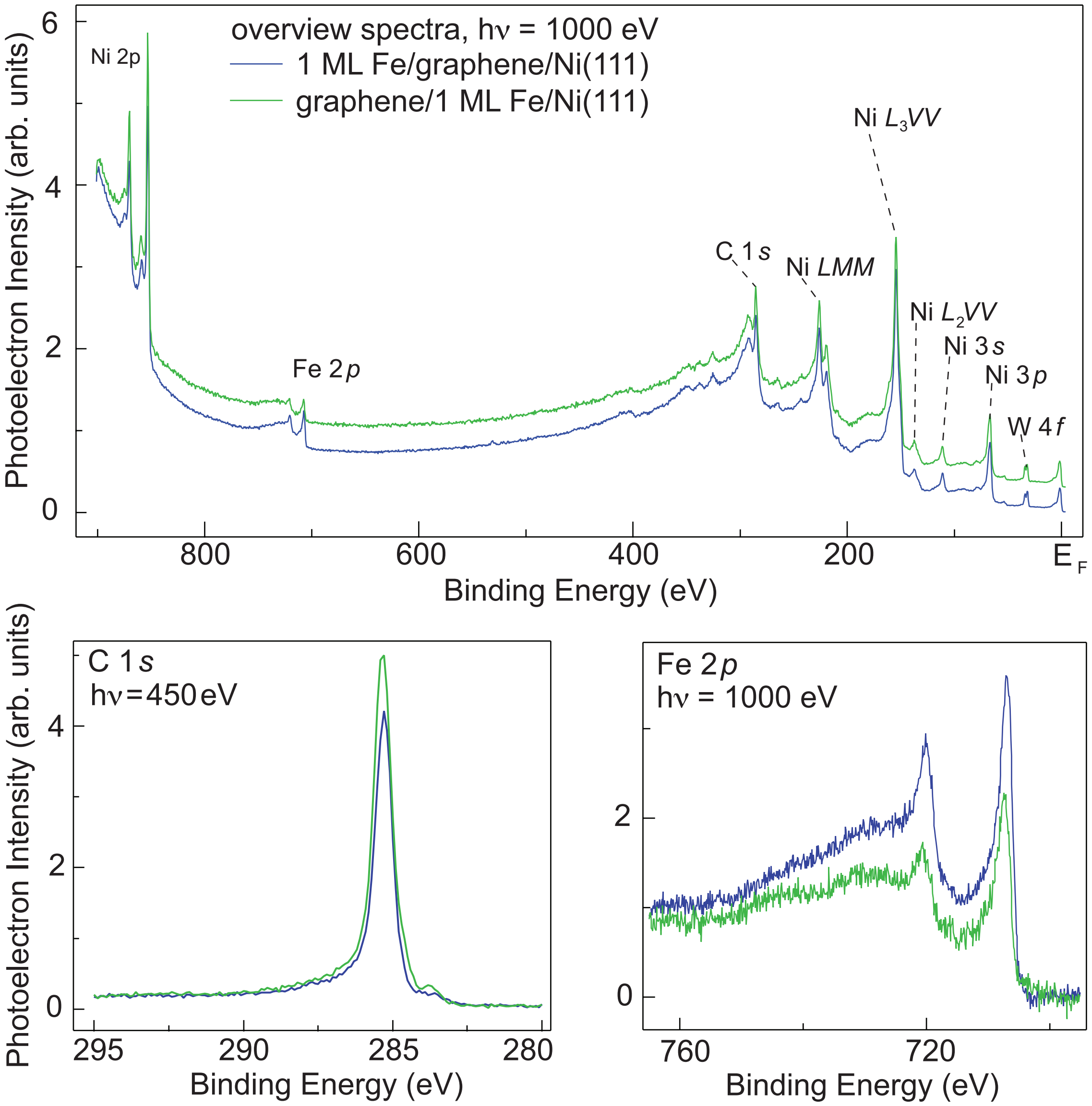

Figure 6.2: Core level spectra before and after intercalation of Fe into graphene/Ni(111), taken at photon energy of 450 eV and 1000 eV. The intercalation process is monitored by the changes of core level intensity.

levels are shifted by 500 meV to higher binding energies. The charge transfer from the Fe layer to the graphene is increased because of the missing of a donor electron spender. Furthermore the Fe layer is now in contact with the Ni substrate. Ni has a slightly higher electronegativity, so Ni substrate changes from donor to acceptor.

After the thermal intercalation step, a small peak occurs in the C 1*s* line, which is shifted by ≈1.5 eV to lower binding energies. Such a peak is often observed in graphene/Ni(111) shifted by ≈0.6 eV to smaller binding energies and has been interpreted as emission from a Ni carbide phase [139]. The large difference to the observed value in graphene on Fe/Ni(111) leads to the assignment to an iron carbide phase and the low intensity of the additional peak suggests that this phase does not strongly disrupt the intercalated phase. The carbide phase probably occurs as a result of thermal stress during the intercalation process.

6.1.3 ARPES Results

From a comparison of the electronic valence band structures of graphene on Ni(111) and graphene on Fe/Ni(111), a similar bonding behavior is apparent. *Figure* 6.3 presents the photoemission spectra of both systems along the high symmetry directions Γ-M-K-Γ. The bottom of the π bands are shifted downwards by about 2.4 eV to higher binding energies compared to free-standing graphene [13]. At the K points, no Dirac cones appear, and the π bands do not extend closer than 2.8 eV, towards the Fermi level in both systems. The σ bands are rigidly shifted downwards by about 1 eV to higher binding energies. A similar binding mechanism as in graphene/Ni(111) means that, a strong hybridization between the π states and the $3\,d$ states of the substrate occurs, accompanied by n-doping of the graphene layer as described in *Chapter* 5.3. Moreover, in the valence band structure of graphene/1 ML Fe/Ni(111) a triangular-shaped intensity structure with a clear minimum at the center occurs, equivalent to the graphene/Ni(111) system at the K point. In case of graphene/Ni(111) this structure was assigned to the creation of new interface states driven by the hybridization between the $3\,d$ Ni states and the graphene π states. Along the almost vertical branches the character of states changes continuously from π to $3\,d$ in the direction to smaller binding energies. Following from the similarity between graphene on Ni(111) and on Fe/Ni(111) a transition from π to $3\,d$ Fe character is expectable Also, the flat intensity distribution around the K point at the Fermi energy is preserved after intercalation. This intensity was assigned in case of graphene/Ni(111) to the creation of the interface state I_3 (see *Chapter* 5).

In the range between 2.5 eV binding energy and the Fermi level, the shallow $3\,d$ bands of the substrate are visible. These also show almost no changes before and after intercalation of 1 ML Fe. This can be explained by the almost similar electronic properties of Fe and Ni. When we consider the band structure of Fe and Ni, both in the fcc phase (e.g. as shown in *Figure* 11 in [164] , we note that they are similar except for the band filling (expected from the higher number of d electrons in the latter) and the spin splitting). Thus we may expect that in a single intercalated layer in which the Fe assumes the structure and lattice constants of the substrate, these similarities will become even stronger.

In order to detect possible changes away from the high symmetry directions, *Figure* 6.4 presents constant energy cuts at different binding energies. Small differences occur only at the Fermi level. The almost circular structure around the Γ point indicated by dashed lines in constant energy cuts at Fermi level shows a decreased intensity and is slightly expanded. Such effects can arise from a small doping because these states belong to a very flat band. Another reason might be that this feature is not present in the Fe adlayer, and is reduced in the Fe intercalated layer

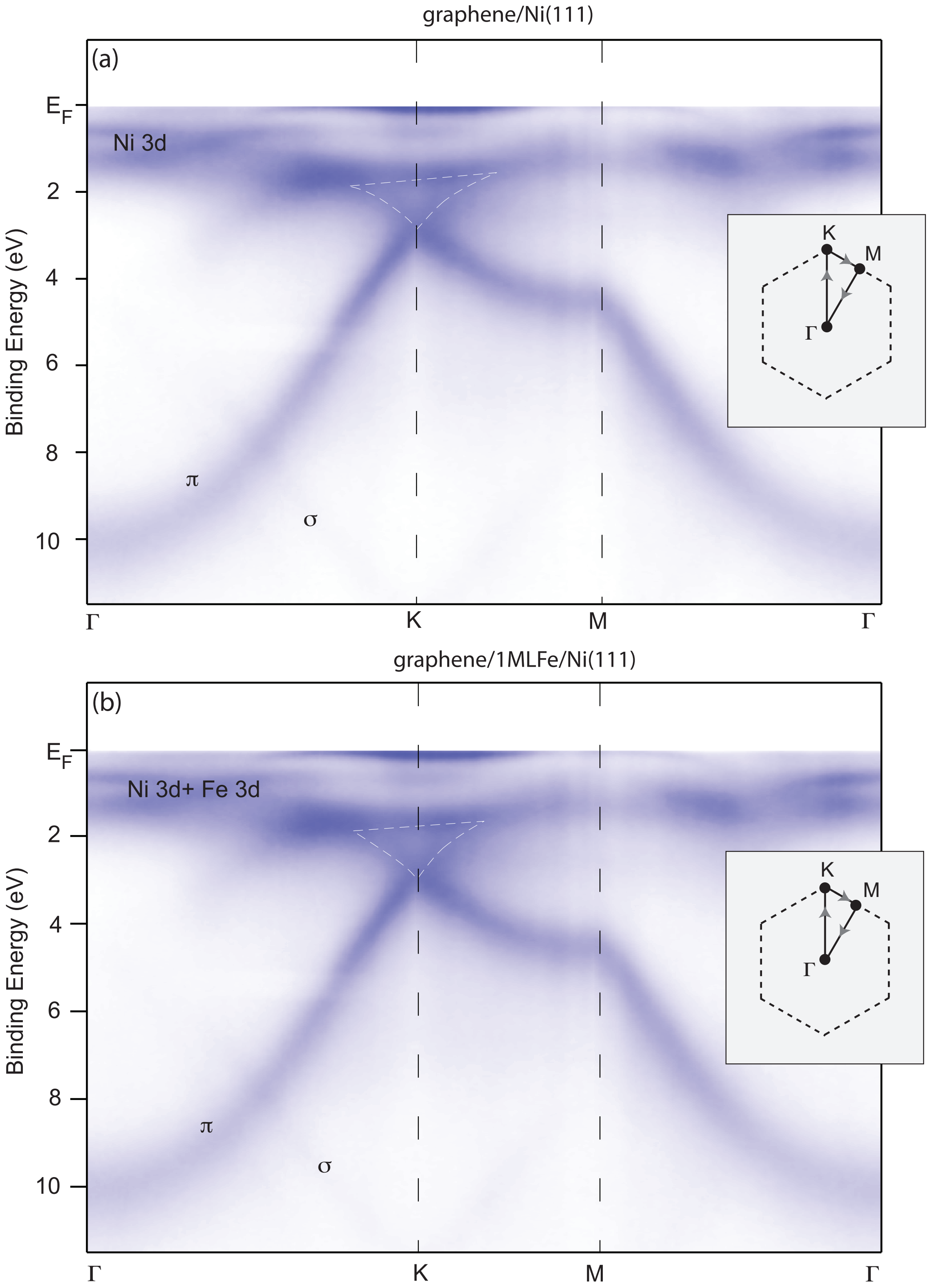

Figure 6.3: Band structure of graphene on Ni(111) and on 1 ML Fe/Ni(111): In both systems, the π *band shifts downwards and is distorted in contrast to the* σ *band that is only shifted. The broad intensity distribution between 2 eV binding energy and the Fermi level is assigned to the 3d states of Ni in (a) and Fe+Ni in (b).*

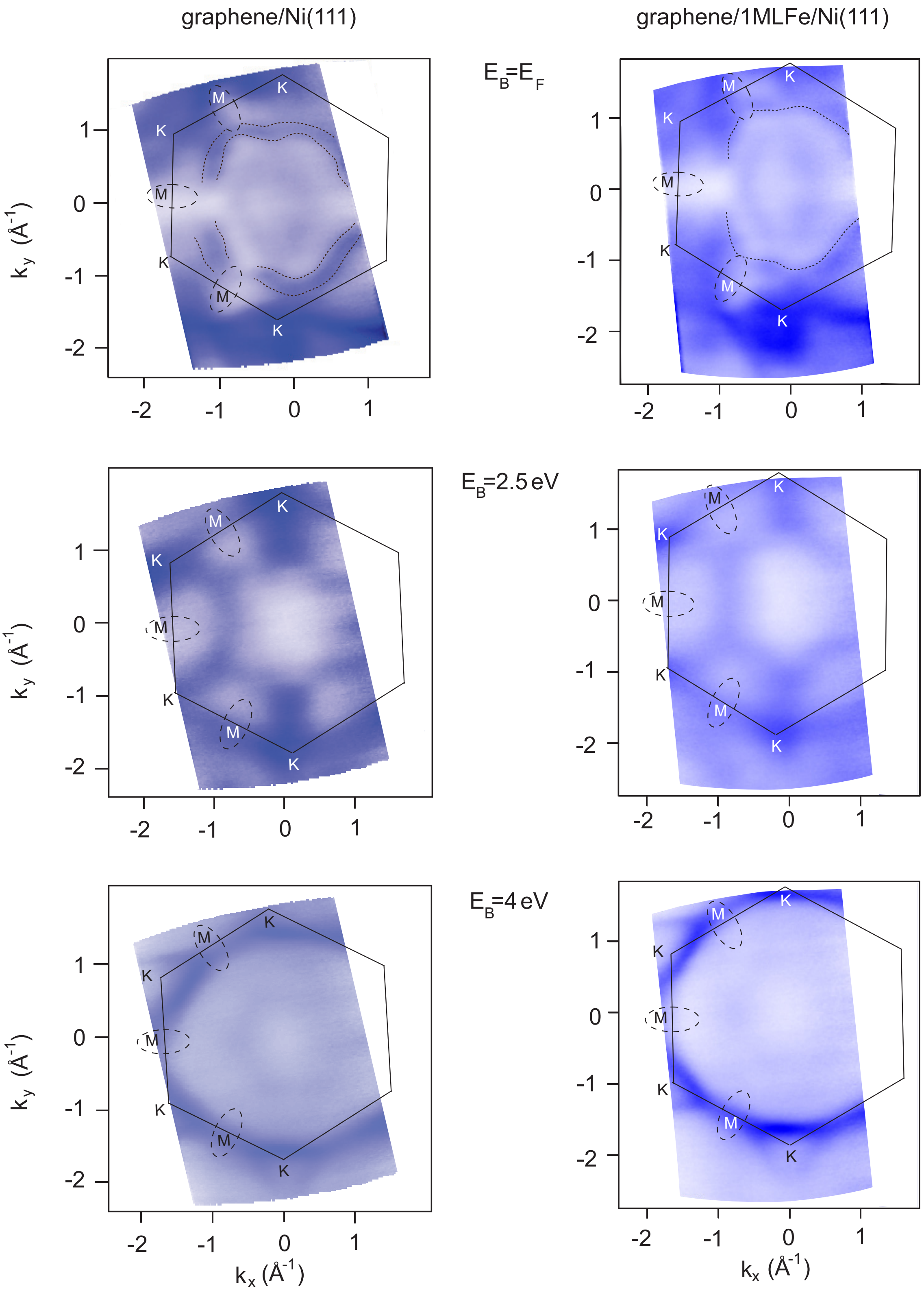

Figure 6.4: Constant energies cuts at the Fermi level, 2.5 eV and 4 eV binding energy for graphene/Ni(111) and graphene/Fe/Ni(111): In case of 2.5 eV and 4 eV binding energy no significant changes between both system are visible. Small differences occur close to Fermi level dash lines marks

because of the attenuation of the Ni substrate signal. By comparing this structure with Fermi surface projection of Ni to the (111) surface these states were interpreted as Ni minority states (see *Figure* 5.6 [67].

In constant energy cuts in *Figure* 6.4 at 4 eV binding energy of graphene/Ni(111) and graphene/1 ML Fe/Ni(111) the π bands has an almost circular shape, with additional triangles at the K points. Such a structure is known from free-standing graphene at smaller binding energies [13]. Thus we can conclude that the hybridization does not influence the structure of the π bands at this energy range and the π states exhibit pure π character.

6.1.4 X-Ray Absorption Spectroscopy

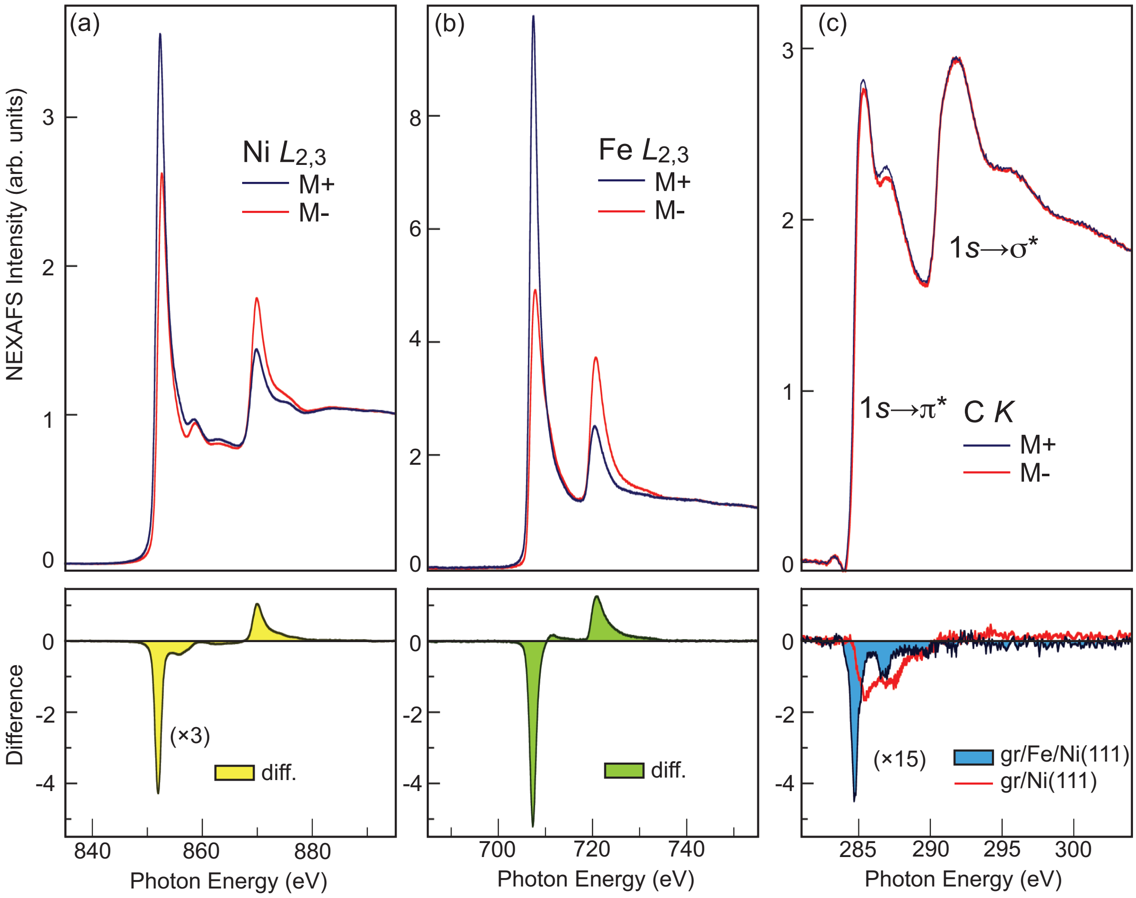

Figure 6.5: Absorption spectra for circular polarized light and the resulting XMCD response of graphene/1 ML Fe/Ni(111): Ni shows a small increased magnetic moment compare to the bulk value. From the absorption spectra of Fe follows a reduction compared to already published fcc stabilized Fe. In case of C atoms the magnetic contrast in the absorption spectra, shown in (c),is increased by a factor of 2.7 in case of graphene/1 ML Fe/Ni(111) compared to graphene/Ni(111).

The magnetic properties of the graphene layer on the ferromagnetic Ni(111) surface were discussed in detail in *Chapter* 5.8 (see also [126, 138]) and it was demonstrated that a strong hybridization of the graphene π and Ni $3\,d$ states leads to the appearance of several new interface states. Differences in the spin-dependent occupation of these create an induced magnetic moment in the carbon atoms with a value of 0.05 - 0.1 μ_B per carbon atom. The respective reduction of the magnetic moment of the Ni interface atoms, compared to the bulk value, was predicted and observed in these experiments [126, 134, 138]. The results of the investigation of the magnetic properties of the graphene/1 ML Fe(111)/Ni(111) system are summarized in *Figure* 6.5, where the absorption spectra measured with circularly polarized light for two opposite magnetization directions of the sample and the corresponding XMCD contrasts are shown in the lower panels, respectively, for the (a) Ni $L_{2,3}$, (b) Fe $L_{2,3}$, and (c) C K absorption thresholds. The XMCD spectrum collected at the Ni $L_{2,3}$ edge in the TEY mode is in perfect agreement with previously published data [153, 175, 176]. The bulk values of the spin and orbital magnetic moments $\mu_S = 0.69\,\mu_B$ and μ_L=0.07 μ_B of Ni calculated from the spectra on the basis of sum rules are in very good agreement with previously published experimental values [153, 154] as well as with the spin-magnetic moment $\mu_S = 0.67\,\mu_B$ calculated for the graphene/Ni(111) system [134]. The Fe $L_{2,3}$ XMCD spectrum is in good agreement with previously presented data for fcc Fe [177, 178]. The spin and orbital magnetic moments can be estimated from these data assuming the number of holes in the iron layer in the graphene/1 ML Fe(111)/Ni(111) system to be $n_h = 3.7$ per atom [179]. This means an electron transfer of $0.15\,e^-$ from Fe to Ni [180] and the same value from Fe to the graphene layer, based on bulk Fe with $n_h = 3.4$. The DFT calculation in the next section gives a value of n_h=3.69 for the Fe interlayer. This number leads to $\mu_S = 2.56\pm0.1\,\mu_B$ and $\mu_L = 0.31\pm\ 0.05\,\mu_B$ for the spin and orbital magnetic moments of Fe atoms in the intercalated layer which are in very good agreement with the value of the spin magnetic moment 2.469 μ_B for Fe obtained in calculations for graphene/1 ML Fe(111)/Ni(111). The relatively large uncertainty in the value of the magnetic moment extracted from experiment arises mainly from the estimation of the number of Fe $3\,d$ holes and from the uncertainty in the degree of circular polarization of light. The C K-edge XMCD spectrum of graphene/1 ML Fe(111)/Ni(111) is strongly modified compared to the one measured for the graphene/Ni(111) system. The most important observation is the increase of the magnetic contrast at the C K edge by a factor of ≈ 2.7. As in the graphene/Ni(111) data, the relatively strong XMCD contrast is detected for C 1 s$\rightarrow$ π^* transitions whereas almost no variation of the absorption signal upon magnetization reversal is observed for the C 1 s$\rightarrow$ σ^* transitions.

These observations are explained well by the theoretically predicted strong hybridization of the out-of-plane graphene π and Fe $3\,d$ states and the existence of the relatively weak hybridization between the in-plane graphene σ and Fe $3\,d$ states, similar to graphene on Ni(111). The C K-edge XAS spectrum of the graphene on 1 ML Fe(111)/Ni(111) system in the energy range corresponding to the $1\,s \rightarrow \pi^*$ transition consists of two peaks which can be assigned, similar to the graphene/Ni(111) system, to transitions of the $1\,s$ electron into the interface states resulting from the hybridization of C p_z orbitals of the graphene layer and Fe $3\,d$ orbitals. These interface states clearly occur in the DFT calculations presented in *Figure* 6.6.

XMCD spectra measured at the C K-edge provide information on the orbital moment only. From the negative sign of the XMCD signal one can conclude that the average orbital moment of carbon atoms of the graphene layer is aligned parallel to both the spin and orbital moments of the substrate layer. Note that the orientation of individual spin and orbital moments of Fe and C at different sites cannot be determined from the experimental XMCD data. On the basis of the comparison of the dichroic signals measured at the C K-edge for the graphene/Ni(111) and graphene/1 ML Fe(111)/Ni(111) systems, an increase of the spin magnetic moment on the carbon atoms up to $\sim$0.2 - 0.25 μ_B can be estimated. The calculation gives values of magnetic moments of 0.050 μ_B and 0.039 μ_B for $\mathrm{C}^{\mathrm{top}}$ atom and $\mathrm{C}^{\mathrm{hcp}}$ atom, respectively. The origin of large discrepancies between theoretical and experimental values are assigned to the different positions of the Fermi level, which strongly influences the occupation of the interface state I_3.

6.1.5 Comparison of DFT Calculation Results for Graphene on Ni(111) and on Fe/Ni(111)

As in the graphene/Ni(111) case, DFT calculations for the graphene/1 ML Fe/Ni(111) system were performed by Dr. E. Voloshina (FU Berlin). In these studies the electronic and structural properties of the graphene-substrate system are obtained using the Perdew-Burke-Ernzerhof (PBE) functional [157]. For solving the resulting Kohn-Sham equation, the Vienna Ab initio Simulation Package (VASP) [158, 159] was used, with projector augmented wave basis sets [160]. The plane wave kinetic energy cutoff was set to 500 eV. The supercell used to model the graphene-metal interface was constructed from a slab of 13 layers of metal atoms with a graphene sheet adsorbed at both sides and a vacuum region of approximately 14 Å. To optimize the geometry, the positions (z-coordinates) of the carbon atoms as well as those of the top two layers of metal atoms were allowed to relax. For the total energy calculations and during the structural relaxations, the k-meshes for sampling the supercell Brillouin zone were chosen with of density of 24 × 24 and 12 × 12, respectively. The detailed results of calculations are presented in *Figure* 6.6 and 6.7.

Starting with a comparison of graphene/Ni(111) and graphene/1 ML Fe/ Ni(111), the majority spin bands are almost identical in both systems. The main difference is that two new quantum well states at 1.47 eV and 0.5 eV above the Fermi level around the K point appear in the minority spin bands, labeled with I_{I} and I_{II} in *Figure* 6.7. Such interface states are well known in thin metal layers [181] created by potential barriers perpendicular to the thin layer. These I_{I} and I_{II} states originate from the $3\,d_{z^2}$ and the $3\,d_{xz,yz}$ orbitals of the Fe layer. The occurrence above the Fermi level explains that the ARPES spectra are not affected because ARPES experiments probe only the occupied states.

Due to the high similarity of both systems, no significant changes in the binding mechanism can be expected. This is strongly supported by the ARPES results and

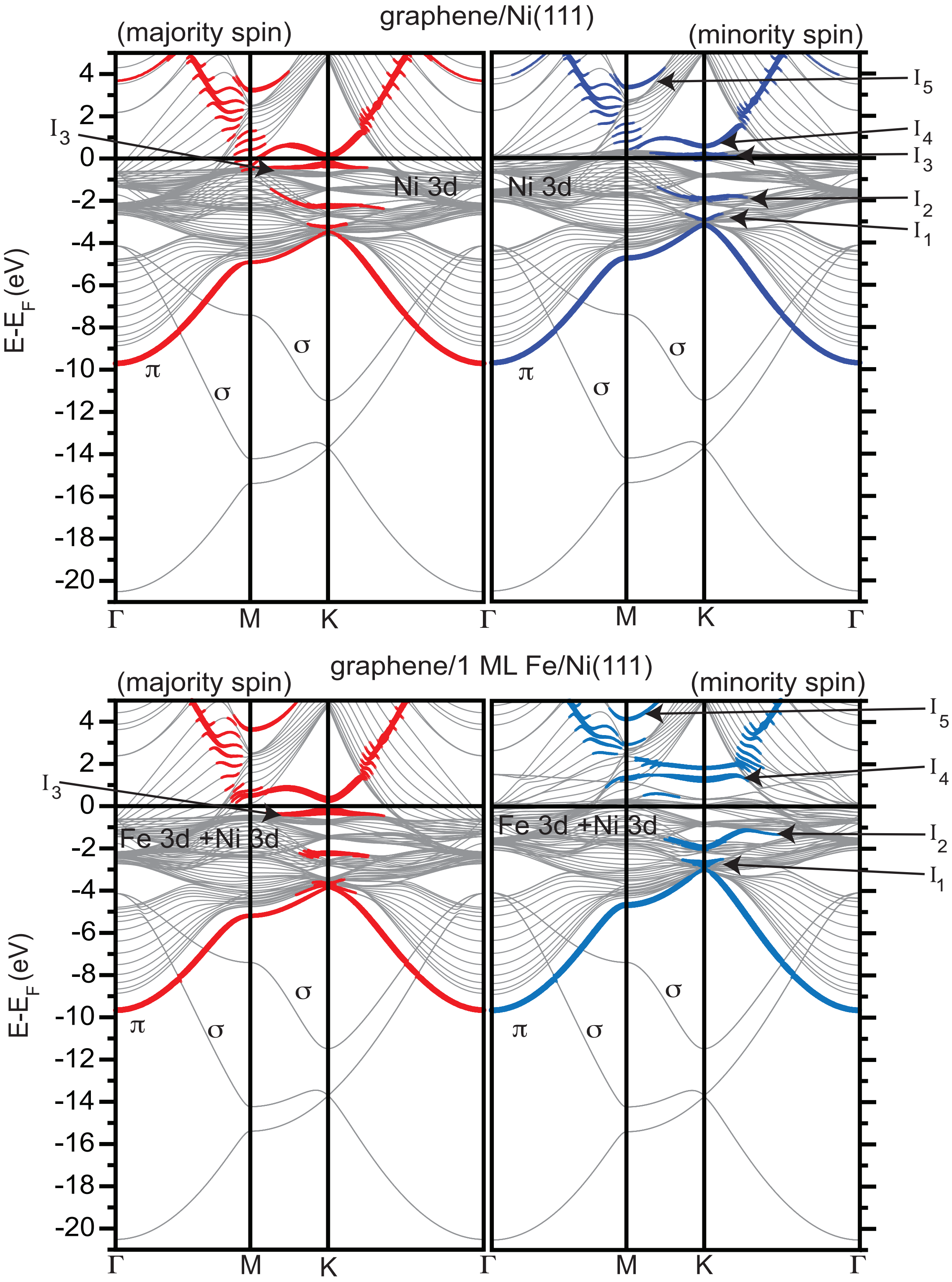

Figure 6.6: The primary valence band structure of the graphene and 3 d substrate states is preserved. Changes occur at the interface states mainly for I_4 of the minority spin band structure. This state splits into two new states 1.47 eV and 0.5 eV above the Fermi level [142].

agrees very well with the shape of the π band structure in DFT calculations. The influence of the new quantum well state is restricted to the minority spin band, in a region close to the K point, and to the energy range above or at least close to the Fermi level. I_1 and I_2 appear similar to the graphene/Ni(111) system. Close to the Fermi level, $I_3^{\uparrow}$ occurs in the band shape as known from graphene/Ni(111). The small shift of $I_3^{\uparrow}$ to higher binding energies can be assigned to a difference of the n-doping effect which leads to a full occupation of $I_3^{\uparrow}$. The main changes are related to interface states $I_3^{\downarrow}$ and I_4, which hybridize strongly with the new quantum wells states $I_{\mathrm{I,II}}$ and together create two new interface states at 1.4 eV and 2 eV above the Fermi energy. The energy range where the two new interface states occur is far above the Fermi level and therefore the occupation probability is zero. This explains why the ARPES spectra do not reflect these differences in bonding mechanism. In comparison to graphene/Ni(111) where the magnetic moments from the minority and majority spin interface states partly compensate each other, in graphene/Fe/Ni(111) the minority spin is fully unoccupied, such that no compensation occurs. Therefore, DFT calculations predict an increased magnetic moment compared to graphene/Ni(111). The interface state I_5 occurs similar to graphene on Ni(111), because it is located at the M point and no changes occur.

At the lower left-hand side of *Figure* 6.7 the spin-resolved DFT results are projected on top of the ARPES band images, aligned to fit of the graphene π states (this leads to a misalignment of the Fermi levels of about 350 meV). Due to the almost perfect fit of the Fermi levels between the calculations and the ARPES measurements of the graphene/Al/Ni(111) system, the present misalignment can be assigned to the omission of van der Waals interaction, which was not included here, in contrast to the graphene/Al/Ni(111) system described in Chapter 7. In the projection in *Figure* 6.7 an energy split of the of the majority and minority band structure is clearly visible.

The calculated magnetic moments of the Fe layer for 1 ML Fe/Ni(111) are -0.28 μ_B and 2.622 μ_B for the $4\,s$ and the $3\,d$ states, respectively. Absorption of graphene on top changes the magnetic moment to -0.35 μ_B and 2.469 μ_B for the $4\,sp$ and $3\,d$, respectively, leading to a reduction of the total magnetic moment of the Fe layer. Further, the calculation shows an increased magnetic moment for the graphene layer of about -0.05 μ_B and 0.039 μ_B for the $\mathrm{C^{top}}$ and $\mathrm{C^{hcp}}$ sublattices, respectively, compared to the graphene/Ni(111) system with -0.019 μ_B for the $\mathrm{C^{top}}$ and 0.031 μ_B for the $\mathrm{C^{fcc}}$.

Interestingly, the DFT results of graphene/Ni(111) assign every interface state to a single sublattice in contrast to the interface states of graphene/Fe/Ni(111) which show contributions of both sublattices to the same interface states. It can be speculated that the potential difference is smaller in case of intercalated Fe and therefore both sublattices are more similar.

In summary, the modification and the increase of the XMCD contrast from graphene/Ni(111) to graphene/1 ML Fe(111)/Ni(111) can be explained by changing to a fully unoccupied interface state $I_3^{\downarrow}$ which belongs to the minority band structure in contrast to the fully occupied $I_3^{\uparrow}$ of the majority bands.

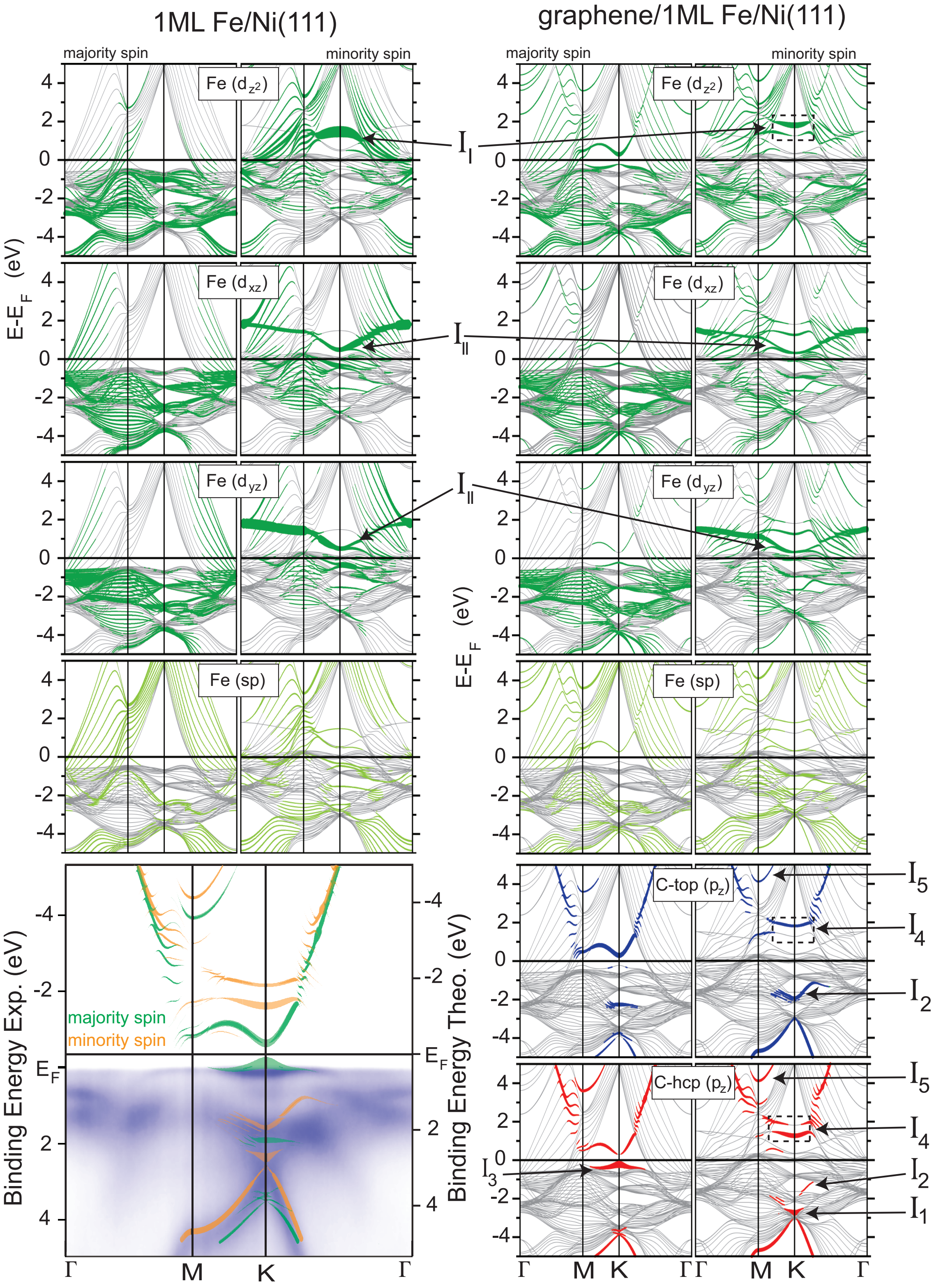

Figure 6.7: Results of the DFT calculations for the 1 ML Fe/Ni(111) substrate and the graphene/1 ML Fe/Ni(111): The occurrence of the interface state in the minority spin band of 1 ML Fe/Ni(111) substrate leads to a strong upwards shift of the interface state I_4.

6.1.6 Discussion

The most interesting effect regarding Fe intercalation is the similarity of the occupied band structure of graphene/Ni(111) and graphene/1 ML Fe/Ni(111). The only aspect questioning this conclusion is the observation of an increased magnetic moment, strongly supported by DFT calculations.

The key aspect for explaining the increased magnetic moment is the occurrence of two quantum wells states above the Fermi energy in the DFT calculations. These states occur only in the minority spin band structure of the metal substrate, such that only the minority graphene states are affected. The appearance of both states above the Fermi energy explains why ARPES spectra of the valence band structure are hardly unaffected upon Fe intercalation. Only $I_3^{\downarrow}$ lies in the k-space region of this quantum well state. The hybridization between the $I_3^{\downarrow}$ and the quantum well state at 1.47 eV leads to the creation of two new interface states. Both new states exist more than one 1 eV above the Fermi level and therefore they are unoccupied. In contrast, I_3 is slightly shifted downwards and fully occupied. The downward shift of I_3 and the completely unoccupied I_4 is the reason for the increased magnetic moment in graphene/1 ML Fe/Ni(111) compared to graphene on Ni(111). According to the assignment of I_3 to the majority band structure, the induced magnetic moment of the graphene layer is aligned parallel to the Ni magnetization. Note that DFT calculations assign the the interface states to both sublattices; rather, the interface states contain contributions from both sublattices. Therefore it can be speculated that the asymmetry of the sublattices is reduced after Fe intercalation.

In future experiments, doping be may used in order to find the maximum occupation of I_3 accompanied by a saturation of the induced magnetic moment. An interesting investigation would also be the intercalation of submonolayer Fe underneath graphene on Ni(111), with the aim of continuously tuning the magnetic moment.

Another interesting question is the maximum number of intercalated Fe layers which are stabilized in the fcc γ-phase. It can be expected that this number differs strongly from the 4 monolayer observed for Fe/Ni(111) [122, 166–168], because of the similar periodic potential from the Ni substrate below and the graphene adlayer layer on top, which is expected to act as a protecting and surfactant layer to increase the maximum thickness of fcc iron films.

From the side of future applications, it could be interesting to tune the magnetic moment induced into graphene. For the use of a graphene/Fe interface as spin filter device, a highly interesting result is the upwards shift of the minority spin interface state I_4 above the Fermi level. This changes the interface from an injector of minority and majority spin as concluded in the case of graphene/Ni(111) to a pure majority spin injector at the K point, contrary to the model proposed by Karpan *et al.* [67].

6.2 Intercalation of Al

One of the goals at present is to realize graphene-based applications, for example to create a graphene based Spin-FET introduced in *Section* 2.3.1.

For such a device it is desirable to prepare graphene electrically insulated on top of a ferromagnetic substrate. Therefore Al as intercalant was selected because of the strong affinity to oxidize and the insulating behavior of AlO_y. The idea of the preparation was to intercalate firstly 1 ML Al underneath graphene and subsequently expose it to O_2. The intercalation of O_2 should lead to an oxidation of the Al layer, creating an insulating layer between graphene and Ni(111). The intercalation of O underneath graphene has been successfully demonstrated in the case of graphene/Ru(0001) [182, 183].

6.2.1 Crystallographic Structure

The process of formation of the graphene/Al/Ni(111) intercalation system was controlled by LEED and core level PES in normal emission geometry. These results are compiled in *Figures* 6.8 (a), (b) and 6.9, respectively. As described in *Chapter* 5, growth of graphene on Ni(111) in a (1×1) structure leads to a sharp hexagon in the LEED pattern. Intercalation of 1 ML Al underneath graphene on Ni(111) leads to drastic changes in the LEED picture which is presented in *Figure* 6.8 (b). First, a clear (2×2) over structure with respect to the graphene/Ni(111) unit cell occur in the LEED pattern, indicating the formation of a structure with a new symmetry. Additionally, weak ring-shaped spots at rotation angles of $\approx 15^\circ$ away with respect to the main diffraction spots are visible around the original (1×1) spots from the graphene layer on Ni(111). A similar ring-shaped structure was observed earlier in [130, 184] for the graphene/Cu/Ni(111) system and was assigned to the existence of a misfit between the graphene layer and the underlying Cu layer, which results from a weak graphene-Cu bonding.

In the atomic model explored for graphene/Al/Ni(111) a fcc Al(111) monolayer is placed in the space between graphene and Ni(111) as shown in *Figure* 6.8 (c). There is only one possible arrangement for the aluminum atoms in the high-symmetry positions in such a system. A ball model of the graphene/Al/Ni(111) system obtained after structural optimization is shown in *Figure* 6.8 (c). The Al(111) lattice plane is rotated by 30° with respect to the graphene/Ni(111) lattice such that the Al atoms occupy all three different high-symmetry adsorption sites in the space between the graphene layer and the Ni(111) surface. They are noted in *Figure* 6.8 (c) with respect to the adsorption sites of the Ni(111) surface when occupying *fcc* (Al^{fcc}), *hcp* (Al^{hcp}), and *top* (Al^{top}) positions. In this case, the Al layer has a structure $(2\sqrt{3}/3 \times 2\sqrt{3}/3)R30^\circ$ with respect to graphene/Ni(111). The unit cell is labeled as "Al(1×1)" in *Figure* 6.8 (c).

The resulting supercell for the graphene/Al/Ni(111) system is marked as "gr(2×2)" in *Figure* 6.8(c). In this structure there are four different occupation sites for carbon atoms in the unit cell with respect to Al/Ni(111). They are labeled in *Figure* 6.8 (c) as $\mathrm{C}_{\mathrm{Ni}}^{top}$, $\mathrm{C}_{\mathrm{Ni}}^{fcc}$, $\mathrm{C}_{\mathrm{Al}}^{top}$, and $\mathrm{C}_{\mathrm{Al}}^{fcc}$, respectively. The distance between Al atoms

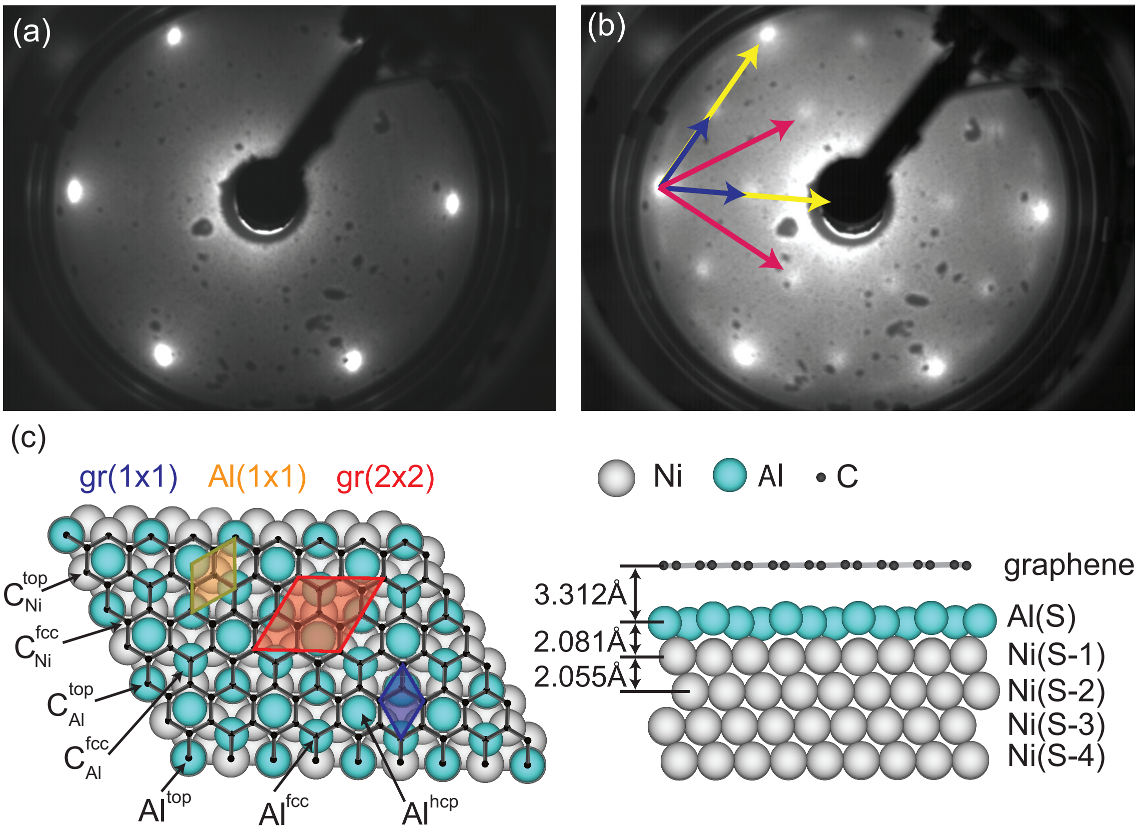

Figure 6.8: LEED pattern and atomic structure model of graphene on Ni(111) and on Al/Ni(111): LEED pattern are shown of graphene/Ni(111) (a) and graphene/1 ML Al/Ni(111) (b) the latter showing a (2 × 2). Additional diffraction spots appear at smaller $\mathbf{k}$*. (c) calculated top and side view of the explored atomic model including the mean distances. Different rhombuses mark the different unit cell of every reference system.*

in this structure is 2.877 Å, which is very close to the distance in the Al *fcc* bulk structure.

6.2.2 Core Level Spectroscopy

Starting from the clean graphene/Ni(111) system presented in *Chapter* 5, core level XPS spectra were recorded during the preparation steps of the graphene on Al/Ni(111) system (see *Figure* 6.9). The corresponding photon energies and the main photoemission features are marked in the figure. Deposition of 1 ML Al on graphene/Ni(111) leads to a decreased intensity of photoemission features from graphene and Ni without any observable energy shifts of the C 1s peak (blue curves in *Figure* 6.9 (c)). Subsequently, short annealing up to 400°C leads to the formation of graphene/Al/Ni(111) and therefore to strong changes in photoemission spectra (green curve in *Figure* 6.9). First, the intensities of the C 1s peak and the graphene π states are restored. At the same time the intensities of the Al 2s, 2p peaks are

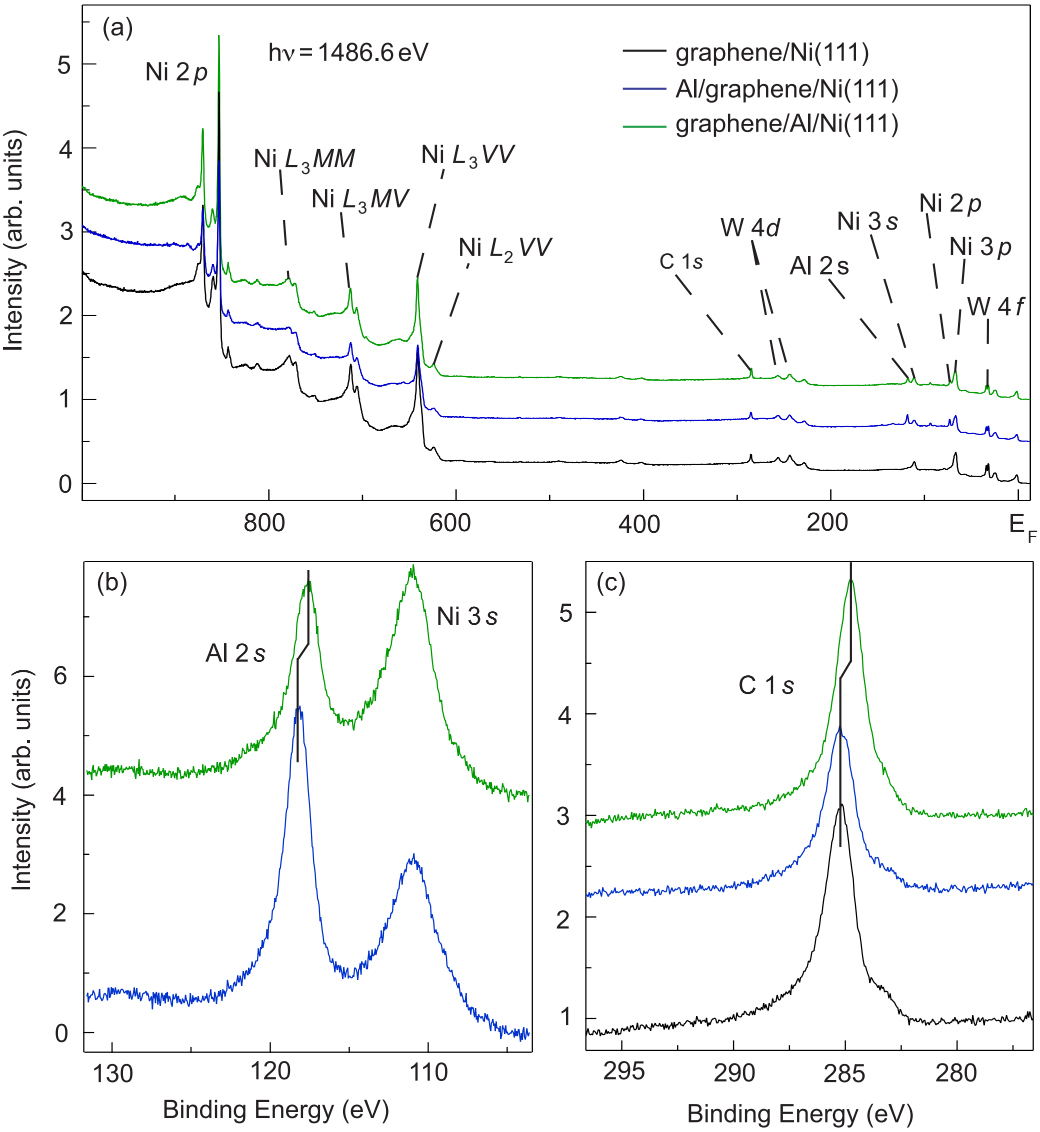

Figure 6.9: XPS overview and detailed core level spectra recorded during the preparation steps: The overview spectra in (a) do not contain additional features indicating contaminations. In the detailed core-level spectra, shown in (b) and (c), a clear shift is observed after intercalation of 1 ML Al underneath graphene on Ni(111).

reduced. These facts indicate that Al intercalates underneath graphene on Ni(111). After intercalation, the C 1s peak and the graphene π states are shifted by ≈ 0.45 eV and ≈ 1.6 eV to lower binding energies, respectively, compared to those for the graphene/Ni(111) system, indicating an electronic decoupling of the graphene layer from the substrate (see also *Section* 6.2.3). The Al layer which is placed between graphene and Ni(111) after intercalation is characterized by Al 2s, 2p photoemission peaks shifted to lower binding energies, with respect to Al/graphene/Ni(111). This indicates the interaction between Al and Ni and a partial charge transfer in the system. These observations are consistent with the previously reported data for the Ni-Al systems [185, 186]. The corresponding changes are also visible in the region of the Ni 3 d states in the vicinity of $\mathrm{E_F}$.

6.2.3 ARPES Results

Shown in *Figure* 6.10 is (a) the angle-resolved photoemission data along the high symmetry axes Γ-K-M-Γ, around the K-point along the direction perpendicular to Γ-K in (b) and along the Γ-K direction (c) of the first Brillouin zone. Interesting changes in photoemission data appear after intercalation of the Al layer underneath graphene on Ni(111) (see also *Figure* 5.3). The resulting photoemission spectra are presented in the same way as for graphene/Ni(111). First, the intercalation of Al leads to the decoupling of the electronic states of the graphene layer from those of the substrate. This results in the shift of all electronic bands of graphene to lower binding energies by 1.6 eV (see also *Figure* 6.9). Second, the electronic structure of the graphene layer as well as the Dirac cone in the vicinity of the Fermi energy are fully restored. The Dirac cone is shifted downwards from E_F to higher binding energy by 0.64 eV. Similar to earlier published results [38, 62, 146, 187] this shift is assigned to an n-doping of the graphene layer. The doping level of 0.64 eV is in very good agreement with the theoretically calculated value of 0.686 eV presented in *Section* 6.2.5 below. Via the area of the Brillouin zone covered by the occupied states of the π^* band it is possible to calculate the electron transfer of about 0.003 e^- per C atom from the metal substrate to graphene layer.

One can expect a that the Brillouin zone for graphene/Al/Ni(111) compared to graphene/Ni(111) is half the size, because of the size of superstructur unit cell. Such an effect cannot be observed from back-folded bands (so-called umklapp effects). It was demonstrated on La-graphite intercalation compounds that the strength of these umklapp-features scales with the strength of the interaction [188]; this is a general feature. Therefore, that such an influence is missing is a clear sign that Al intercalation fully decouples the graphene layer from the substrate.

6.2.4 X-Ray Absorption Spectroscopy

The unoccupied valence band states of graphene/Al/Ni(111) were studied by means of NEXAFS spectroscopy at the C K and Ni $L_{2,3}$ absorption edges, (see *Figure* 6.11). Angle-dependent NEXAFS spectra shown in *Figure* 6.11 for both systems represent a nice example, demonstrating the so-called search-light effect explained in *Chapter* 3 in detail. The C K NEXAFS spectra of the graphene/Ni(111) system in *Figure* 6.11 (a) have been studied and discussed in detail in *Chapter* 5 and in earlier published work [126, 138, 189]. These spectra serve here as reference.

Both spectra series in *Figure* 6.11 show the same angle dependence demonstrating the preservation of the orbital orientation upon Al intercalation. The intensity features in the energy range from 290 eV to 310 eV binding energy, which are assigned to the $1\,s \rightarrow \sigma^*$, have maximum intensity for normal incidence. The σ states

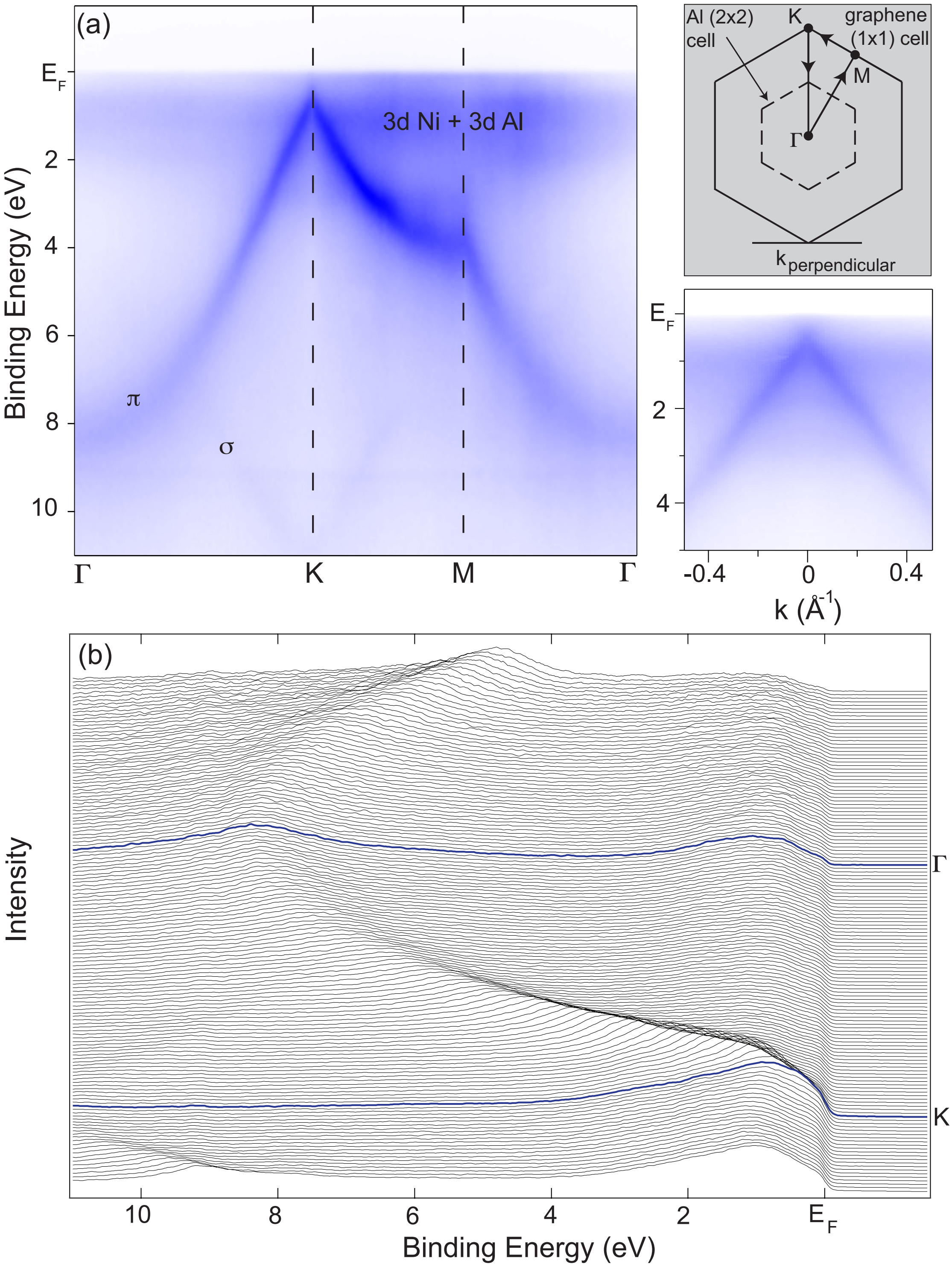

Figure 6.10: ARPES spectra of graphene/Al/Ni(111) taken at hν=63 eV photon energy: After intercalation the Dirac-cone is recovered shifted downwards by 0.63 eV to higher binding energies indicating n-doping. The signal of the 3d states of the transition metals are strongly suppressed.

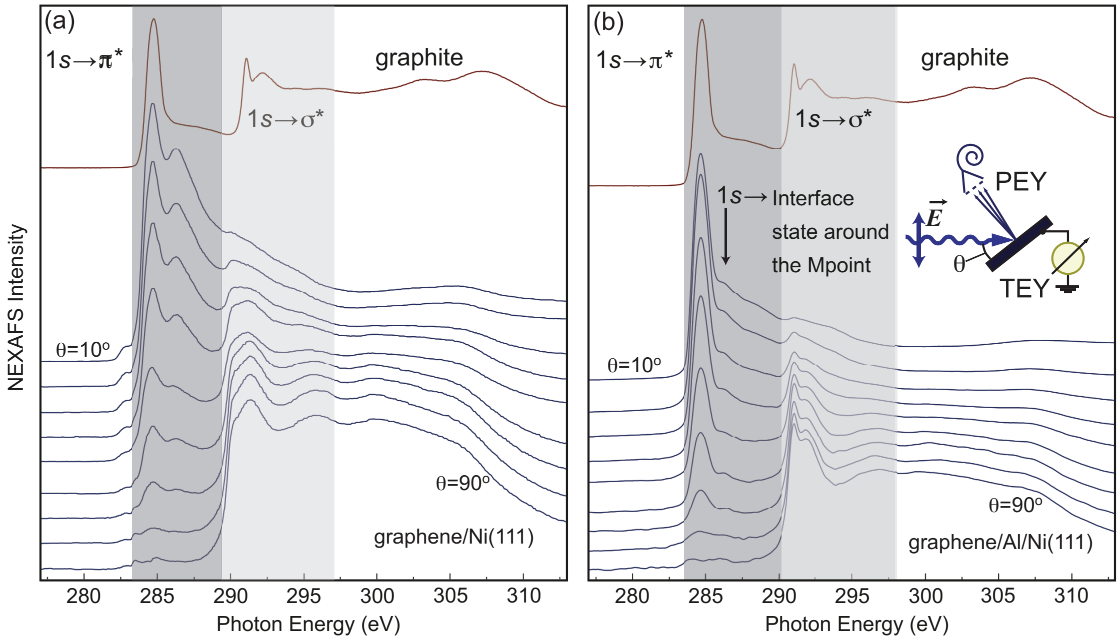

Figure 6.11: NEXAFS spectra of the C K edge at varied angle for both graphene/Ni(111) (a) and graphene/Al/Ni(111) (b): In the upper part NEXAFS spectra of the C K edge of graphite are shown and serve as reference.

of graphene/Al/Ni(111) are nearly unaffected compared to graphite.

As discussed extensively in *Chapter* 5.4 the case of the $1s \rightarrow \pi^*$ transition is different. The strong hybridization between the π and the $3d$ Ni states creates several unoccupied interface states, which induce a double peak structure at the $1s \rightarrow \pi^*$ transition of graphene/Ni(111). Intercalation of a thin Al layer underneath a graphene layer on Ni(111) leads to strong changes in the C K NEXAFS spectra in *Figure* 6.11 (b) and 6.12 (b). The shape of these spectra, the positions of main spectroscopic features as well as the energy separation between the π^* and σ^* features become similar to those in the spectra of pure graphite. These facts provide strong evidence for the fact that the graphene layer is decoupled from the substrate by intercalated Al, observations which are also consistent with the main conclusions of the band structure calculations and ARPES results above. Based on DFT calculations, the intense main π^* peak in the NEXAFS spectra of graphene/Al/Ni(111) can be assigned to the transition of an $1\,s$ core electron into the unoccupied states around the M point at ≈ 0.8 eV above E_F. The second spectroscopic feature at 286.3 eV photon energy (small shoulder in the region of the $1s \rightarrow \pi^*$ resonance) can be assigned to a transition of the electron from the $1s$ level into the graphene unoccupied states around the M point at ≈ 2.8 eV above E_F.

A reduction of about 880 meV in the energy separation between the π^* and σ^* features for all spectra in case of graphene/Ni(111) compared to that in the spectra of graphite or graphene/Al/Ni(111) shifts the σ^* resonance below 290 eV to 289.76 eV indicating an increased flatness of the graphene layer in graphite or graphene/Al/Ni(111). If the graphene layer exhibits a buckling the sp^2 hybridized σ orbitals together with the p_z orbital contain also an sp^3 compound leading to an approach to the absorption spectra of diamond because a z-compound is introduced to the σ states and a x-y-compound is introduced to the π states. Therefore NEXAFS spectra becomes closer to the NEXAFS spectra of diamond. Such changes was observed in NEXAFS spectra of diamond, nanotubes and fullerenes[190–192].

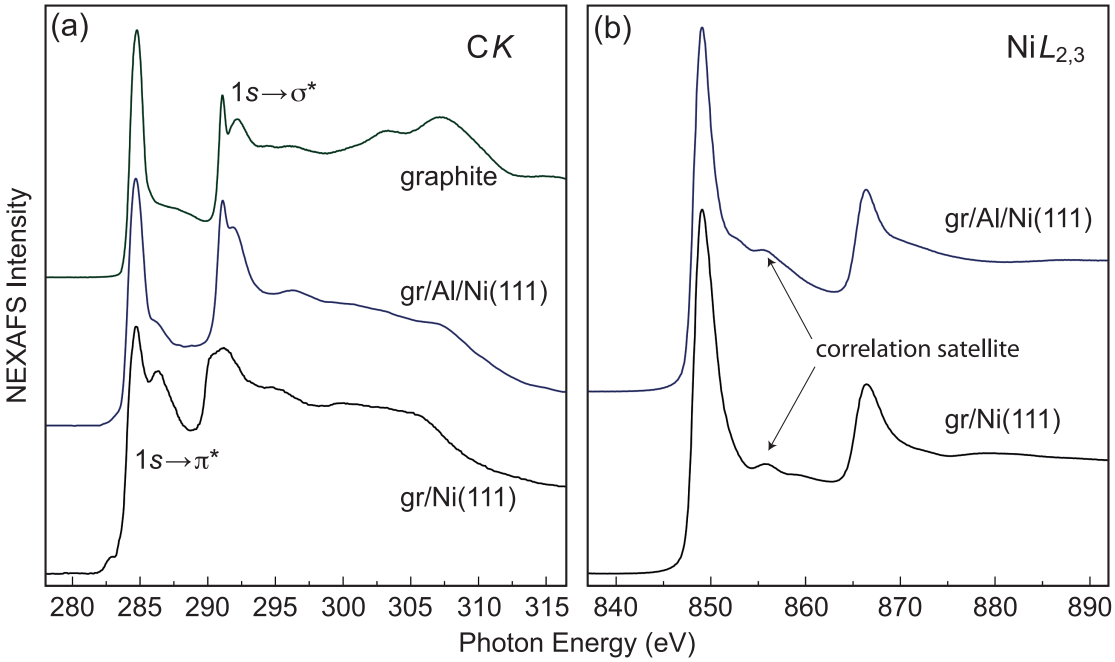

Figure 6.12: Comparison of the C K and $L_{2,3}$ absorption spectra for graphene/Ni(111), graphene/Al/Ni(111) and graphite.

Figure 6.12 (b) shows Ni $L_{2,3}$ NEXAFS spectra of graphene on Ni(111) and graphene on Al/ Ni(111). A noticeable modification of this spectrum after intercalation of the Al layer is clearly visible. The shape and the energy of the so-called 6 eV Ni correlation satellite are modified. Additionally, a small shoulder at ≈ 852.6 eV photon energy occurs. The resulting Ni $L_{2,3}$ NEXAFS spectrum is similar, to some extent, to that of Ni_3Al [185] and these spectral changes are explained by the charge transfer from Al on Ni. These experimental observations of the interaction at the Al/Ni interface are supported by the band structure calculations shown in *Figure* 6.13 (b) in *Section* 6.2.5. This charge transfer leads to a strong reduction of the Ni 3d magnetic moment from 0.528 μ_B for graphene/Ni(111) to 0.273 μ_B in graphene/Al/Ni(111). As a consequence, the interaction between the graphene layer and the substrate is reduced and graphene becomes decoupled with an electron doping that shifts the Dirac cone below E_F.

6.2.5 Comparison of Experimental Results with DFT Calculation for Graphene/Al/Ni(111)

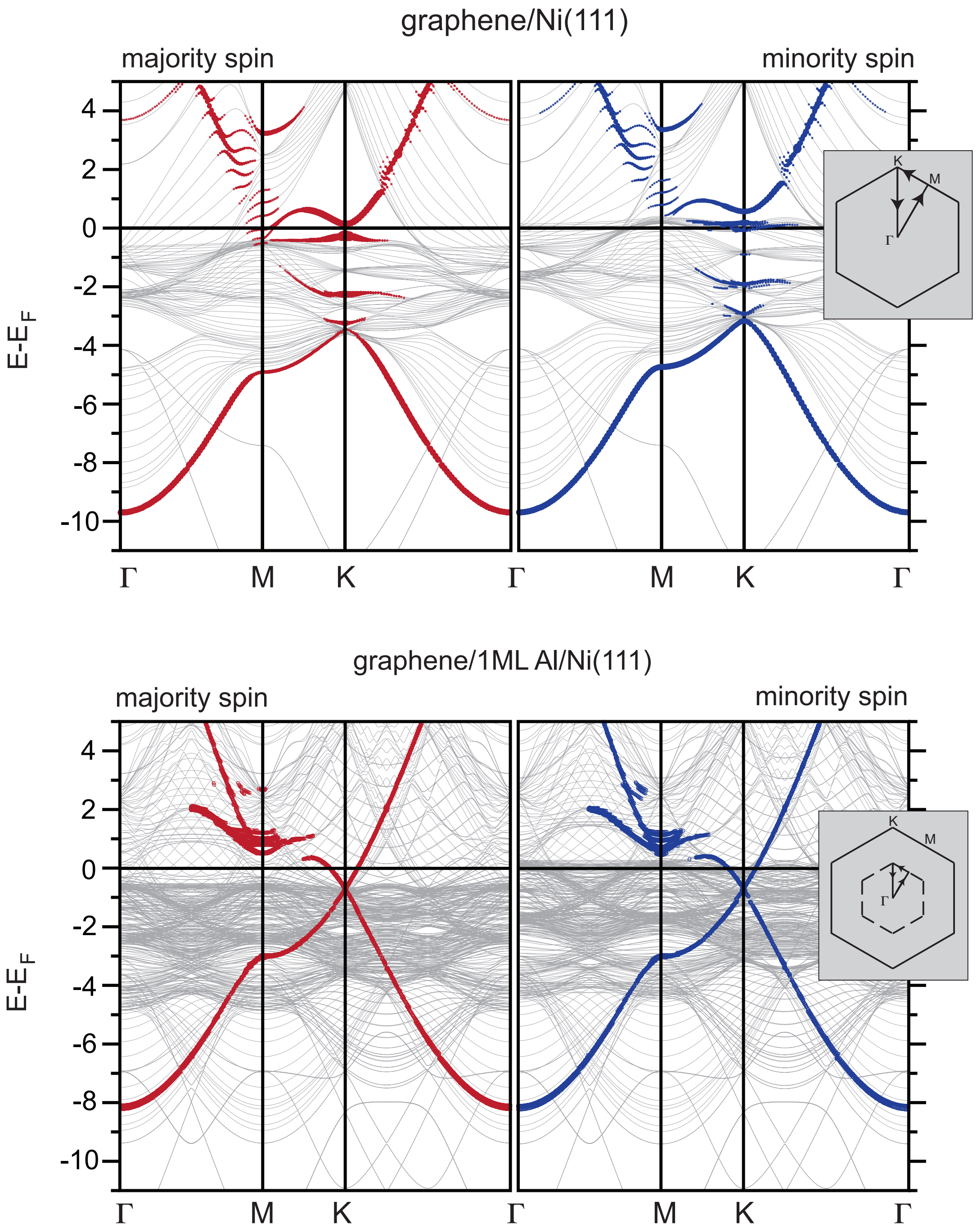

Figure 6.13: Calculated band structure before and after Al intercalation underneath graphene on Ni(111): In the case of graphene/Al/Ni(111) the backfolded band structure was chosen in order to show the result more clearly.

As in the case of graphene/Ni(111) and graphene/Fe/Ni(111), the DFT calculations were carried out by Dr. Voloshina using the projector augmented wave method [160], a plane wave basis set and the generalized gradient approximation as parameterized by Perdew *et al.* [157], as implemented in the VASP program [193]. The plane wave kinetic energy cutoff was set to 500 eV. The long-range van der Waals interactions were accounted for by means of a semiempirical DFT-D2 approach proposed by Grimme [194–196]. In the total energy calculations and during the structural relaxation, the positions of the carbon atoms as well as those of Al and the top two layers of Ni are optimized, the k-meshes for sampling of the supercell Brillouin zone are chosen to be as dense as 24×24 and 12×12, respectively, when folded up to the simple graphene unit cell. The system was modeled using a supercell consisting of 74 atoms. It has (2×2) lateral periodicity and contains 13 layers of Ni atoms, 4 atoms per layer, with one Al layer, 3 atoms each, and a graphene sheet, 8 atoms per layer, adsorbed on both sides of the slab. Metallic slab replicas are separated by ca. 24 Å in the surface normal direction, leading to an effective vacuum region of about 17 Å.

The calculated electronic band structure of the graphene/Al/Ni(111) system is strongly different from the one of graphene/Ni(111) (see *Figure* 6.13). Insertion of an Al layer between a graphene layer and Ni(111) decouples the electronic structure of graphene from the substrate, preventing hybridization between graphene π and Ni $3d$ valence band states. The Dirac cone in the graphene/Al/Ni(111) system is fully restored, and is shifted by 0.686 eV below the Fermi energy indicating electron doping of graphene on Al/Ni(111). This value is very close to 0.57 eV calculated recently for graphene/Al(111) by means of the local-density approximation with a distance of 3.41 Å between a graphene layer and the Al(111) surface [197]. The main π branches are clearly recognizable in the electronic structure of graphene/Al/Ni(111) and they almost reproduce the electronic structure of the free-standing graphene, except for a downward shift [134, 142]. Compared to graphene/Ni(111), in the intercalated system there is no strong hybridization between graphene and Al valence band states preventing the occurrence of a Dirac cone. There is only one energy region, away from Fermi energy, where such hybridization is visible, around M at approximately -1 eV binding energy. According to C atom site dependent calculations [144], in this region one can clearly see the disparity between different carbon atoms in the graphene (2×2) unit cell as the hybridization of the graphene π states from different carbon atoms with the Al $3p$ and Ni $3d$ valence band states leads to a splitting of the graphene-derived π band along M to K. Here one can conclude that the symmetry in the graphene lattice is broken. Surprisingly, such difference in the symmetry of the carbon atoms in the graphene layer of the graphene/Al/Ni(111) system does not lead to any sizable energy gap for the π states around the K point of the Brillouin zone. The appearance of such a gap was recently demonstrated by ARPES for graphene on Cu(111), Ag(111), and Au(111) [52, 198]. However, these observations are not supported by band structure calculations where very small [199] or no energy gap was observed for these surfaces [197].

6.2.6 Discussion

The results of the experiments as well as the calculations draw a single picture: the intercalated Al layer decouples graphene from the Ni(111) substrate accompanied by a charge transfer of 0.003 e^- per C atom.

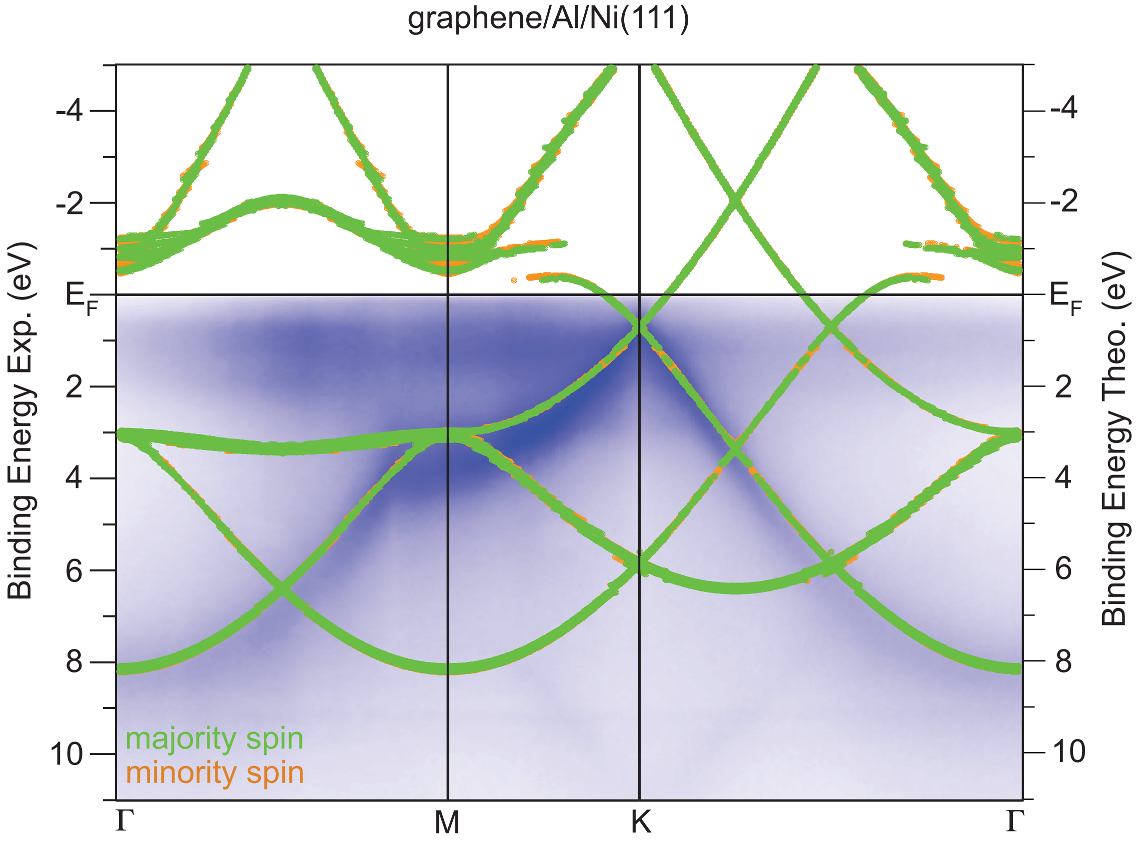

Figure 6.14: Projection of the spin-resolved DFT results on top of the APRES spectra: The majority and minority bands fit almost perfectly to each other. Hybridization features occur around the M point at 1 eV above the Fermi level only.

LEED measurements show that the graphene/Al layer form a (2×2) superstructure with respect to the graphene/Ni(111) unit cell. While the graphene becomes almost completely decoupled indicated by the increased distance of the graphene layer to the metal surface and the restored Dirac cones. Furthermore the increased energetic difference between the $1s \rightarrow \pi^*$ and $1s \rightarrow \sigma^*$ resonances indicates that graphene stays even more flat on top of Al/Ni(111) compared to on Ni(111) pointing to a decoupling as well.

In *Figure* 6.14 the DFT results are projected on top of the ARPES data in the range of the graphene Brillouin zone. Clearly visible is that the umklapp bands proposed by the calculations cannot be observed in the measurements. The missed umklapp features prove the decoupling further because the intensity of this features has to be scaled by the coupling strength of the interaction between the single system which compose the superstructure [188]. This fact is not accounted by the

DFT calculations. *Appendix* A shows DFT results in the Brillouin zone of graphene exhibiting clearly umklapp features.

The almost perfect fit of the experimental data with theoretical results indicates that the long-rang van der Waals interaction plays a significant role between the graphene and the metal substrate. In contrast, this interaction was not included in the calculations of the graphene/Ni(111) and graphene/Fe/N(111) system leading to obvious misfit of the theoretical and experimental Fermi levels. A second interaction is a charge transfer of about $0.003\,\mathrm{e}^-$ per C atom to graphene layer. The value was calculated from the downward shift of the Dirac cone to higher binding energies.

A magnetic coupling between the electronic system of the graphene and the metal substrate can be excluded because of the fit of the majority and minority bands, clearly visible by the nearly completely coverage of minority states by the majority states in *Figure* 6.14. Note that this fact is not equivalent to the situation if the graphene electrons exist in a magnet field free space; the graphene exist still in the macroscopic magnet field of the Ni substrate. Because of the lack of spin-dependent interface states in the vicinity to the Fermi level, XMCD measurements were not performed for this system. It can be speculated that the interface layer of the Ni substrate exhibits an decreased magnetization because of an expectable charge transfer from the Ni to the Al, similar to the graphene/Ni(111) system. But a magnetic coupling from the Ni to the graphene through the Al spacer layer cannot be expected considering that Al is not ferromagnetic and the increased interlayer distance between the graphene and the metal surface.

Concerning future applications, the electronic configuration of this system can be summarized as nearly free-standing graphene electrostatically coupled to Al/Ni(111) substrate. If the linear dispersion is assumed at the Fermi level, a mass less behavior of charge carriers can be expected.

A future application which is in the focus of the present work is the spin-FET realized by an electrically isolated graphene layer on a ferromagnetic substrate. The idea was to form a graphene/AlO_x/Ni(111) interlayer via O_2 intercalation underneath graphene on top of Al/Ni(111). The possibility to intercalate O_2 underneath graphene was demonstrated on graphene/Ru(0001) [182, 183]. In a series of sample preparations, it was found that O_2 does not intercalate as desired. The graphene/Al/Ni(111) sample was exposed to an oxygen atmosphere of $1{\cdot}10^{-6}$ mbar at room temperature for 30 min and at 450 K for 60 min. At room temperature no changes in the electron valence and core level spectra were observed. In this preparation step graphene acts as a passivation layer of the Al/Ni(111) substrate. Such a behavior was already reported for Ni(111) [123] and Fe/Ni(111) [124]. Strong changes occur in case of 450 K annealing temperatures. The intensity of the C $1\,s$ emission was decreased accompanied by a shift of the π states to higher binding energies and a restored $3\,d$ Ni emission intensity. Two scenarios are possible. Firstly, the Al atoms segregate into the Ni bulk and graphene couples to Ni again. It was observed that it is possible to restore the graphene/Ni(111) completely by extended annealing. The scenario of Al dilution does not explain the loss in C $1\,s$ intensity, however the second scenario assumes a breaking of the graphene layer and the migration of the Al atoms on top of the graphene layer. This explanation is in line with all observations such as the reduction of C 1*s* emission and the increased binding energy of the π states. Furthermore, it can be assumed that both scenarios occur simultaneously. A dissociation of the graphene layer to CO and CO_2 at 450 K also be considered, but would be in strong contrast to the O_2 intercalation at 850 K underneath graphene on Ru(0001).

Summarizing the O_2 intercalation experiment, the intercalation process in case of graphene/Al/Ni(111) does not run similar to graphene/Ru(0001). Temperatures up to 850° C were successfully used in the case of graphene/O/Ru(0001). Such temperatures are not possible in case of graphene/Al/Ni(111) because graphene on top of Al/Ni(111) breaks already at 450° C.

6.3 Discussion and Comparison of Ferromagnetic and Nonferromagnetic Intercalants

First of all, it can be concluded that the intercalates Fe and Al behave completely differently. The Al intercalant grows in a (2×2) structure underneath graphene and creates a large distance between the graphene and the Ni(111) substrate, suppressing strong interaction. In comparison, Fe intercalates in a (1×1) structure, preserves a continuing d-electron driven periodic potential, except for a reorientation from the top-fcc to the top-hollow configuration. The flatness of graphene layer is increased after Al intercalation compared to Fe, as shown by the energetic separation of the C $1s \rightarrow \pi^*$ and the C $1s \rightarrow \sigma^*$ transition. The possibility and the strength of a buckling in case of graphene/Ni(111) and graphene/Fe/Ni(111) is still under debate.

Both intercalants influence the valance band structure very differently. Al decouples the graphene nearly completely in contrast to Fe which shows no remarkable changes in ARPES spectra indicating the preservation of the strong interaction. This becomes clear from the unchanged majority spin band structure and particular by the modification of the minority spin band structure. In general, all features of the graphene/Ni(111) are preserved such as the interface states. The n-doping effect is a common aspect of both intercalants following from the high electronegativity of C. The different amount of transferred electrons ($0.003\,\mathrm{e}^-$/C atom for Al and $0.15\,\mathrm{e}^-$/ C atom for Fe) is assigned to the element-specific electronegativity. Further, the structure of the intercalant plays a role in this doping process because of the different number of contact atoms. Note that in the description of the doping level in the rigid band model, the band structure has to be taken into account. If a band gap is opened like in graphene/ Ni(111) or graphene/Fe/Ni(111), a transfer of an electron into the next empty state can shift the bands rigidly by several hundred meV. In contrast, graphene/Al/Ni(111) has a continuous graphene π band around the Fermi level. Thus the doping level is linearly connected with the amount of the charge transfer. The electron transfer also affects the magnetic moment of the Ni interface layer. Al, which exhibits an unpolarized band structure, reduces and Fe with polarized $3\,d$ bands increases the magnetic moment of the first Ni layers.

Chapter 7

Multilayer Graphene on Ni(111)

This chapter describes experiments which were performed to study a modification of graphene on Ni(111) which may lead to the desired spin filter application mentioned in the introduction. As described in detail in *Chapter* 2, Karpan *et al.* predicted that the conductance across a nickel-graphene-nickel sandwich only acts as a reasonable spin filter if several graphene layers are stacked on top of each other. The reason for this behavior is easy to understand; for thin graphene films, tunneling of electrons may occur, which do not have to obey the spin-dependent transport caused by the difference in overlap of spin-up and spin-down electrons. A technology based on such a sandwich arrangement permits to change from the binary system consistent of “0” and “1” to the ternary system consisting of “0”, “1” and “2”, coding the information in spin-up current, spin-down current and no current bits. A more detailed introduction to the principles of a spin-filter devices based on the graphene/Ni(111) junction is presented in *Chapter* 2.

Thus in order to obtain the spin filter properties, it is necessary to grow an oriented multilayer of graphene on top of Ni(111); moreover, this layer should behave like a nearly free-standing graphene and still be electronically coupled to the Ni(111) substrate, i.e. the strong interaction between Ni and graphene explained in detail in the previous chapters should be removed, since it is detrimental to spin filtering.

In the experiments described here we achieved bilayer growth of graphene on Ni(111). In these systems, however, the first layer was still strongly coupled to the metal. Thus, in a second step a gold layer was intercalated between the graphene double layer and the substrate to achieve the decoupling, a well known process already described (for the case of copper intercalation) by Dedkov *et al.* in 2001 [130]. These results can be considered the first step towards realizing a spin filter sandwich, although it must be said that the grown structures were only measured by photoelectron spectroscopy, and a structural characterization is highly desirable.

The challenge for multilayer growth is to overcome the passivation effect of the first graphene layer [125], described for the present system by Dedkov *et al.* in 2008 [123, 124], when trying to grow the second layer by dissociation of hydrocarbons at relatively low pressures in an ultrahigh vacuum chamber. For the growth of graphene on silicon carbide, this is relatively straightforward, since the graphene

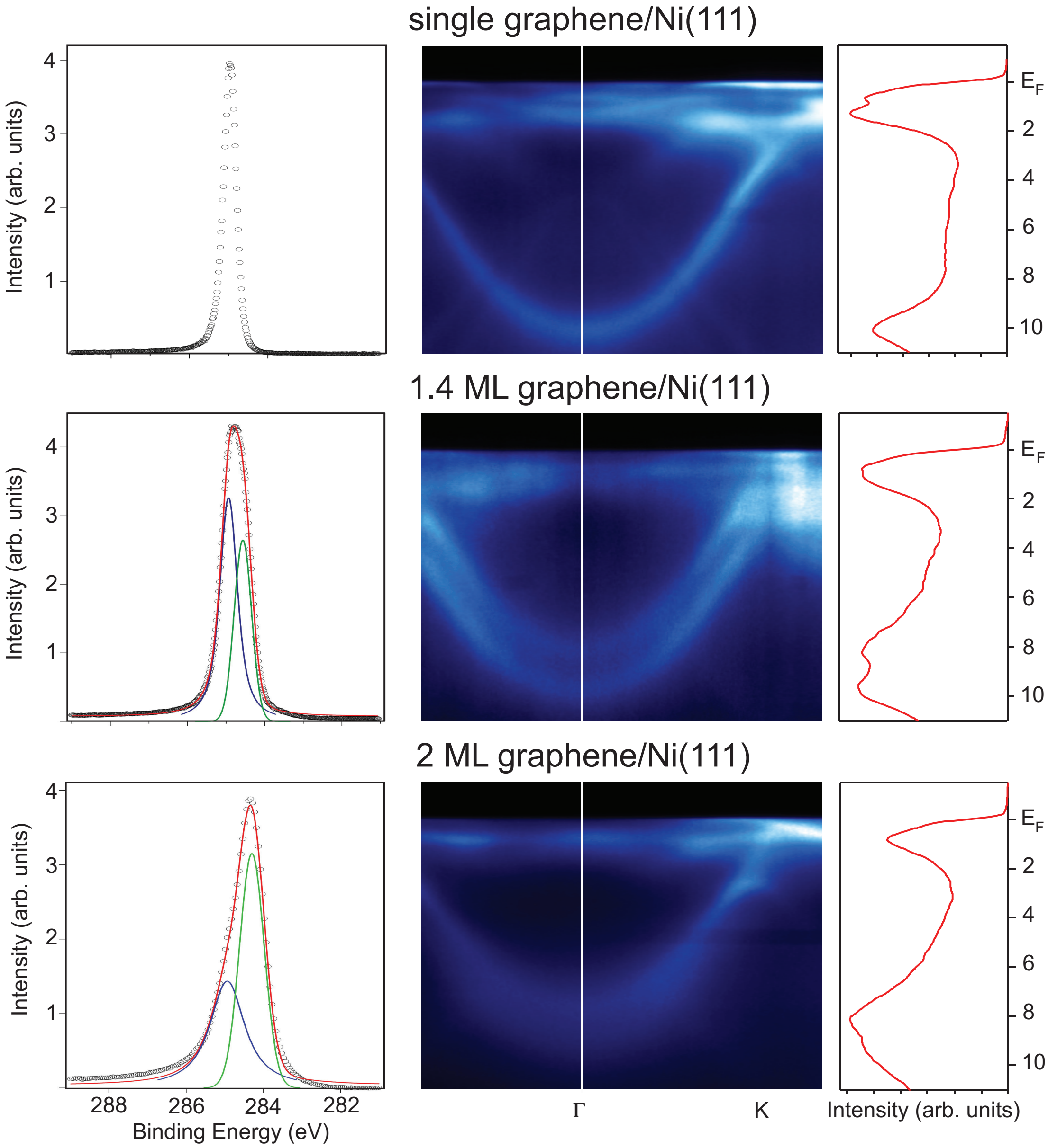

Figure 7.1: ARPES and C 1s spectra taken from different numbers of graphene layers: The ARPES spectra clearly monitors the appearance of two different π electron systems. The lower parabola is assigned to the first, strongly bound graphene layer. The upper parabola shows nearly free-standing graphene behavior, therefore it is assigned to the top layer.

films are prepared by thermal dissociation of the topmost SiC layers, such that the silicon desorbs and the remaining carbon layer(s) remain [38]. Oshima *et al.* were able to achieve the beginnings of a second layer in graphene growth on TaC, although a complete layer was not completed. By using pyridine (C_5H_5N), which had been previously used in order to achieve electron doping through inclusion of nitrogen atoms into the graphene lattice, we were able to grow double layers, although in a relatively small temperature window. The used preparation method is described in *Chapter* 4.

The successful growth of multilayer graphene is evident from the occurrence of a second parabola that parallels the one from the single layer at smaller binding energies in ARPES data (see *Figures* 7.1 and 7.2). The spectra in *Figure* 7.1 top show the photoemission signals of a single layer of graphene on Ni(111) already discussed at length in preceding chapters. The center photoemission image (see *Figure* 7.1) clearly shows the second parabola, also evident from the cut along the energy axis at the Γ point where the bottom of the π band has two peaks at different binding energies. The splitting between the two bands is much larger than that expected from the two bands that occur in a bilayer where both layers are decoupled from the substrate such as on SiC(0001) [38]. Therefore, I conclude that this π band originates from a second graphene layer on top of the first one, where the first layer is still strongly coupled, whereas the second layer is decoupled from the Ni(111) substrate. The bottom photoemission image in *Figure* 7.1 shows what we conclude to be a completed bilayer; all layer estimates are based on the line shape analysis of the carbon 1s core level photoemission line shown on the left hand side in *Figure* 7.1.

An uncertainty in the estimate of the number of layers present on the sample arises from the unknown surface morphology. A correct evaluation of the film thickness through core level line intensity its requires a homogeneously flat film. However, the surface of the first graphene layer is chemically inert, and so is every higher graphene layer also. It is likely that defects and step edges provide a starting point of second layer growth, although no evidence for this is available at present. If we start from the assumption that defects and step edges are the nucleation points for the second layer, a growth in islands is expected. Whether this provides the smooth layer morphology required for the spin-filter properties of such a device is still an open question. What is also not clear is the role of the pyridine in second layer growth. Note that in these experiments both layers were grown by pyridine as the active molecule in CVD growth. Since pridine is likely to provide more defects in the film, at single defect sites where the nitrogen resides before being driven off the surface by annealing, this can leave active sites where pyridine molecules can attach to and dissociate to leave carbon atoms free to form the second layer.

A further result of the ARPES measurements, critical for the spin-filter effect was that multilayer graphene grows in different rotation modes on top of the first strongly bounded layer. The first layer is always oriented because of the strong interaction with the Ni substrate. However, the ARPES data in *Figure* 7.2 (a) and (b) reveal a clearly different Brillouin zone orientation of the topmost layer with respect that of Ni(111) and the first graphene layer. For the first rotation mode in *Figure* 7.2 (a) the Dirac cone of the nearly free-standing graphene topmost layer is found along the Γ-K direction of the strongly bound first layer which has the same orientation as the Ni(111) substrate. A detailed analysis of constant energy cuts shows that the topmost layers grow with a rotation angle distribution around 23.8° and 36.2° rotation angle with respected to the first graphene layer. In contrast,

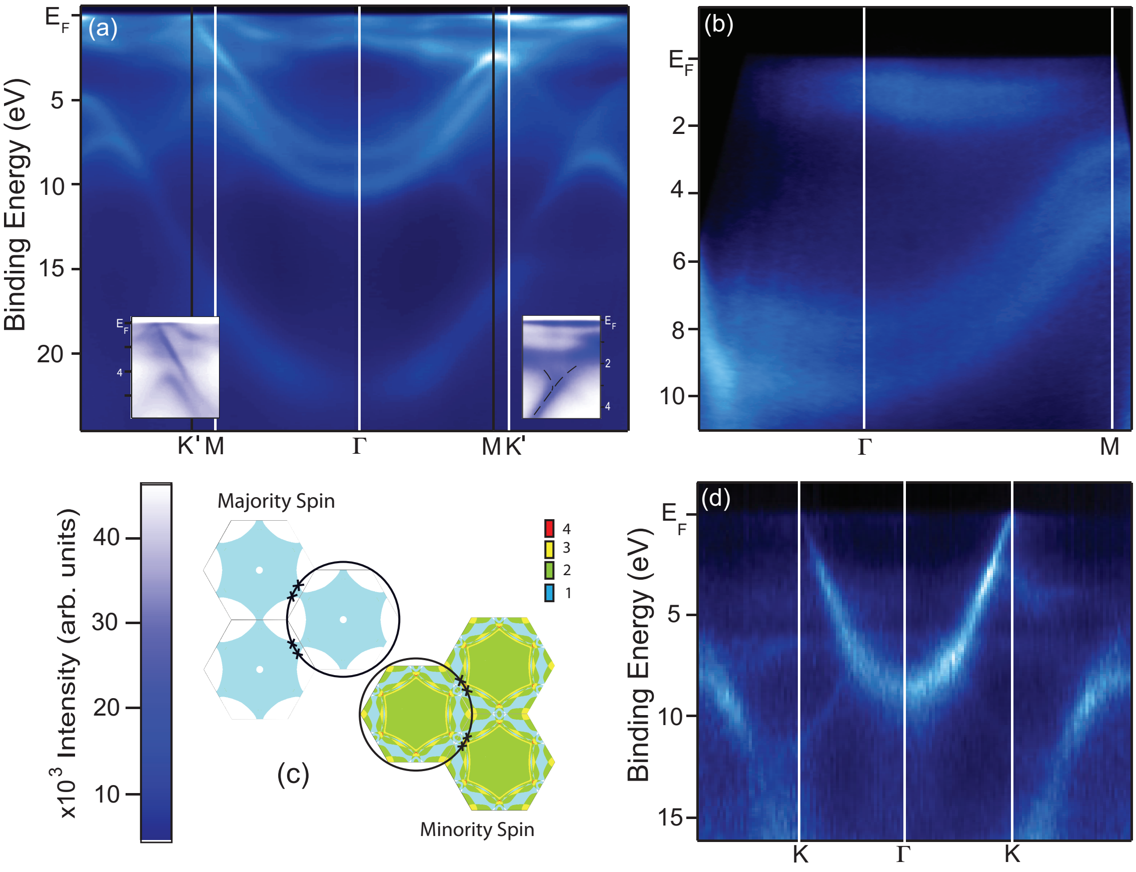

Figure 7.2: (a) and (b): ARPES valence band spectra of two samples with rotated (a) and unrotated (b) top layer. The two Brillouin zones are labeled in (a). (c) shows the spin resolved DOS of the Ni(111) Fermi surface projection. The black circles mark the positions of the Dirac cones in case of an arbitrary rotation angle of the top layer. The observed case of rotation angles 23.8° and 36.8° the positions are marked by black crosses, indicating where the Dirac cones meet with the DOS of both spin species in the second Brillouin zone. (d) shows the ARPES spectra taken after Au intercalation, indicating the decoupling of the full graphene stack and the reorientation of the top layer.

in the ARPES spectra presented in *Figure* 7.2 (b), both graphene π bands show a parallel dispersion. Therefore, the M points of the Brillouin zones of the first and the topmost layer meet. The topmost layer remains aligned to the strongly bound first layer.

The mutual orientation of the graphene layers is extremely important for the filter effect of such a graphene-based junction. This becomes obvious from the theoretical predictions by Karpan [67] in *Figures* 7.2 (c) and 2.10 (b) in *Chapter* 2. As mentioned in *Chapter* 2, the spin filter effect relies on the overlap of the Dirac cone with Ni(111) minority-spin states and of the absence of Ni(111) majority-spin states at the Fermi level. If the topmost layer has a rotated orientation with respect to the Ni(111) surface, the Dirac cone also overlaps with majority-spin states which block the filter effect. The occurrence of the Dirac cone in the rotated case for rotation angles of 23.8° and 36.2° is marked by black crosses in *Figure* 7.2. It is clearly visible that the Dirac cone of the topmost layer overlaps with both kinds of spin states. Therefore, only the orientated graphene stack structure is desired for use in spin-filter device.

However, both types of samples, the rotated and the unrotated, do not fulfill all requirements to act as spin filter. It is the first, strongly bound layer which keeps them from being a perfect spin filter; the hybridization between the graphene π states of the first layer and the Ni(111) substrate creates interface states which act as a majority spin injectors exactly at the K point as described in *Chapter* 5. However, the tunneling probability of electrons which occupy the Ni(111) minority states, through the first graphene layer from the Ni(111) surface into the unoccupied states of the second graphene layer is considerable. As a consequence, in this configuration both spin species are transferred into higher layers, one from the interface state and one from the tunneling through the first strongly bound layer, thus destroying the spin-filter effect. Therefore Karpan *et al.* suggested to decouple the graphene stack via intercalation of one atomic layer of Cu. They calculated that by doing so, the efficiency is only reduced from 100 % to 98 %, still an almost perfect value.

In order to prepare a nearly perfect spin-filter, we performed an experiment in which a one atomic thick Au was intercalated. It is well know that Au also acts as a decoupling spacer layer similar to Cu. This preparation step was performed on a sample which exhibited a rotated topmost layer (see *Figure* 7.2 (d)). First of all, we found that the Au intercalates underneath both layers and and decouples the full graphene stack. Both π bands from the strongly bound and the topmost graphene then forma bilayer as known from nearly free-standing graphene. Interestingly, the π band intensity of the rotated topmost layer is notably weakened. This can be explained by the alignment process of the top layer with respect to the formerly strongly bound graphene layer and the Ni substrate. For comparison, in *Figure* 7.2 (a) and (d) the ARPES spectra of the same sample before and after the intercalation are shown. The mechanism of reorientation cannot be explained by a rotation of the full layer, islands or flakes, because of the large amount of energy which is required for such a process. A more realistic explanation would be a dissolving process of the topmost graphene layer in the Au material during the intercalation followed by a regrowth into an oriented way.

7.1 Discussion

The intercalation of Au underneath the full graphene stack and the reorientation of the topmost layer in case of the rotated graphene overlayer are two promising routes for the use of graphene on Ni(111) in spin-filter devices. These effects of the Au intercalation give the possibility to not only decouple the graphene stack, but also to tune the system into a state which fulfils all spin-filter conditions.

Future experiments on this system should focus on the investigation of the surface morphology in order to clarify whether the single layer graphene on top of Ni(111) is fully and homogeneously covered with additional graphene layers. Furthermore, it can be speculated that the dilution of the top layers can also improve the flatness of the graphene stack. After the improvement of the sample quality with regards to the flatness and the number of layers, the next experiments should approach the central question, “Does a graphene stack separated and decoupled by a spacer layer act as a spin-filter?”. To this end, it is necessary to measure the spin dependent conductance perpendicular to the surface, a challenging task. Another experiment which is quite feasible is to measure the induced magnetic moment of the top layer. If the top layer shows a magnetic moment aligned antiparallel to the Ni magnetization, it is clear that the whole stack couples to the underlying Ni(111) substrate as predicted by Karpan *et al.* [12, 67].

Chapter 8

Summary and Outlook

8.0.1 Summary

In this work the electric and magnetic interactions between graphene and ferromagnetic substrates were investigated. Starting from the ground system graphene on Ni(111) ways were found to increase or to suppress the interaction between the carbon layer and the substrate via intercalation of different metals underneath. This opposite behavior was explained by different strength of hybridization between the graphene and varied substrates. In further experiments were focused to tune graphene/metal systems into structures which are supposed to be possible future spintronic applications, namely the spin filter and SFET.

In the case of graphene/Ni(111) strong interactions between the graphene π states and the Ni $3\,d$ states were observed deforming the π band around the K point. The σ bands are only shifted rigidly downwards indicating that these state are not strongly involved to bonding mechanism between the graphene layer and the substrate. The origin of these differences in the interaction strength is the perpendicular real space orientation of the σ states with respect to the π states proven in NEXAFS experiments. The interacting between the π states of the graphene and Ni $3\,d$ states is explained in terms of hybridization forming several new interface states around the K and around the M point. A specially the Dirac cone at the K point vanishes, instead the matching point of the π and the π^* band, the π band changes continuously from states with pure π character into states which exhibit pure $3\,d$ character. A particular observation is the occurrence of new interface states at the Fermi level which are energetically split in dependence of the spin state. The localization of these states at the Fermi level leads to different occupation and thus to different amount of minority spin and majority spin electrons observed as an into the graphene layer induced magnetic moment.

The possibility to tune the electric and magnetic interaction was investigated via intercalation of an one atomic thick Fe or Al layer. After the intercalation, Fe atoms are stabilized in fcc γ phase structure underneath graphene on Ni(111). The so formed metal graphene interface has the same periodicity like the graphene/Ni(111) interface. Therefore similar interactions are expectable. However, the Fe layer create a new quantum well state at substrate surface, which belongs clearly to the minority spin band structure. This new quantum well state hybridizes together with the partially filled in graphene/Ni(111) observed minority interface state. This further hybridization shifts the minority graphene states of about 1 eV above the Fermi level emptying the minority spin states. The majority spin bands occur almost unaffected by the intercalation of Fe. The influence of intercalation to majority and minority bands together preservers almost the valence band structure.

The intercalation of Al underneath graphene drastically changes the interaction. After the intercalation graphene stays nearly decoupled on top exhibiting a valence band structure similar to free-standing graphene. The interaction is reduced to an n-doping of $0.003\,e^-$ per C atom.

After the investigation of methods to increase or almost switch-off the interaction between graphene and the ferromagnetic substrate the focus was shifted to graphene spintronic applications. One promising way is to realize a spin filter devices via a stack of graphene layers on Ni(111) [12, 67]. A way was found to overcome the passivation effect of the first grown graphene layer while the CVD preparation of graphene on Ni(111) [123–125]. So it was possible to grow ordered multilayer graphene on Ni(111) in two different rotation modes. In ARPES measurement clarified that the first graphene layer is strongly bounded to Ni substrate avoiding the spin filter effect. In order to turn such multilayer system into the desired spin filter configuration a monolayer Au was successfully intercalated underneath the whole graphene stack. ARPES measurements show that after Au intercalation the whole graphene stack exhibit valence band structure similar to free standing graphene. These graphene multilayers have the by Karpan *et. al* required valence band configuration. Therefore these prepared systems are promising candidates.

The second idea was to prepare graphene electrical insulated on a ferromagnetic substrate via intercalate of O_2 underneath graphene on Al/Ni(111). It was expected that intercalation of O_2 forms graphene/AlO_x/Ni(111). Here the AlO_x layer acts as a insulating space layer between the graphene and the ferromagnetic substrate. Unfortunately this procedure does not work the graphene layer break before intercalation of O_2 could be observed.

8.0.2 Outlook

After successfully characterization of the electronic valence band structure of multilayer graphene on Ni(111), the next step is the verification and the investigation of the spin selective interface transmission. Important questions are: Is the spin-polarized signal large enough to sensor? Up to which distances of the graphene Ni interface, spin polarization can be evidenced? Occur magnetic effects originating from the spin polarized current? These and several more questions have to be answered before graphene spin filter applications are thinkable.

The spectroscopic methods, which were used in the present work, are not suited to investigate such effects. Because the filter effect is determined by the states in vicinity to the Fermi level and PES excites electrons into states far above the Fermi level. Absorption experiments excite core electrons into empty valence band states. In the case of the flat spin-split interface state in the graphene/Ni(111) the XMCD contrast was rather small. I expect for the case of a time and space limited polarization of the conduction bands, originating only on the transmission process, is not observable XMCD contrast.

Suited experiments are STM measurements, which provide information about the surface morphology and layer quality, and spin-resolved transport measurements, which are the ultimate prove of this effect.

Appendix A

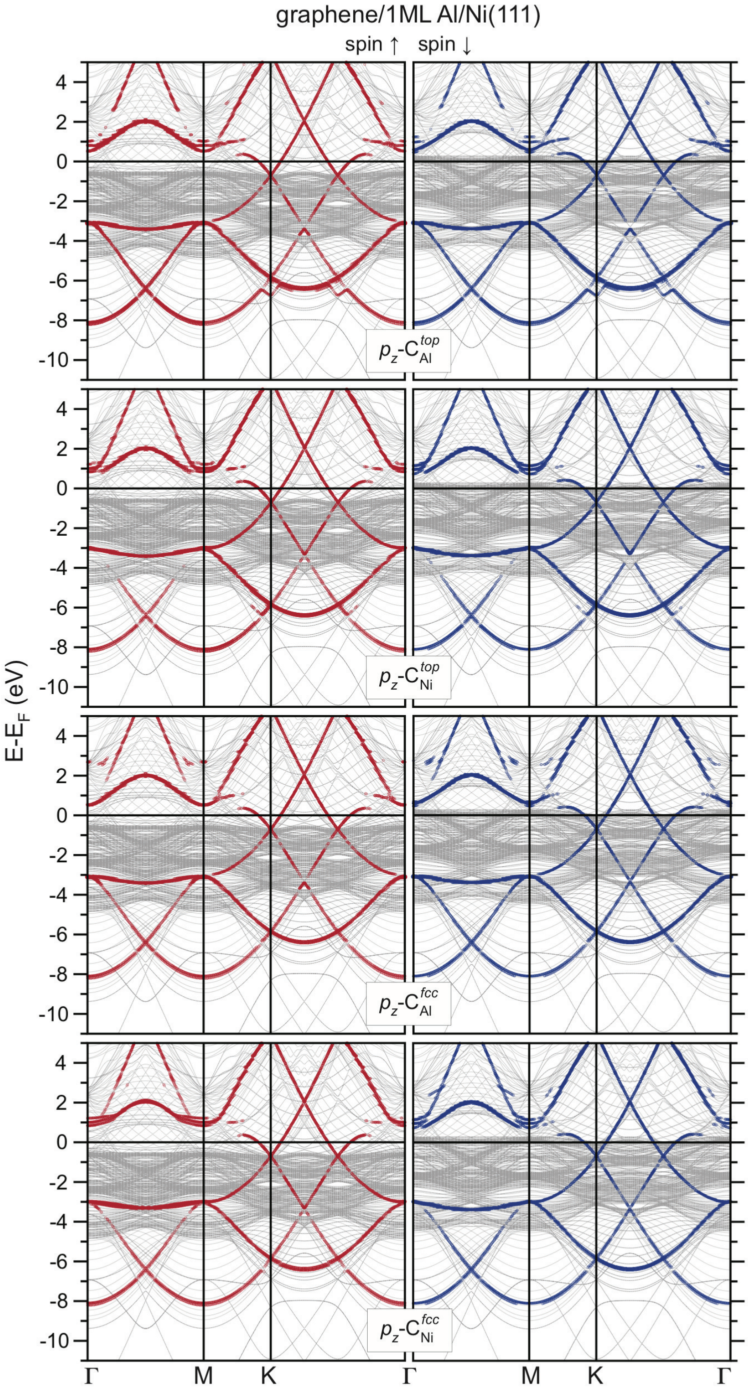

Figure 8.1: Calculated π band structure of graphene/Al/Ni(111): The π band shows clear umklapp effects. Especially visible along Γ-K direction, the π band is mirrored after 2/3 of the distance.

Bibliography

[1] P. R. Wallace. “The band theory of graphite”. In: *Physical Review* 71 (1947), page 622.

[2] M.S. Dresselhaus and G. Dresselhaus. “Intercalation compounds of graphite”. In: *Advances in Physics* 30 (1981), pages 139–326.

[3] R. E. Peierls. “Quelques propriétés typiques des corps solides”. In: *Ann. Inst. Henri Poincare* 5 (1935), pages 177–222.

[4] L. D. Landau. “Zur Theorie der Phasenumwandlungen II.” In: *Physikalische Zeitschrift der Sowjetunion* 11 (1937), pages 26–35.

[5] K.S. Novoselov, A.K. Geim, S.V. Morozov, D. Jiang, M.I.K.I.V. Grigorieva, S.V. Dubonos, and A.A. Firsov. “Two-dimensional gas of massless Dirac fermions in graphene”. In: *Nature* 438 (2005), pages 197–200.

[6] Y. Zhang, Y.W. Tan, H.L. Stormer, and P. Kim. “Experimental observation of the quantum Hall effect and Berry’s phase in graphene”. In: *Nature* 438 (2005), pages 201–204.

[7] E. McCann, K. Kechedzhi, V.I. Fal’ko, H. Suzuura, T. Ando, and B. L. Altshuler. “Weak-localization magnetoresistance and valley symmetry in graphene”. In: *Physical Review Letters* 97 (2006), page 146805.

[8] P. Neugebauer, M. Orlita, C. Faugeras, A.L. Barra, and M. Potemski. “How perfect can graphene be?” In: *Physical Review Letters* 103 (2009), page 136403.

[9] W. Han and R.K. Kawakami. “Spin Relaxation in Single-Layer and Bilayer Graphene”. In: *Physical Review Letters* 107 (2011), page 47207.

[10] A.K. Geim and K.S. Novoselov. “The rise of graphene”. In: *Nature Materials* 6 (2007), pages 183–191.

[11] N. Tombros, C. Jozsa, M. Popinciuc, H.T. Jonkman, and B.J. Van Wees. “Electronic spin transport and spin precession in single graphene layers at room temperature”. In: *Nature* 448 (2007), pages 571–574.

[12] V.M. Karpan, P.A. Khomyakov, A.A. Starikov, G. Giovannetti, M. Zwierzycki, M. Talanana, G. Brocks, J. Van Den Brink, and P.J. Kelly. “Theoretical prediction of perfect spin filtering at interfaces between close-packed surfaces of Ni or Co and graphite or graphene”. In: *Physical Review B* 78 (2008), page 195419.

[13] A.H.C. Neto, F. Guinea, N.M.R. Peres, K.S. Novoselov, and A.K. Geim. “The electronic properties of graphene”. In: *Reviews of Modern Physics* 81 (2009), page 109.

[14] A.K. Geim. “Graphene: status and prospects”. In: *Science* 324 (2009), pages 1530–1534.

[15] D. R. Cooper, B. D’Anjou, N. Ghattamaneni, B. Harack, M. Hilke, A. Horth, N. Majlis, M. Massicotte, L. Vandsburger, E. Whiteway, et al. “Experimental review of graphene”. In: *arXiv preprint arXiv:1110.6557* (2011).

[16] J. Wintterlin and M.L. Bocquet. “Graphene on metal surfaces”. In: *Surface Science* 603 (2009), pages 1841–1852.

[17] H. Raza. *Graphene Nanoelectronics: Metrology, Synthesis, Properties and Applications*. Springer Verlag, 2012.

[18] K.E. Geckeler and S. Samal. “Syntheses and properties of macromolecular fullerenes, a review”. In: *Polymer International* 48 (1999), pages 743–757.

[19] R. Saito, G. Dresselhaus, M.S. Dresselhaus, et al. *Physical properties of carbon nanotubes*. Imperial college press London, 1998.

[20] J.C. Meyer, A.K. Geim, M.I. Katsnelson, K.S. Novoselov, T.J. Booth, and S. Roth. “The structure of suspended graphene sheets”. In: *Nature* 446 (2007), pages 60–63.

[21] E. McCann. “Electronic properties of monolayer and bilayer graphene”. In: *Graphene Nanoelectronics* (2012), pages 237–275.

[22] F. Bloch. “Über die Quantenmechanik der Elektronen in Kristallgittern”. In: *Zeitschrift für Physik A Hadrons and Nuclei* 52 (1929), pages 555–600.

[23] K.S. Novoselov, A.K. Geim, S.V. Morozov, D. Jiang, Y. Zhang, S.V. Dubonos, I.V. Grigorieva, and A.A. Firsov. “Electric field effect in atomically thin carbon films”. In: *Science* 306 (2004), page 666.

[24] K.V. Emtsev, A. Bostwick, K. Horn, J. Jobst, G.L. Kellogg, L. Ley, J.L. McChesney, T. Ohta, S.A. Reshanov, J. Röhrl, et al. “Towards wafer-size graphene layers by atmospheric pressure graphitization of silicon carbide”. In: *Nature Materials* 8 (2009), pages 203–207.

[25] P. Poncharal, C. Berger, Y. Yi, ZL Wang, and W.A. De Heer. “Room temperature ballistic conduction in carbon nanotubes”. In: *Journal of Physical Chemistry B* 106 (2002), pages 12104–12118.

[26] K. Järrendahl and R.F. Davis. “Materials properties and characterization of SiC”. In: *Semiconductors and Semimetals* 52 (1998), pages 1–20.

[27] T. Seyller. “Epitaxial graphene on SiC (0001)”. In: *Graphene Nanoelectronics* (2012), pages 135–159.

[28] A. Bostwick, T. Ohta, T. Seyller, K. Horn, and E. Rotenberg. “Quasiparticle dynamics in graphene”. In: *Nature Physics* 3 (2006), pages 36–40.

[29] I. Forbeaux, J.M. Themlin, and J.M. Debever. “Heteroepitaxial graphite on 6H-SiC (0001): Interface formation through conduction-band electronic structure”. In: *Physical Review B* 58 (1998), page 16396.

[30] I. Forbeaux, J.M. Themlin, A. Charrier, F. Thibaudau, and J.M. Debever. “Solid-state graphitization mechanisms of silicon carbide 6H-SiC polar faces”. In: *Applied Surface Science* 162 (2000), pages 406–412.

[31] Z.Y. Juang, C.Y. Wu, C.W. Lo, W.Y. Chen, C.F. Huang, J.C. Hwang, F.R. Chen, K.C. Leou, and C.H. Tsai. “Synthesis of graphene on silicon carbide substrates at low temperature”. In: *Carbon* 47 (2009), pages 2026–2031.

[32] S. Unarunotai, Y. Murata, C.E. Chialvo, H. Kim, S. MacLaren, N. Mason, I. Petrov, and J.A. Rogers. “Transfer of graphene layers grown on SiC wafers to other substrates and their integration into field effect transistors”. In: *Applied Physics Letters* 95 (2009), pages 202101–202101.

[33] S. Unarunotai, J.C. Koepke, C.L. Tsai, F. Du, C.E. Chialvo, Y. Murata, R. Haasch, I. Petrov, N. Mason, M. Shim, et al. “Layer-by-layer transfer of multiple, large area sheets of graphene grown in multilayer stacks on a single SiC wafer”. In: *ACS Nano* (2010).

[34] K.V. Emtsev, F. Speck, T. Seyller, L. Ley, and J.D. Riley. “Interaction, growth, and ordering of epitaxial graphene on SiC {0001} surfaces: A comparative photoelectron spectroscopy study”. In: *Physical Review B* 77 (2008), page 155303.

[35] K.V. Emtsev, T. Seyller, F. Speck, L. Ley, P. Stojanov, J.D. Riley, and R.C.G Leckey. “Initial stages of the graphite-SiC (0001) interface formation studied by photoelectron spectroscopy”. In: *Materials Science Forum*. Volume 556. Trans Tech Publ. 2007, pages 525–528.

[36] F. Varchon, R. Feng, J. Hass, X. Li, B.N. Nguyen, C. Naud, P. Mallet, J.Y. Veuillen, C. Berger, E.H Conrad, et al. “Electronic structure of epitaxial graphene layers on SiC: effect of the substrate”. In: *Physical Review Letters* 99 (2007), page 126805.

[37] L. Magaud, F. Hiebel, F. Varchon, P. Mallet, and J.Y. Veuillen. “How the SiC substrate impacts graphene’s atomic and electronic structure”. In: *Physica Status Solidi Rapid Research Letters* 3 (2009), pages 172–174.

[38] T. Ohta, A. Bostwick, T. Seyller, K. Horn, and E. Rotenberg. “Controlling the electronic structure of bilayer graphene”. In: *Science* 313 (2006), page 951.

[39] A.B. Kuzmenko, E. van Heumen, D. van der Marel, P. Lerch, P. Blake, K.S. Novoselov, and A.K. Geim. “Infrared spectroscopy of electronic bands in bilayer graphene”. In: *Physical Review B* 79 (2009), page 115441.

[40] J.B. Oostinga, H.B. Heersche, X. Liu, A.F. Morpurgo, and L.M.K. Vandersypen. “Gate-induced insulating state in bilayer graphene devices”. In: *Nature Materials* 7 (2007), pages 151–157.

[41] E.V. Castro, K.S. Novoselov, S.V. Morozov, N.M.R. Peres, J.M.B.L. Dos Santos, J. Nilsson, F. Guinea, A.K. Geim, and A.H.C. Neto. “Biased bilayer graphene: semiconductor with a gap tunable by the electric field effect”. In: *Physical Review Letters* 99 (2007), page 216802.

[42] J. Nilsson, A.H.C. Neto, F. Guinea, and N.M.R. Peres. “Transmission through a biased graphene bilayer barrier”. In: *Physical Review B* 76 (2007), page 165416.

[43] J. Kedzierski, P.L. Hsu, P. Healey, P.W. Wyatt, C.L. Keast, M. Sprinkle, C. Berger, and W.A. de Heer. “Epitaxial graphene transistors on SiC substrates”. In: *Electron Devices, IEEE Transactions on* 55 (2008), pages 2078–2085.

[44] A.Y. Tontegode. “Carbon on transition metal surfaces”. In: *Progress in Surface Science* 38 (1991), pages 201–429.

[45] C. Oshima and A. Nagashima. “Ultra-thin epitaxial films of graphite and hexagonal boron nitride on solid surfaces”. In: *Journal of Physics: Condensed Matter* 9 (1997), page 1.

[46] N.R. Gall, E.V. Rut’kov, and A.Y. Tontegode. “Two Dimensional Graphite Films on Metals and Their Intercalation”. In: *International Journal of Modern Physics B* 11 (1997), pages 1865–1912.

[47] S. Bae, H. Kim, Y. Lee, X. Xu, J.S. Park, Y. Zheng, J. Balakrishnan, T. Lei, H.R. Kim, Y.I. Song, et al. “Roll-to-roll production of 30-inch graphene films for transparent electrodes”. In: *Nature Nanotechnology* 5 (2010), pages 574–578.

[48] Y. Lee, S. Bae, H. Jang, S. Jang, S.E. Zhu, S.H. Sim, Y.I. Song, B.H. Hong, and J.H. Ahn. “Wafer-scale synthesis and transfer of graphene films”. In: *Nano Letters* 10 (2010), pages 490–493.

[49] J.C. Shelton, H.R. Patil, and J.M. Blakely. “Equilibrium segregation of carbon to a nickel (111) surface: A surface phase transition”. In: *Surface Science* 43 (1974), pages 493–520.

[50] M. Eizenberg and J.M. Blakely. “Carbon monolayer phase condensation on Ni (111)”. In: *Surface Science* 82 (1979), pages 228–236.

[51] J.C. Hamilton and J.M. Blakely. “Carbon segregation to single crystal surfaces of Pt, Pd and Co”. In: *Surface Science* 91 (1980), pages 199–217.

[52] C. Enderlein, Y.S. Kim, A. Bostwick, E. Rotenberg, and K. Horn. “The formation of an energy gap in graphene on ruthenium by controlling the interface”. In: *New Journal of Physics* 12 (2010), page 033014.

[53] Y. Dedkov, K. Horn, A. Preobrajenski, and M. Fonin. “Epitaxial Graphene on metals”. In: *Graphene Nanoelectronics* (2012), pages 189–234.

[54] E. Voloshina and Y. Dedkov. “Graphene on metallic surfaces: problems and perspectives”. In: *Physical Chemistry Chemical Physics* (2012).

[55] A.T. N'Diaye, S. Bleikamp, P.J. Feibelman, and T. Michely. "Two-dimensional Ir cluster lattice on a graphene moire on Ir (111)". In: *Physical Review Letters* 97 (2006), page 215501.

[56] A.B. Preobrajenski, M.L. Ng, A.S. Vinogradov, and N. Mårtensson. "Controlling graphene corrugation on lattice-mismatched substrates". In: *Physical Review B* 78 (2008), page 073401.

[57] A.L. Vazquez de Parga, F. Calleja, B. Borca, MCG Passeggi Jr, J.J. Hinarejos, F. Guinea, and R. Miranda. "Periodically rippled graphene: growth and spatially resolved electronic structure". In: *Physical Review Letters* 100 (2008), page 56807.

[58] D. Martoccia, P.R. Willmott, T. Brugger, M. Björck, S. Günther, C.M. Schlepütz, A. Cervellino, S.A. Pauli, B.D. Patterson, S. Marchini, et al. "Graphene on Ru (0001): a 25× 25 supercell". In: *Physical Review Letters* 101 (2008), page 126102.

[59] S. Marchini, S. Günther, and J. Wintterlin. "Scanning tunneling microscopy of graphene on Ru (0001)". In: *Physical Review B* 76 (2007), page 075429.

[60] J. Coraux, T.N. Plasa, C. Busse, T. Michely, et al. "Structure of epitaxial graphene on Ir (111)". In: *New Journal of Physics* 10 (2008), page 043033.

[61] I. Pletikosić, M. Kralj, P. Pervan, R. Brako, J. Coraux, AT N'Diaye, C. Busse, and T. Michely. "Dirac cones and minigaps for graphene on Ir (111)". In: *Physical Review Letters* 102 (2009), page 56808.

[62] E. Starodub, A. Bostwick, L. Moreschini, S. Nie, F. El Gabaly, K.F. McCarty, and E. Rotenberg. "In-plane orientation effects on the electronic structure, stability, and Raman scattering of monolayer graphene on Ir (111)". In: *Physical Review B* 83 (2011), page 125428.

[63] X. Li, W. Cai, J. An, S. Kim, J. Nah, D. Yang, R. Piner, A. Velamakanni, I. Jung, E. Tutuc, et al. "Large-area synthesis of high-quality and uniform graphene films on copper foils". In: *Science* 324 (2009), pages 1312–1314.

[64] K.S. Kim, Y. Zhao, H. Jang, S.Y. Lee, J.M. Kim, K.S. Kim, J.H. Ahn, P. Kim, J.Y. Choi, and B.H. Hong. "Large-scale pattern growth of graphene films for stretchable transparent electrodes". In: *Nature* 457 (2009), pages 706–710.

[65] P. Grünberg, R. Schreiber, Y. Pang, M. B. Brodsky, and H. Sowers. "Layered Magnetic Structures: Evidence for Antiferromagnetic Coupling of Fe Layers across Cr Interlayers". In: *Physical Review Letters* 57 (1986), pages 2442–2445.

[66] C. Chappert, A. Fert, and F.N. Van Dau. "The emergence of spin electronics in data storage". In: *Nature Materials* 6 (2007), pages 813–823.

[67] V.M. Karpan, G. Giovannetti, P.A. Khomyakov, M. Talanana, A.A. Starikov, M. Zwierzycki, J. van den Brink, G. Brocks, and P.J. Kelly. "Graphite and graphene as perfect spin filters". In: *Physical Review Letters* 99 (2007), page 176602. ISSN: 1079-7114.

[68] R.A. De Groot, F.M. Mueller, P.G. Engen, and K.H.J. Buschow. “New class of materials: Half-metallic ferromagnets”. In: *Physical Review Letters* 50 (1983), pages 2024–2027.

[69] S. Hüfner. *Photoelectron spectroscopy: principles and applications*. Springer Verlag, 2003.

[70] K. Siegbahn. “Electron spectroscopy for atoms, molecules, and condensed matter”. In: *Science* 217 (1982).

[71] J. Stöhr. *NEXAFS spectroscopy*. Springer, 2003.

[72] T.A. Carlson. “Basic assumptions and recent developments in quantitative XPS”. In: *Surface and Interface Analysis* 4.4 (1982), pages 125–134.

[73] N.V. Smith. “Inverse photoemission and related techniques”. In: *Vacuum* 33 (1983), pages 803–811.

[74] F.J. Himpsel and D. Straub. “Inverse photoemission as a probe for unoccupied electronic states”. In: *Surface Science* 168 (1986), pages 764–772.

[75] J.J. Barton. “Photoelectron holography”. In: *Physical Review Letters* 61 (1988), page 1356.

[76] K.U. Weiss, R. Dippel, K.M. Schindler, P. Gardner, V. Fritzsche, AM Bradshaw, ALD Kilcoyne, and DP Woodruff. “Chemical shift photoelectron diffraction from molecular adsorbates”. In: *Physical Review Letters* 69 (1992), page 3196.

[77] D.M. Neumark. “Time-resolved photoelectron spectroscopy of molecules and clusters”. In: *Annual Review of Physical Chemistry* 52 (2001), pages 255–277.

[78] S. Imada, S. Suga, W. Kuch, and J. Kirschner. “Magnetic microspectroscopy by a combination of XMCD and PEEM”. In: *Surface Review and Letters* 9 (2002), pages 877–882.

[79] A. Kaminski and H.M. Fretwell. “On the extraction of the self-energy from angle-resolved photoemission spectroscopy”. In: *New Journal of Physics* 7 (2005), page 98.

[80] N.D. Lang and W. Kohn. “Theory of metal surfaces: work function”. In: *Physical Review B* 3 (1971), page 1215.

[81] B.T. Thole, P. Carra, F. Sette, and G. Van der Laan. “X-ray circular dichroism as a probe of orbital magnetization”. In: *Physical Review Letters* 68 (1992), pages 1943–1946.

[82] P. Carra, B.T. Thole, M. Altarelli, and X. Wang. “X-ray circular dichroism and local magnetic fields”. In: *Physical Review Letters* 70 (1993), pages 694–697.

[83] J.M. Esteva, R.C. Karnatak, J.C. Fuggle, and G.A. Sawatzky. “Selection rules and multiplet effects in comparison of x-ray absorption and photoemission peak energies”. In: *Physical Review Letters* 50 (1983), pages 910–913.

[84] A. E. Becquerel. “Mémoire sur les effets électriques produits sous l’influence des rayons solaires”. In: *Comptes Rendus des Séances Hebdomadaires* 9 (1839), pages 561–567.

[85] P. Lenard. “Über die lichtelektrische Wirkung”. In: *Annalen der Physik* 313 (1902), pages 149–198.

[86] H.P. Bonzel and C. Kleint. “On the history of photoemission”. In: *Progress in Surface Science* 49 (1995), pages 107–153.

[87] A. Einstein. “Über einen die Erzeugung und Verwandlung des Lichtes betreffenden heuristischen Gesichtspunkt”. In: *Annalen der Physik* 322 (1905), pages 132–148.

[88] M.P. Seah. “The quantitative analysis of surfaces by XPS: a review”. In: *Surface and Interface Analysis* 2 (1980), pages 222–239.

[89] G. Ertl and J. Küppers. *Low energy electrons and surface chemistry*. VCH Verlagsgellschaft. Distribution, USA and Canada, VCH Publishers, 1985.

[90] I. Lindau and W.E. Spicer. “The probing depth in photoemission and Auger-electron spectroscopy”. In: *Journal of Electron Spectroscopy and Related Phenomena* 3 (1974), pages 409–413.

[91] H. Ibach. *Electron spectroscopy for surface analysis*. Springer-Verlag Berlin, 1977.

[92] A.C. Thompson, D. Vaughan, Center for X-ray optics, and advanced light source. *X-ray data booklet*. Lawrence Berkeley National Laboratory, University of California Berkeley, CA, 2001.

[93] A. Bansil, M. Lindroos, S. Sahrakorpi, and R.S. Markiewicz. “Influence of the third dimension of quasi-two-dimensional cuprate superconductors on angle-resolved photoemission spectra”. In: *Physical Review B* 71 (2005), page 012503.

[94] R.C.G. Leckey. “Recent developments in electron energy analysers”. In: *Journal of Electron Spectroscopy and Related Phenomena* 43 (1987), pages 183–214.

[95] B. Frietsch. “Winkelaufgelaufgelöste Photoemission an niederdimensionalen Quantentopfsystemen”. Master’s thesis. Hochschule Ravensburg-Weingarten, 2007.

[96] *Manual: Hemispherical Energy Analyzer PHOIBOS 100*. SPECS GmbH, 2008.

[97] D. Norman, J. Stöhr, R. Jaeger, PJ Durham, and J.B. Pendry. “Determination of local atomic arrangements at surfaces from near-edge X-ray-absorption fine-structure studies: O on Ni (100)”. In: *Physical Review Letters* 51 (1983), pages 2052–2055.

[98] I.H. Hertel, I.V. Hertel, and C.P. Schulz. *Atom-, Molekul-und Optische Physik*. Springer Verlag, 2008.

[99] H.A. Bethe and E.E. Salpeter. *Quantum mechanics of one-and two-electron atoms.* Plenum Publishing Corporation, 1977.

[100] K. Kummer. “Investigation of structural properties in biomolecular systems using synchrotron-based spectroscopies”. PhD thesis. 2009.

[101] G. Schütz, W. Wagner, W. Wilhelm, P. Kienle, R. Zeller, R. Frahm, and G. Materlik. “Absorption of circularly polarized x rays in iron”. In: *Physical Review Letters* 58 (1987), pages 737–740.

[102] J. Stöhr. “Exploring the microscopic origin of magnetic anisotropies with X-ray magnetic circular dichroism (XMCD) spectroscopy”. In: *Journal of Magnetism and Magnetic Materials* 200 (1999), pages 470–497.

[103] W. Kuch. “Imaging magnetic microspectroscopy”. In: *Magnetic Microscopy of Nanostructures* (2005), pages 1–28.

[104] B.J. Hales. “Magnetic circular dichroism spectroscopy.” In: *Methods in Molecular Biology* 766 (2011), page 207.

[105] J. Stöhr and H.C. Siegmann. *Magnetism: from fundamentals to nanoscale dynamics.* Springer Heidelberg, 2006.

[106] J. Stöhr. “X-ray magnetic circular dichroism spectroscopy of transition metal thin films”. In: *Journal of Electron Spectroscopy and Related Phenomena* 75 (1995), pages 253–272.

[107] *Feynman, R.P. and Leighton, R.B. and Sands, M. The Feynman Lectures on Physics, Vol. I, Part 2, Addison-Wesley, Reading, MA, 1964.*

[108] J. Stöhr and H. König. “Determination of spin-and orbital-moment anisotropies in transition metals by angle-dependent X-ray magnetic circular dichroism”. In: *Physical Review Letters* 75 (1995), pages 3748–3751.

[109] O. Eriksson, B. Johansson, R.C. Albers, A.M. Boring, and M.S.S. Brooks. “Orbital magnetism in Fe, Co, and Ni”. In: *Physical Review B* 42 (1990), page 2707.

[110] P. Söderlind, O. Eriksson, B. Johansson, RC Albers, and AM Boring. “Spin and orbital magnetism in Fe-Co and Co-Ni alloys”. In: *Physical Review B* 45 (1992), page 12911.

[111] E.C. Stoner. “Collective electron ferromagnetism. II. Energy and specific heat”. In: *Proceedings of the Royal Society of London. Series A, Mathematical and Physical Sciences* 169 (1939), pages 339–371.

[112] H. Ebert. “Magneto-optical effects in transition metal systems”. In: *Reports on Progress in Physics* 59 (1999), page 1665.

[113] H. Ebert and G. Schütz. “Spin-Orbit-Influenced Spectroscopies of Magnetic Solids”. In: *Lecture Notes in Physics, Berlin Springer Verlag.* Volume 466. 1996.

[114] U. Fano. “Spin orientation of photoelectrons ejected by circularly polarized light”. In: *Physical Review* 178 (1969), page 131.

[115] U. Fano. “Spin orientation of photoelectrons: erratum and addendum”. In: *Physical Review* 184 (1969), page 250.

[116] H. Ebert, J. Stöhr, S.S.P Parkin, M. Samant, and A. Nilsson. “L-edge x-ray absorption in fcc and bcc Cu metal: Comparison of experimental and first-principles theoretical results”. In: *Physical Review B* 53 (1996), page 16067.

[117] E.D. Crozier. “A review of the current status of XAFS spectroscopy”. In: *Nuclear Instruments and Methods in Physics Research Section B: Beam Interactions with Materials and Atoms* 133 (1997), pages 134–144.

[118] V. L. Aksenov, M. V. Koval’chuk, A. Y. Kuz’min, Y. Purans, and S. I. Tyutyunnikov. “Development of methods of EXAFS spectroscopy on synchrotron radiation beams: Review”. In: *Crystallography Reports* 51.6 (2006), pages 908–935.

[119] J. Kołaczkiewicz and E. Bauer. “The adsorption of Ni on W (110) and (211) surfaces”. In: *Surface Science* 144 (1984), pages 495–511.

[120] C. Schmidthals, D. Sander, A. Enders, and J. Kirschner. “Structure and morphology of Ni monolayers on W (110)”. In: *Surface Science* 417 (1998), pages 361–371.

[121] D. Sander, A. Enders, C. Schmidthals, D. Reuter, and J. Kirschner. “Mechanical stress and magnetism of ferromagnetic monolayers”. In: *Surface Science* 402 (1998), pages 351–355.

[122] D. Sander, A. Enders, C. Schmidthals, J. Kirschner, HL Johnston, CS Arnold, and D. Venus. “Structure and perpendicular magnetization of Fe/Ni (111) bilayers on W (110)”. In: *Journal of Applied Physics* 81 (1997), page 4702.

[123] Y.S. Dedkov, M. Fonin, U. Rüdiger, and C. Laubschat. “Graphene-protected iron layer on Ni (111)”. In: *Applied Physics Letters* 93 (2008), page 022509.

[124] Y.S. Dedkov, M. Fonin, and C. Laubschat. “A possible source of spin-polarized electrons: The inert graphene/Ni (111) system”. In: *Applied Physics Letters* 92 (2008), page 052506.

[125] T. Aizawa, R. Souda, S. Otani, Y. Ishizawa, and C. Oshima. “Anomalous bond of monolayer graphite on transition-metal carbide surfaces”. In: *Physical Review Letters* 64 (1990), pages 768–771.

[126] Y.S. Dedkov and M. Fonin. “Electronic and magnetic properties of the graphene-ferromagnet interface”. In: *New Journal of Physics* 12 (2010), page 125004.

[127] D. Usachov, O. Vilkov, A. Grüneis, D. Haberer, A. Fedorov, V. Adamchuk, A. Preobrajenski, P. Dudin, A. Barinov, M. Oehzelt, C. Laubschat, and D. Vyalikh. “Nitrogen-doped graphene: efficient growth, structure and electronic properties”. In: *Nano Letters* (2011).

[128] N.R. Gall, E.V. Rut’Kov, and A.Y. Tontegode. “Intercalation of nickel atoms under two-dimensional graphene film on (111) Ir”. In: *Carbon* 38 (2000), pages 663–667.

[129] A.M. Shikin, G.V. Prudnikova, V.K. Adamchuk, F. Moresco, and K.H. Rieder. "Surface intercalation of gold underneath a graphite monolayer on Ni (111) studied by angle-resolved photoemission and high-resolution electron-energy-loss spectroscopy". In: *Physical Review B* 62 (2000), page 13202.

[130] Y.S. Dedkov, A.M. Shikin, V.K. Adamchuk, S.L. Molodtsov, C. Laubschat, A. Bauer, and G. Kaindl. "Intercalation of copper underneath a monolayer of graphite on Ni (111)". In: *Physical Review B* 64 (2001), page 035405.

[131] A. Varykhalov, J. Sánchez-Barriga, A.M. Shikin, C. Biswas, E. Vescovo, A. Rybkin, D. Marchenko, and O. Rader. "Electronic and magnetic properties of quasifreestanding graphene on Ni". In: *Physical Review Letters* 101 (2008), page 157601.

[132] M. Sicot, P. Leicht, A. Zusan, S. Bouvron, O. Zander, M. Weser, Y.S. Dedkov, K. Horn, and M. Fonin. "Size-selected epitaxial nanoislands underneath graphene Moiré on Rh (111)". In: *ACS Nano* (2012).

[133] N.R. Gall, E.V. Rut'kov, and A.Y. Tontegode. "Efficiency of the intercalation of aluminum atoms under a monolayer and submonolayer two-dimensional graphite film on a metal". In: *Semiconductors* 36 (2002), pages 276–281.

[134] G. Bertoni, L. Calmels, A. Altibelli, and V. Serin. "First-principles calculation of the electronic structure and EELS spectra at the graphene/Ni (111) interface". In: *Physical Review B* 71 (2005), page 075402.

[135] Y.H. Wu, T. Yu, and Z.X. Shen. "Two-dimensional carbon nanostructures: fundamental properties, synthesis, characterization, and potential applications". In: *Journal of Applied Physics* 108 (2010), pages 071301–071301.

[136] E.N. Voloshina, Y.S. Dedkov, S. Torbrugge, A. Thissen, and M. Fonin. "Graphene on Rh (111): Scanning tunneling and atomic force microscopies studies". In: *Applied Physics Letters* 100 (2012), pages 241606–241606.

[137] Y. Gamo, A. Nagashima, M. Wakabayashi, M. Terai, and C. Oshima. "Atomic structure of monolayer graphite formed on Ni (111)". In: *Surface Science* 374 (1997), pages 61–64.

[138] M. Weser, Y. Rehder, K. Horn, M. Sicot, M. Fonin, A.B. Preobrajenski, E.N. Voloshina, E. Goering, and Y.S. Dedkov. "Induced magnetism of carbon atoms at the graphene/Ni (111) interface". In: *Applied Physics Letters* 96 (2010), page 012504. DOI: `http://dx.doi.org/10.1063/1.3280047`.

[139] S. Sinharoy and LL Levenson. "The formation and decomposition of nickel carbide in evaporated nickel films on graphite". In: *Thin Solid Films* 53 (1978), pages 31–36.

[140] M. Sprinkle, D. Siegel, Y. Hu, J. Hicks, A. Tejeda, A. Taleb-Ibrahimi, P. Le Fèvre, F. Bertran, S. Vizzini, H. Enriquez, et al. "First direct observation of a nearly ideal graphene band structure". In: *Physical Review Letters* 103 (2009), page 226803.

[141] E.L. Shirley, L.J. Terminello, A. Santoni, and F.J. Himpsel. “Brillouin-zone-selection effects in graphite photoelectron angular distributions”. In: *Physical Review B* 51 (1995), page 13614.

[142] M. Weser, E. N. Voloshina, K. Horn, and Yu. S. Dedkov. “Electronic structure and magnetic properties of the graphene/Fe/Ni(111) intercalation-like system”. In: *Phys. Chem. Chem. Phys.* 13 (16 2011), pages 7534–7539. DOI: `http://dx.doi.org/10.1039/C1CP00014D`.

[143] A. Grüneis, K. Kummer, and D.V. Vyalikh. “Dynamics of graphene growth on a metal surface: a time-dependent photoemission study”. In: *New Journal of Physics* 11 (2009), page 073050.

[144] E.N. Voloshina, A. Generalov, M. Weser, S. Boettcher, K. Horn, and Y.S. Dedkov. “Structural and electronic properties of the graphene/Al/Ni (111) intercalation-like system”. In: *New Journal of Physics* 13 (2011), page 113028. DOI: `http://dx.doi.org/10.1088/1367-2630/13/11/113028`.

[145] F. Liu and T.S. Seo. “A Controllable Self-Assembly Method for Large-Scale Synthesis of Graphene Sponges and Free-Standing Graphene Films”. In: *Advanced Functional Materials* 20 (2010), pages 1930–1936.

[146] A. Bostwick, T. Ohta, J.L. McChesney, K.V. Emtsev, T. Seyller, K. Horn, and E. Rotenberg. “Symmetry breaking in few layer graphene films”. In: *New Journal of Physics* 9 (2007), page 385.

[147] R.A. Rosenberg, P.J. Love, V.V. Rehn, et al. “Polarization-dependent C (K) near-edge x-ray-absorption fine structure of graphite.” In: *Physical Review. B* 33 (1986), page 4034.

[148] E.J. Mele and J.J. Ritsko. “Fermi-level lowering and the core exciton spectrum of intercalated graphite”. In: *Physical Review Letters* 43 (1979), pages 68–71.

[149] Y. Ma, P. Skytt, N. Wassdahl, P. Glans, J. Guo, and J. Nordgren. “Core excitons and vibronic coupling in diamond and graphite”. In: *Physical Review Letters* 71 (1993), pages 3725–3728.

[150] P.A. Brühwiler, A.J. Maxwell, C. Puglia, A. Nilsson, S. Andersson, and N. Mårtensson. “π^* and σ^* Excitons in C 1s Absorption of Graphite”. In: *Physical Review Letters* 74 (1995), pages 614–617.

[151] R. Ahuja, P. A. Brühwiler, J. M. Wills, B. Johansson, N. Mårtensson, and O. Eriksson. “Theoretical and experimental study of the graphite 1s x-ray absorption edges”. In: *Physical Review B* 54 (1996), page 14396.

[152] O. Wessely, M.I. Katsnelson, and O. Eriksson. “Ab initio theory of dynamical core-hole screening in graphite from x-ray absorption spectra”. In: *Physical Review Letters* 94 (2005), page 167401.

[153] P. Srivastava, F. Wilhelm, A. Ney, M. Farle, H. Wende, N. Haack, G. Ceballos, and K. Baberschke. “Magnetic moments and Curie temperatures of Ni and Co thin films and coupled trilayers”. In: *Physical Review B* 58 (1998), page 5701.

[154] K. Baberschke. “The magnetism of Nickewl monolayers”. In: *Applied Physics A: Mater. Sci. Process* 62 (1996), page 417.

[155] H.C. Mertins, S. Valencia, W. Gudat, P.M. Oppeneer, O. Zaharko, and H. Grimmer. “Direct observation of local ferromagnetism on carbon in C/Fe multilayers”. In: *Europhysics Letters* 66 (2004), page 743.

[156] O. Cespedes, M.S. Ferreira, S. Sanvito, M. Kociak, and J.M.D. Coey. “Contact induced magnetism in carbon nanotubes”. In: *Journal of Physics: Condensed Matter* 16 (2004), page L155.

[157] J.P. Perdew, K. Burke, and M. Ernzerhof. “Generalized gradient approximation made simple”. In: *Physical Review Letters* 77 (1996), pages 3865–3868.

[158] G. Kresse and J. Furthmüller. “Efficiency of ab-initio total energy calculations for metals and semiconductors using a plane-wave basis set”. In: *Computational Materials Science* 6 (1996), pages 15–50.

[159] G. Kresse and J. Furthmüller. “Efficient iterative schemes for ab initio total-energy calculations using a plane-wave basis set”. In: *Physical Review B* 54 (1996), page 11169.

[160] P.E. Blöchl. “Projector augmented-wave method”. In: *Physical Review B* 50 (1994), page 17953.

[161] S.Y. Zhou, G.H. Gweon, A.V. Fedorov, P.N. First, W.A. De Heer, D.H. Lee, F. Guinea, A.H.C. Neto, and A. Lanzara. “Substrate-induced bandgap opening in epitaxial graphene”. In: *Nature Materials* 6 (2007), pages 770–775.

[162] A. Qaiumzadeh and R. Asgari. “The effect of sublattice symmetry breaking on the electronic properties of doped graphene”. In: *New Journal of Physics* 11 (2009), page 095023.

[163] B. Dóra and K. Ziegler. “Gaps and tails in graphene and graphane”. In: *New Journal of Physics* 11 (2009), page 095006.

[164] F.J. Himpsel, J.E. Ortega, G.J. Mankey, and R.F. Willis. “Magnetic nanostructures”. In: *Advances in Physics* 47 (1998), pages 511–597.

[165] J. Thomassen, F. May, B. Feldmann, M. Wuttig, and H. Ibach. “Magnetic live surface layers in Fe/Cu (100)”. In: *Physical Review Letters* 69 (1992), pages 3831–3834.

[166] M.T. Kief and W.F. Egelhoff Jr. “Growth and structure of Fe and Co thin films on Cu (111), Cu (100), and Cu (110): A comprehensive study of metastable film growth”. In: *Physical Review B* 47 (1993), page 10785.

[167] K. Heinz, S. Müller, and P. Bayer. “Multilayer reconstruction of ultrathin epitaxial fcc Fe films”. In: *Surface Science* 337 (1995), pages 215–223.

[168] P. Bayer, S. Müller, P. Schmailzl, and K. Heinz. “Nonpseudomorphic and surface-reconstructed ultrathin epitaxial fcc Fe films on Cu (100)”. In: *Physical Review B* 48 (1993), page 17611.

[169] D. Li, M. Freitag, J. Pearson, Z.Q. Qiu, and S.D. Bader. “Magnetic and structural instabilities of ferromagnetic and antiferromagnetic Fe/Cu (100)”. In: *Journal of Applied Physics* 76 (1994), pages 6425–6427.

[170] M. Straub, R. Vollmer, and J. Kirschner. “Surface magnetism of ultrathin γ-Fe films investigated by nonlinear magneto-optical Kerr effect”. In: *Physical Review Letters* 77 (1996), pages 743–746.

[171] M. Wuttig, B. Feldmann, J. Thomassen, F. May, H. Zillgen, A. Brodde, H. Hannemann, and H. Neddermeyer. “Structural transformations of fcc iron films on Cu (100)”. In: *Surface Science* 291 (1993), pages 14–28.

[172] J. Giergiel, J. Kirschner, J. Landgraf, J. Shen, and J. Woltersdorf. “Stages of structural transformation in iron thin film growth on copper (100)”. In: *Surface Science* 310 (1994), pages 1–15.

[173] J. Giergiel, J. Shen, J. Woltersdorf, A. Kirilyuk, and J. Kirschner. “Growth and morphology of ultrathin Fe films on Cu (001)”. In: *Physical Review B* 52 (1995), page 8528.

[174] N.A. Vinogradov, A.A. Zakharov, V. Kocevski, J. Rusz, K.A. Simonov, O. Eriksson, A. Mikkelsen, E. Lundgren, A.S. Vinogradov, N. Mårtensson, et al. “Formation and Structure of Graphene Waves on Fe (110)”. In: *Physical Review Letters* 109 (2012), page 26101.

[175] S.S. Dhesi, H.A. Dürr, G. Van der Laan, E. Dudzik, and N.B. Brookes. “Electronic and magnetic structure of thin Ni films on Co/Cu (001)”. In: *Physical Review B* 60 (1999), page 12852.

[176] A.I. Nesvizhskii, A.L. Ankudinov, J.J. Rehr, and K. Baberschke. “Interpretation of x-ray magnetic circular dichroism and x-ray absorption near-edge structure in Ni”. In: *Physical Review B* 62 (2000), page 15295.

[177] V. Cros, F. Petroff, J. Vogel, A. Fontaine, JL Menéndez, A. Cebollada, W. Grange, JP Kappler, M. Finazzi, and N. Brookes. “Evidence for a high-spin Fe phase in Fe/Pd (001) multilayers”. In: *EPL (Europhysics Letters)* 49 (2000), page 807.

[178] I. Yamamoto, T. Nakagawa, Y. Takagi, and T. Yokoyama. “Spin reorientation transitions of Ni/Pd (111) films induced by Fe deposition”. In: *Physical Review B* 81 (2010), page 214442.

[179] K. Yamamoto, M. Fukushima, T. Osaka, and C. Oshima. “Charge-transfer mechanism for the (monolayer graphite)/Ni (111) system”. In: *Physical Review B* 45 (1992), page 11358.

[180] R. Wu and A.J. Freeman. “Structural and magnetic properties of Fe/Ni (111)”. In: *Physical Review B* 45 (1992), page 7205.

[181] T.C. Chiang. “Photoemission studies of quantum well states in thin films”. In: *Surface Science Reports* 39 (2000), pages 181–235.

[182] H. Zhang, Q. Fu, Y. Cui, D. Tan, and X. Bao. “Growth mechanism of graphene on Ru (0001) and O2 adsorption on the graphene/Ru (0001) surface”. In: *Journal of Physical Chemistry C* 113 (2009), pages 8296–8301.

[183] P. Sutter, J.T. Sadowski, and E.A. Sutter. “Chemistry under Cover: Tuning Metal- Graphene Interaction by Reactive Intercalation”. In: *Journal of the American Chemical Society* 132 (2010), pages 8175–8179.

[184] A.M. Shikin, D. Farias, and K.H. Rieder. “Phonon stiffening induced by copper intercalation in monolayer graphite on Ni (111)”. In: *Europhysics Letters* 44 (1998), page 44.

[185] Y.K. Chang, K.P. Lin, W.F. Pong, M.H. Tsai, H.H. Hseih, J.Y. Pieh, P.K. Tseng, J.F. Lee, and LS Hsu. “ELECTRONIC STRUCTURE AND TRANSPORT (PACS 71-73)-Charge transfer and hybridization effects in Ni3Al and Ni3Ga studies by x-ray-absorption spectroscopy and theoretical calculations”. In: *Journal of Applied Physics* 87 (2000), pages 1312–1317.

[186] N. Ohtsu, M. Oku, T. Shishido, and K. Wagatsuma. “X-ray photoelectron spectroscopic studies on phase identification and quantification of nickel aluminides”. In: *Applied Surface Science* 253 (2007), pages 8713–8717.

[187] M.G. Menezes, R.B. Capaz, and J.L.B. Faria. “Gap opening by asymmetric doping in graphene bilayers”. In: *Physical Review B* 82 (2010), page 245414. DOI: `10.1103/PhysRevB.82.245414`.

[188] S.L. Molodtsov, F. Schiller, S. Danzenbächer, M. Richter, J. Avila, C. Laubschat, and M.C. Asensio. “Folded bands in photoemission spectra of La-graphite intercalation compounds”. In: *Physical Review B* 67 (2003), page 115105. ISSN: 1550-235X.

[189] J. Rusz, AB Preobrajenski, M.L. Ng, N.A. Vinogradov, N. Mårtensson, O. Wessely, B. Sanyal, and O. Eriksson. “Dynamical effects in x-ray absorption spectra of graphene and monolayered h-BN on Ni (111)”. In: *Physical Review B* 81 (2010), page 073402.

[190] D.M. Gruen, A.R. Krauss, C.D. Zuiker, R. Csencsits, L.J. Terminello, J.A. Carlisle, I. Jimenez, D.G.J. Sutherland, D.K. Shuh, W. Tong, et al. “Characterization of nanocrystalline diamond films by core-level photoabsorption”. In: *Applied Physics Letters* 68 (1996), page 1640.

[191] F.L. Coffman, R. Cao, P.A. Pianetta, S. Kapoor, M. Kelly, and L.J. Terminello. “Near-edge x-ray absorption of carbon materials for determining bond hybridization in mixed sp2/sp3 bonded materials”. In: *Applied Physics Letters* 69 (1996), pages 568–570.

[192] YH Tang, TK Sham, YF Hu, CS Lee, and ST Lee. “Near-edge X-ray absorption fine structure study of helicity and defects in carbon nanotubes”. In: *Chemical Physics Letters* 366 (2002), pages 636–641.

[193] G. Kresse and J. Hafner. “Norm-conserving and ultrasoft pseudopotentials for first-row and transition elements”. In: *Journal of Physics: Condensed Matter* 6 (1994), page 8245.

[194] S. Grimme. “Accurate description of van der Waals complexes by density functional theory including empirical corrections”. In: *Journal of Computational Chemistry* 25.12 (2004), pages 1463–1473.

[195] S. Grimme. “Semiempirical GGA-type density functional constructed with a long-range dispersion correction”. In: *Journal of Computational Chemistry* 27 (2006), pages 1787–1799.

[196] S. Grimme, J. Antony, S. Ehrlich, and H. Krieg. “A consistent and accurate ab initio parametrization of density functional dispersion correction (DFT-D) for the 94 elements H-Pu”. In: *Journal of Chemical Physics* 132 (2010), page 154104.

[197] P.A. Khomyakov, G. Giovannetti, P.C. Rusu, G. Brocks, J. Van den Brink, and P.J. Kelly. “First-principles study of the interaction and charge transfer between graphene and metals”. In: *Physical Review B* 79 (2009), page 195425.

[198] A. Varykhalov, MR Scholz, T.K. Kim, and O. Rader. “Effect of noble-metal contacts on doping and band gap of graphene”. In: *Physical Review B* 82 (2010), page 121101.

[199] M.H. Kang, S.C. Jung, and J.W. Park. “Density functional study of the Au-intercalated graphene/Ni (111) surface”. In: *Physical Review B* 82 (2010), page 085409.

[200] R.J. Koch, M Weser, W Zhao, F Viñes, K Gotterbarm, SM Kozlov, O Höfert, M Ostler, C Papp, J Gebhardt, et al. “Growth and electronic structure of nitrogen-doped graphene on Ni (111)”. In: *Physical Review B* 86 (2012), page 075401. DOI: `http://link.aps.org/doi/10.1103/PhysRevB.86.075401`.

Parts of this thesis have been published in:

M. Weser, Y. Rehder, K. Horn, M. Sicot, M. Fonin, A.B. Preobrajenski, E.N. Voloshina, E. Goering, and Y.S. Dedkov. "Induced magnetism of carbon atoms at the graphene/Ni (111) interface". In: Applied Physics Letters 96 (2010), page 012504. doi: http://dx.doi.org/10.1063/1.3280047.

M. Weser, E. N. Voloshina, K. Horn, and Yu. S. Dedkov. "Electronic structure and magnetic properties of the graphene/Fe/Ni(111) intercalation-like system". In: Phys. Chem. Chem. Phys. 13 (16 2011), pages 7534-7539. doi: http://dx.doi.org/10.1039/C1CP00014D.

E.N. Voloshina, A. Generalov, M. Weser, S. Boettcher, K. Horn, and Y.S. Dedkov. "Structural and electronic properties of the graphene/Al/Ni (111) intercalation-like system". In: New Journal of Physics 13 (2011), page 113028. doi: http://dx.doi.org/10.1088/1367-2630/13/11/113028.

R.J. Koch, M. Weser, W. Zhao, F. Viñes, K. Gotterbarm, S. M. Kozlov, O. Höfert, M. Ostler, C. Papp, J. Gebhardt, et al. "Growth and electronic structure of nitrogen-doped graphene on Ni (111)". In: Physical Review B 86 (2012), page 075401. doi: http://link.aps.org/doi/10.1103/PhysRevB.86. 075401.

Acknowledgment

I would like to thank Prof. Gerad Meijer for the possibility work such familiar and well organized environments such as MP department of the Fritz-Haber Institut.

I want to thank Prof. Karsten Horn, for the possibility to work in his group and for interesting discussions over physics and many other things. He supports me during whole time and a specially at the end when the last meters becomes harder. His support reaches out the tasks of professors.

I want thank specially my supervisor Dr. Yuriy S. Dedkov for many things. Firstly that he shift my intension to this very exiting topic of graphene spintronics. Further that he show me what means "Cutting the edge.". The way how he pushed me to the limit. The huge knowledge on sample preparation, working on difficult experimental setups which he shift to me in so a short time. And that we always find back to a friendly team work after strong discussions.

Dr. Elena Voloshina aseptically for the theoretical support and the fruitful discussion which arose from that.

I want to thank my measuring colleges Stefan Böttcher, Alex Generalov, Hendrik Vita, Dr. Jes̀us Martines-Blanko, Philip Leicht, Dr. Muriel Sicoute, Alexander Leptev, Samuel Bovin, Dr. Mikail Fonin, Roland Koch and Karsten Enderlein. Together we had a very exciting time at several synchrotrons all over the world. The spectrum of emotions, which we experienced, covered the ranges from highly euphoric to total frustration like in the moments when we managed to grow multilayer graphene in contrast when we recognized that we can do it only ones. Also when Philip and I performed at 3 o'clock in the morning the maybe most craziest sample transfer that the world has ever seen. Furthermore I want to give special thanks to Roland, together we found not every failed preparation is generally bad, some of them can create chapters.

I want thank to my family. They trust in my when a I approach them with the idea to change my study to physics also when this time was not free from complications they never give up the hope and when I am sure only for 5 s. And finial support of

course.

I want to thank a few people for support in english questions they Olivia Dzwonkovski, Kurt Kummer, Daniel Engelhart, Thomas Surowiec, Thomas Weser and Solvig Schmeck. A specially Olivia, she forced me in a painful process to start to think about english grammar which was at that time a really new field for me.

My friends Sebstian Bensch, Ita Brunke, Ole Zander, Rico Liebe and Christiane Häntsch which motivates my in hart moments here in Berlin.

I want to thank unbelievable many friends which helps me to realize my private life project. We see us end of April. Same procedure as every year.

Abstract

The rising demand for every greater computing power and the continuous miniaturization of electronic devices require a detailed knowledge of the physical interactions down to the atomic scale. Graphene is a promising candidate for future applications because of its unique properties such as optical transparency which can be used touch screens, the “mass-less” electron behavior leading to high carrier mobility which is suited in electronic devices, and the mechanical robustness which is desired in many applications.

In the present work the electronic and magnetic properties of graphene on varied substrate are investigated by spectrometric methods. The results of these experiments were supported by DFT calculations. Concerning the DFT results it was possible to explain the magnetic moment induced into graphene by the formation of several new interface states. These interface states are energetically split, leading to different occupations for spin-up and spin-down states, generating the magnetic moment of the graphene layer observed in XCMD experiments. This work is focused on the study of the fundamental coupling mechanism and the possibility to influence them.

Via intercalation of Fe or Al, it was possible to increase or suppress magnetic interaction. This is a highly interesting observation because it may open the door to a continuous tuning of the induced magnetic moment into the graphene.

A promising aspect of the thesis is the investigation of epitaxially grown ordered multilayer graphene of Ni(111). Subsequently experiments showed that it is possible to tune the electronic properties of the graphene stack into the valence band configuration which are required [12, 67] to act as a spin filter device.

Abstrakt

Die zunehmende Nachfrage nach Rechnerleistung und die fortschreitende Miniaturisierung der Struktur in elektronischen Schaltkreisen erfordert ein detailliertes Wissen der Prozesse und Wechselwirkungen auf atomarer Ebene. Ein Hauptaugenmerk liegt dabei auf selbstordnenden Systemen mit deren Hilfe es möglich ist Strukturen effektiv und kontrolliert für zukünftigen Compterbauelemente zu präparieren. Graphene auf Ni(111) ist eines dieser Systeme, so lassen sich mühelos große Flächen von Graphen hoher Qualität und Ordnung wachsen. Des Weiteren hebt sich Graphen mit seinen herausragenden elektronischen, optischen und mechanischen Eigenschaften wie zum Beispiel das Auftreten von "masselossen" Ladungsträgern weit von anderen Materialien ab. Die Wahl des Ni(111) Substrates bietet die Möglichkeit Wechselwirkungen zwischen ferromagnetischen und nicht ferromagnetischen Festkörpern in einer kommensuraten Struktur zu untersuchen.

In dieser Doktorarbeit wurden die elektronischen und magnetischen Eigenschaften von Graphen auf verschiedenen Substraten mittels spektrometrischen Methoden untersucht. Die Ergebnisse wurden mit DFT-Berechnungen verglichen. Dabei konnte ein in das Graphen induziertes magnetisches Moment durch Auswertung von DFT Berechnungen der Ausbildung von mehreren Interface-Zuständen zugeordnet werden. Diese Arbeit beschäftigt sich im besonderem Maße mit den grundlegenden Kopplungsmechanismen der elektronischen Systeme des Graphen und des Ni so wie der Möglichkeit diese zu beeinflussen.

Durch Intercalation von Fe oder Al konnte die magnetischem Wechselwirkung gestärkt bzw. nahe zu ausgeschaltet werden. Dies ist eine sehr interessante Beobachtung mit Hinblick auf die Möglichkeit, die physikalischen Eigenschaften von Graphen gezielt zu verändern.

Eine viel versprechende Entdeckung ist die Entdeckung einer Methode zur Präparation von mehrlagigem Graphen. In den anschließenden spektrometrischen Untersuchungen konnte die elektronische Valenzbandstruktur so beeinflußt werden, dass sie alle Charakteristika des von Karpan vorgeschlagenen Spinfilters aufweisen [12, 67].

Eigenständigkeitserklärung

Hiermit versichere ich, dass ich die vorliegende Arbeit mit dem Titel "Electronic and Magnetic Properties of Graphene-Based Systems" ohne unzulässige Hilfe Dritter und ohne Benutzung anderer als der angegebenen Hilfsmittel angefertigt habe; die aus fremden Quellen direkt oder indirekt übernommenen Gedanken sind als solche kenntlich gemacht. Die Arbeit wurde bisher weder im Inland noch im Ausland in gleicher oder ähnlicher Form einer anderen Prüfungsbehörde vorgelegt. Die Dissertation wurde unter der wissenschaftlichen Betreuung von Prof. Dr. K. Horn angefertigt. Die Promotionsordnung des Fachbereichs Physik der Freien Universität Berlin erkenne ich hiermit an.

Berlin den 21.02.2013